The Dissertation Committee for Jacob Lyle Bean
certifies that this is the approved version of the following dissertation:

M Dwarf Metallicities and Exoplanets

Committee:

G. Fritz Benedict, Supervisor

Christopher Sneden, Supervisor

David Lambert

John Scalo

Christopher M. Johns-Krull

M Dwarf Metallicities and Exoplanets

by

Jacob Lyle Bean, B.S.

DISSERTATION

Presented to the Faculty of the Graduate School of

The University of Texas at Austin

in Partial Fulfillment

of the Requirements

for the Degree of

DOCTOR OF PHILOSOPHY

THE UNIVERSITY OF TEXAS AT AUSTIN

August 2007

Acknowledgments

I would like to thank my advisors Fritz Benedict and Chris Sneden for their crucial support. Fritz provided the original inspiration for the projects in this dissertation and his guidance kept me on track when complications and distractions threatened my progress. His mentoring went beyond my research and he always had the right advice for whatever issue I faced. Chris's enthusiasm to tackle the hard problem that I brought to him out of the blue one day was more than my own at times. I benefited greatly from his calm and patience in addition to his expertise as we worked together on MOOG.

I am also grateful to Peter Hauschildt, Barbara McArthur, Chris Johns-Krull, Todd Henry, Mike Endl, Tom Harrison, Dmitry Bizyaev, Ed Nelan, and Verne Smith for their collaboration. I thank David Lambert for asking tough questions and for his support at a critical moment. I also found the perspective on my work offered by John Scalo to be very helpful.

M Dwarf Metallicities and Exoplanets

Publication No. _____

Jacob Lyle Bean, Ph.D.
The University of Texas at Austin, 2007

Supervisors: G. Fritz Benedict
Christopher Sneden

This dissertation is primarily focused on the topic of M dwarf metallicities and their relevance to the study of extrasolar planets. I begin by describing a method for accurately determining M dwarf metallicities with spectral synthesis based on abundance analyses of visual binary stars. I then apply this technique and present the first spectroscopic metallicities of three M dwarfs with planetary mass companions. The three M dwarf planet hosts have sub-solar metallicities, a surprising departure from the trend observed in FGK-type planet hosting stars. I discuss the implications of this result for extrasolar planet searches around the most numerous stars in the galaxy. I also present measured metallicities for a select group of M dwarfs with precisely determined masses and luminosities. Comparison of these stars' V band magnitudes with the predictions of the current state-of-the-art theoretical models for low-mass stars indicate that the models are deficient, as previously thought. I discuss how the cool star model atmospheres that were developed for the metallicity

analysis technique might be used to improve M dwarf structure and evolution models.

In addition to M dwarf metallicities, I describe some complementary work to determine the true mass of an extrasolar planet candidate using a combined analysis of high-precision astrometry and radial velocities. I present a dynamical mass for the companion to HD 33636 that indicates it is a low-mass star instead of an exoplanet. This result demonstrates the value of follow-up astrometric observations to determine the true masses of exoplanet candidates detected with the radial velocity method. Finally, I discuss the broader implications of the results presented in this dissertation and the prospect for similar work in the future.

Table of Contents

List of Tables

List of Figures

Chapter 1

Introduction

The first unambiguous detection of a candidate planetary mass companion orbiting a solar-type star by Mayor & Queloz (1995) ushered in the era of extrasolar planet research in astronomy. Tremendous progress in this area has been made since then and more than 200 candidate planets have been announced[1]. However, the attention that the discovery and characterization of extrasolar planets receives is largely blind to an important aspect of this work: the study of extrasolar planets to aid our understanding of planet formation and evolution is strongly dependent on a supporting foundation of stellar astrophysics knowledge. The reason for this is that we cannot yet directly image extrasolar planets. Thus, almost all comparative exoplanetology that has been done to this point has been based on observations of the putative planets' host stars and inference about their characteristics. For example, the minimum masses of planets detected with the radial velocity method, the true masses of planets detected astrometrically or that transit their host stars, and the radii of transiting planets depend on assumptions of the host stars' masses and radii from stellar evolution models. Additionally, the chemical composi-

[1] A regularly updated list of reported exoplanets can be found at `http://exoplanet.eu/`.

tions of planet host stars, which are used to probe the conditions of the disks that the planets formed from, rely on stellar model atmospheres. Therefore, the accuracy of stellar theory is critical to the study of extrasolar planets. The goal of the research contained in this dissertation was to improve our understanding of planet formation and evolution through testing, improving, and applying the theoretical models that describe the lowest-mass stars, the M dwarfs.

While the distinction between the K7 and M0 spectral types in terms of physical parameters is slightly ambiguous and the hydrogen-burning minimum mass is somewhat uncertain, the M spectral class dwarfs generally have masses $0.07 \leq M \leq 0.6\ M_{\odot}$, absolute V magnitudes $20 \leq \mathrm{M}_V \leq 8.0$, and effective temperatures $2500 \leq T_{eff} \leq 4000$ K. Their notable spectral signature is strong molecular band absorption at almost all wavelengths due to the low temperatures in their photospheres. The prominent species are metal oxides (most of all TiO, but also VO) and hydrides (MgH, FeH, and CaH) in the visible, and CO and H_2O in the infrared.

M dwarfs are the most abundant stellar objects in our galaxy, making up over 70% of stars (Henry 1998). Because of this, a complete model of planet formation and evolution must necessarily account for the frequency and properties of planets around these stars. Therefore, planets discovered orbiting M dwarfs must be characterized so that they can be used to constrain theory. Accurate characterization of these planets depends on reliable M dwarf models.

Despite their numbers, M dwarfs remain one of the least understood stellar types. This is due in part to a lack of the empirical data needed to test the predictions of theoretical models. Photospheric metal abundance, metallicity, is one such parameter for which reliable data did not yet exist. This was my primary focus.

The historic deficiency of data for M dwarfs was due primarily to their intrinsic faintness, a consequence of their low mass. The proliferation of large aperture telescopes and increasingly sensitive instrumentation in recent years have now all but eliminated the observational limits on the study of M dwarfs. As a consequence of these technology developments, the determination of some physical parameters, like mass and radius, for M dwarfs has become common. However, the measurement of chemical compositions of M dwarfs is still limited, despite the ease of obtaining very high quality spectra of them. Today, the factor limiting the determination of accurate chemical compositions for M dwarfs is the lack of a technique reliable enough to interpret the complex spectra of these stars. Modern analysis techniques applied to high resolution and high signal-to-noise ratio spectra of solar-type stars consistently yield chemical abundances with internal precisions of 10% (e.g. Allende Prieto et al. 2004; Valenti & Fischer 2005). The application of these methods to M dwarfs is complicated by the effects of significant molecule formation and the resulting opacity in the photospheres of these stars.

The problem caused by molecular opacity is illustrated by Figures 1.1 and 1.2. Figure 1.1 shows a comparison of low resolution spectra, taken from

Pickles (1998), for spectral types over the range F8 – M6. Molecular band spectra are much more complex than atomic spectra and dominate the spectral regions in which they are located. TiO has an especially distributed and complex spectrum and it dominates M dwarf spectra in the regions traditionally utilized to determine the chemical compositions of solar-type stars. This can be seen in Figure 1.1, where the M dwarf spectra show a significant deviation, primarily owing to TiO absorption, from the predominantly smooth continuum spectra of earlier type stars.

Figure 1.2 compares a segment of high resolution spectra for the Sun and a M4 dwarf that corresponds to one tick mark length in Figure 1.1. Even at high-dispersion, the TiO lines blend with all other lines and create a "pseudo continuum." This makes equivalent width measurements of atomic lines in the visible and red spectral regions unreliable for all but the earliest M dwarfs (Woolf & Wallerstein 2006). Therefore, unique synthetic spectrum techniques must be employed to determine the chemical compositions of these stars.

Chapter 2 contains a description, adapted from Bean et al. (2006a), of our successful effort to develop a technique for determining accurate metallicities for M dwarfs. This success represents the next step in the ongoing evolution of M dwarf spectral analyses. Our work was based on analyses of both components of visual binary pairs that are made up of a solar-similar primary and an M dwarf secondary. I use the term "solar-similar" throughout to refer to stars for which abundances can be derived spectroscopically in an identical manner as for the Sun, roughly main sequence mid-F to mid-K

spectral class stars. The utility of the visual binary star sample was based on the reasonable assumption that stars in a bound system have the same photospheric abundances due to their having formed in a common, uniform environment. Thus, the results of our abundance analysis of the M dwarfs could be compared to the results of our abundance analysis of the corresponding primaries, which are ultimately benchmarked to the Sun. The assumption of co-evolution and this comparison yielded a critical verification of our M dwarf metallicity technique.

After developing a technique to determine M dwarf metallicities, we applied it to two samples of M dwarfs that could be used to test theoretical models. The analyses and results are presented in Chapters 3 and 4. In Chapter 3, which is adapted from Bean et al. (2006b), I discuss M dwarfs with detected planets. Gonzalez (1997) first noted the high metallicities of the first four stars which were found to exhibit radial velocity variations attributable to a planetary mass companion. This trend was found to continue as more stars were identified as potential extrasolar planet hosts with the radial velocity method, and followed up with high precision abundance analyses (see Chapter 3 for a complete list of references). We extended the previous host star metallicity studies by analyzing M dwarf planet hosts to see if the metallicity trend continued for M dwarfs.

In Chapter 4 I discuss our work on the the second sample of M dwarfs that we applied the new metallicity technique to; M dwarfs with measured dynamical masses and absolute magnitudes. These stars are the most important

calibrators of low-mass stellar structure and evolution models because the most fundamental prediction of stellar models is the luminosity of a star for a given mass. In addition to mass, metallicity is predicted to play an important role in governing early evolution and main sequence properties of low-mass stars (Kroupa & Tout 1997; Baraffe et al. 1998; Siess et al. 2000). However, most of the M dwarfs with measured masses are field stars and no measurement of their metallicities has been made to test these predictions. We measured the metallicities for a selection of low-mass stars with known masses. This resulted in the first direct quantification of the effect of this parameter on the luminosity of low-mass stars.

In addition to work on M dwarf metallicities, this dissertation includes results from complementary work on measuring the mass of an exoplanet candidate by combining high-precision radial velocity and astrometry data. This work is important because the method used to find the vast majority of exoplanets, the radial velocity method, only yields the minimum mass of the detected companion due to the inclination angle ambiguity. Chapter 5 includes a presentation, adapted from Bean et al. (2007), of our analysis method and result for the mass of the candidate planetary companion to HD 33636.

I conclude with a summary and a discussion in Chapter 6. I discuss the broader implications of our results not already mentioned in their corresponding Chapters. I also discuss the future prospects for research in the areas covered by this dissertation.

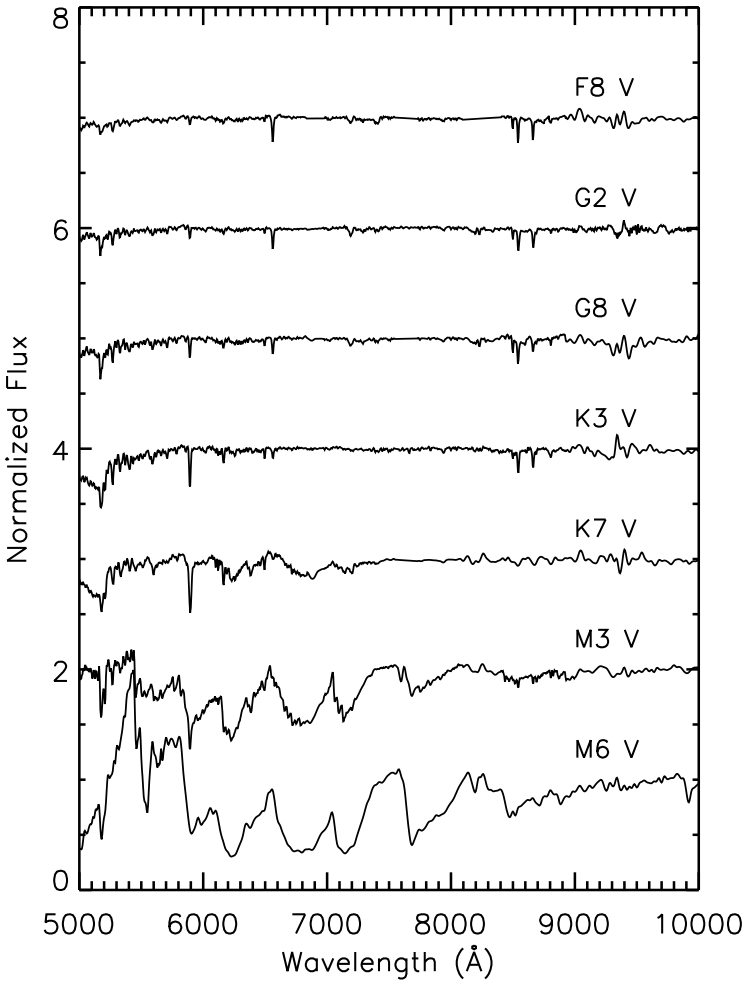

Figure 1.1 Continuum normalized spectra with arbitrary offsets for a sequence of dwarf spectral types over the range F8 – M6. The data are taken from Pickles (1998). The deviation seen in the M dwarf spectra from the mostly smooth continuum morphology of the warmer stars is due to molecular absorption (primarily TiO). This makes it impossible to apply the same techniques for chemical composition analyses to M dwarfs that are used for earlier type stars.

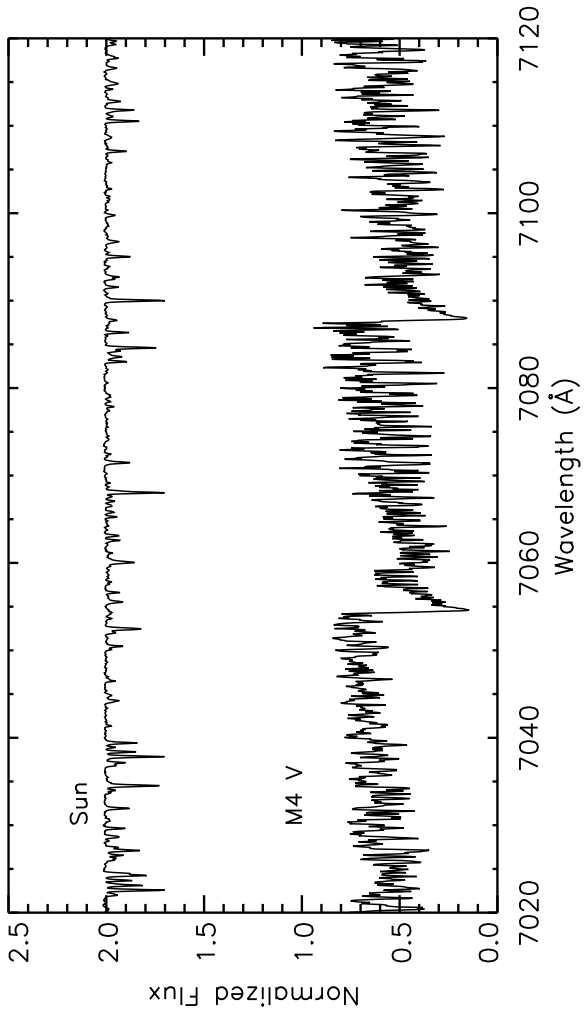

Figure 1.2 A segment of normalized high resolution (R = 60,000) and high signal-to-noise ratio (S/N > 200) spectra of the Sun (with an offset) and a M4 dwarf. The spectral region plotted corresponds to one tick mark length in Figure 1.1. Many individual atomic lines in this region of the solar spectrum could easily be used for a chemical abundance determination. The M dwarf spectrum is made up of thousands of molecular (TiO) lines blended together even at high dispersion. This makes placement of the continuum and individual line analysis impossible.

Chapter 2

Accurate M Dwarf Metallicities from Spectral Synthesis

Valenti, Piskunov, & Johns-Krull (1998, hereafter V98) pioneered the use of spectral synthesis to determine M dwarf parameters to high precision. They fit synthetic spectra of TiO and atomic lines based on the NextGen version of the PHOENIX model atmospheres (Hauschildt et al. 1999) to a high quality observed spectrum of the M3.5 V star Gl 725B to determine its parameters. Their precisions for the parameters effective temperatures, T_{eff}, surface gravity, $\log g$, metallicity, [M/H][1], and macroturbulent velocity, η, were 71 K, 0.14 dex, 0.07 dex, and 0.7 km s^{-1} respectively.

In this Chapter I present the results of a test of the V98 technique and PHOENIX cool-star model atmospheres, and our work to improve both based on the abundance analyses of visual binary stars. In §2.1 I describe our spectroscopic observations of five visual binary pairs containing primaries ranging from spectral type F7 V - K3 V and secondaries M0.5 V - M3.5 V. In §2.2 I discuss our differential abundance analysis of the primaries with respect

[1]We adopt the standard spectroscopic notation: for elements X and Y, $\log \epsilon(\mathrm{X}) \equiv \log (N(\mathrm{X})/N(\mathrm{H})) + 12.0$, $[\mathrm{X/Y}] \equiv \log (N(\mathrm{X})/N(\mathrm{Y}))_\star - \log (N(\mathrm{X})/N(\mathrm{Y}))_\odot$, and $N(\mathrm{X})$ is the number density of element X. We assume [M/H] = [Fe/H] throughout this dissertation.

to the Sun. In §2.3 I describe our application of the V98 technique to derive the metallicities of the M dwarf secondaries. Based on the assumption that stars in a bound system have the same metallicities, we showed that the original V98 technique yields metallicities for M dwarfs that are systematically 0.5 dex too low. I then outline our updates and modifications to this technique in §2.4. We showed that a re-analysis of the M dwarfs in our binary sample, using our revised method and new model atmospheres, gives a RMS deviation of 0.11 dex from the primaries' metallicities. In §2.5 I present an error analysis of the new technique, which yields uncertainties of 48 K for T_{eff}, 0.10 dex for log g, 0.12 dex for [M/H], 0.15 km s^{-1} for the microturbulent velocity, ξ, and 0.20 km s^{-1} for η. Finally, in §2.6, I summarize our results and discuss the potential ramifications of our validation of the PHOENIX cool-star model atmospheres.

2.1 Observations and Data Reduction

We selected five nearby, common proper motion, visual binary pairs containing a solar-similar primary and a M dwarf secondary from the Poveda et al. (1994), Allen et al. (2000), and *Hipparcos* (Perryman et al. 1997) catalogs. Basic data for the selected pairs are listed in Table 2.1. Spectral types of the primaries span the range from F7 V – K3 V. The M dwarf secondaries range from spectral type M0.5 V – M3.5 V, with one object not having a published spectral type but assumed to be an M dwarf based on its placement in an HR diagram. The minimum component separation on the sky, ρ, for the five pairs is 31″. Therefore, each component was easily isolated and there was no light

contamination from its companion.

We observed each component of the five visual binary pairs using the 2.7m Harlan J. Smith telescope at McDonald Observatory on November 20 and 21, 2003. Data were obtained with the 2dcoudé spectrograph (Tull et al. 1995) equipped with a 79 gr mm^{-1} echelle grating and $8\farcs2$ x $1\farcs2$ slit. Exposure times varied from 5 to 30 minutes. Multiple 30 minute exposures were taken for the M dwarfs and co-added to facilitate cosmic ray subtraction. The maximum total exposure time for a single object was 180 minutes. Additionally, we recorded a spectrum of the day sky via a port that directs outside light on to the slit entrance of the instrument.

CCD reduction and optimal order extraction were carried out using the standard IRAF[2] routines in the *imred*, *ccdred*, and *echelle* packages. After extraction, the spectra in each order were flattened using the IRAF task *continuum*. The wavelength calibrations for each night were calculated based on the identification of roughly 1000 lines in thorium-argon emission spectra taken at the beginning of the night and have RMS precisions of 0.002 Å. Each exposure contains 37 echelle orders with incomplete coverage spanning the range 3800 – 9900 Å. The average order width is 110 Å. Gaps between the orders begin at 4000 Å and increase in size with wavelength.

The final one-dimensional spectra have measured continuum signal-to-

[2]IRAF is distributed by the National Optical Astronomy Observatories, which are operated by the Association of Universities for Research in Astronomy, Inc., under cooperative agreement with the National Science Foundation.

noise, assuming Poisson statistics, of $245 \leq \mathrm{S/N} \leq 592$ pixel^{-1} for the primaries and $145 \leq \mathrm{S/N} \leq 300$ pixel^{-1} for the secondaries in the spectral regions used for analysis. The measured resolving power, $\mathrm{R} \equiv \lambda/\delta\lambda \approx 50,000$.

2.2 Analysis of the Primaries

We determined the metallicities of the primaries in our sample by using a technique that is a variation of the traditional approach for solar-similar stars. We constrain the stellar effective temperatures and surface gravities by using a photometric color relationship and evolutionary models respectively. We derive an iron abundance relative to the solar value by fitting synthetic spectra to the observed line profiles of Fe I lines and equate this parameter to metallicity. The details of our approach are discussed in the following subsections.

2.2.1 Line Data

We began by identifying Fe I lines that are unblended with neighboring lines in our observed day-sky spectrum, which we considered a proxy for the solar spectrum. We limited our search to lines for which accurate laboratory data was available in the compilation of Ramirez et al. (2007) and van der Waals damping data had been calculated by Barklem et al. (2000). For the purpose of continuum normalization, we required that each line have a region that was apparently free of contaminating lines within 3 Å of the line center. We then examined the selected lines in the spectra of the primaries for blends

and continuum windows to ensure their utility for these stars. In order to retain a reasonable sample of lines, we had to relax the unblended constraint. We identified portions of each line that did remain relatively free of contamination and used this information to construct a mask of spectral regions to be used in our analysis. Thirty Fe I lines were selected and their profiles in the observed spectrum of one of the primaries, HIP 102040A, are shown in Figure 2.1. Also shown is the fit, found with the procedure described below, used to determine the stellar parameters. Figure 2.1 illustrates the relatively clean nature of the lines selected and the specific regions that we used in our analysis.

We then determined astrophysical log gfs for the selected lines. Our procedure was the inverse of the procedure we used to determine the iron abundances of the primaries and was a two step process. We adopted a model atmosphere with the standard solar parameters, $T_{eff} = 5777$ K, $\log g = 4.44$, and [M/H] = 0.0 (by definition) that was interpolated from the grid described in the following subsection. We assumed the solar abundances of Asplund et al. (2005), namely $\log \epsilon(\mathrm{Fe})_{\odot} = 7.45$. Microturbulence and macroturbulence are not purely physical parameters and their adopted solar values vary greatly in the literature. Therefore, our first step in the process of determining astrophysical log gfs was to determine the solar microturbulence and macroturbulence values to be used. To do this we fit synthetic spectra to the high quality solar spectrum of Kurucz et al. (1984). We determined the microturbulence, ξ, and Gaussian macroturbulence, η, values that yielded synthetic spectra that best reproduced the selected line profiles as a group using an

adaptation of the χ^2 minimization algorithm of Marquardt (Marquardt 1963; Press et al. 1986). We assumed the Ramirez et al. (2007) lab log gf values for this step and found the solar ξ to be 1.24 km s^{-1} and η to be 1.90 km s^{-1}.

With these determined line broadening parameters and our adopted solar model atmosphere and abundances, we then determined log gfs values that best reproduced the solar line profiles. We again used the χ^2 minimization algorithm to find which values gave synthetic spectra that best fit the Kurucz solar spectrum. The final line data, including the lab log gfs for comparison, are listed in Table 2.2. The astrophysical log gf values average 0.08 dex lower than the lab values. As shown in §3.4, our systematic adjustment of the line data is ultimately inconsequential because our analysis of the primaries was purely differential to the Sun.

2.2.2 Model Atmospheres

We chose to use model atmospheres computed with PHOENIX for our analysis of the primaries in order to maintain consistency with our analysis of the M dwarf secondaries. The models are the latest version of the NextGen version models presented by Hauschildt et al. (1999) and are discussed further in §2.4.2. We generated a grid of models with version 13 of PHOENIX for the analysis of the primaries spanning the ranges $4000 \leq T_{eff} \leq 7000$ K, $3.5 \leq \log g \leq 5.5$, and -1.0 $\leq$ [M/H] $\leq$ +0.5 in steps of 100 K, 0.5 dex, and 0.5 dex respectively.

We interpolated in this grid to obtain model atmospheres with arbitrary

parameters for the analyses of the primaries. All the models were calculated on the same optical depth scale at 12000 Å. This feature, and the fineness of the grid in the effective temperature domain, allowed us to use a three dimensional polynomial interpolation over the logarithm of the atmospheric parameters for each depth.

2.2.3 Procedure

We determined the parameters iron abundance, [Fe/H], microturbulence, ξ, and macroturbulence, η, directly for the primaries by fitting synthetic spectra to profiles of the 30 selected Fe I lines in the observed spectra. Our procedure was similar to that used by Allende Prieto et al. (2004) and was a two step process.

In the first step, we used all the line profiles as a constraint to determine the global [Fe/H], ξ, and η. As for the determination of the astrophysical line data, we used an adaptation of the χ^2 minimization algorithm of Marquardt (Marquardt 1963; Press et al. 1986) to find which parameters yielded synthetic spectra that best fit the observed spectra. For each iteration by the algorithm in [Fe/H], a model atmosphere with the appropriate parameters was interpolated from the grid described in the previous subsection. The model T_{eff} was determined from the $(B-V)$ – T_{eff} relationship of Ramirez & Meléndez (2005). We chose $(B - V)$, as opposed to $(V - K)$ for example, because of the availability of a homogeneous set of precise photometry in these bands for our target stars. The uncertainty in our adopted T_{eff} values was estimated by

propagating the errors in the photometry through the Ramirez & Meléndez (2005) formula and adding this in quadrature with the uncertainty in the formula itself. The model log g value and uncertainty was determined by using Bertelli et al. (1994) isochrones as described in Allende Prieto et al. (2004). The model atmosphere [M/H] was set equal to [Fe/H]. The V magnitudes, (B – V) colors, and parallaxes needed to determine these parameters were taken from the *Hipparcos* catalog (Perryman et al. 1997). The color relationship and isochrones depend weakly on metallicity, so the T_{eff} and log g were determined for each iteration in [Fe/H].

We generated synthetic spectra for each line profile region with an updated version (described in detail in §2.4.1) of the plane-parallel, LTE, stellar analysis computer code MOOG (Sneden 1973) and the given model atmosphere. We use the macroturbulence parameter to account for large-scale turbulent and rotational broadening. The synthetic spectra are convolved with an isotropic Gaussian profile with a full-width half-max, FHWM, equal to the combination of the macroturbulence parameter value and the measured instrument resolution (2.55 km s^{-1}). The synthetic spectra were then resampled to the pixel scale of the observed spectrum and compared to it. The spectral regions used in evaluating the fit were determined by the mask described above. Additionally, we attempted to minimize errors introduced by departures from local thermodynamic equilibrium (LTE) by ignoring points in the line cores that are more than 0.5 residual intensity units below the continuum (Allende Prieto et al. 2004). Therefore, the exact regions that were fit vary slightly

among the objects. The match between the synthetic spectra and observed spectra was evaluated by the fitting algorithm, new parameters selected if necessary, and the algorithm continued to iterate. This process continued until the parameters which minimized χ^2 were found.

Once the best fit to all the line profiles together was found, the model atmosphere parameters, ξ, and η were fixed to their final values and the process was repeated to determine log ϵ(Fe) for each line. The abundance found for each line was compared with the solar iron abundance (7.45) so that each line gave a differential abundance, [Fe/H]. The final [Fe/H] value is the mean of the distribution of the line abundances.

Our calculated uncertainties for the derived [Fe/H] values consist of three components. The first component (σ_l) is the uncertainty in the mean of the line abundance distribution, the standard deviation divided by the square root of the number of lines used minus one. The second, σ_t, and third, σ_g, components were derived from the uncertainties in the stellar T_{eff} and log g values respectively. We re-ran the analysis for each star with the T_{eff} and log g parameters set to one sigma above and below the adopted values. This yielded a pair of derived [Fe/H] values for each parameter. The RMS deviation from the adopted [Fe/H] value for the two pairs were the second and third components. The three components were added in quadrature to yield the final uncertainty in our derived [Fe/H] values.

Our derived parameters for the solar-similar primaries are give in Table 2.3. The internal uncertainties in the derived T_{eff}, log g, and [Fe/H],

including the [Fe/H] error components, for each star are also given. The median uncertainty in [Fe/H] for the solar-similar primaries is 0.06 dex. The uncertainties in the microturbulence and macroturbulence were assumed to be 0.15 and 0.20 km s^{-1} respectively for all the objects.

2.2.4 Comparison of Results

The most common abundance analysis techniques can typically approach internal precisions of 10% for the abundances of elements with easily observed spectral lines. However, independent analyses of the same star can give abundances that differ by amounts many times quoted uncertainties (Cayrel de Strobel et al. 2001). This is of particular concern for our investigation because we are interested in determining not only the internal consistency of our abundance analyses of two very different samples of stars, solar-similar stars and M dwarfs, but also our external consistency with the results of other groups. To accomplish this, we determined iron abundances for 30 stars (referred to hereafter as the "test sample") that were analyzed by Allende Prieto et al. (2004) and Valenti & Fischer (2005). We selected objects in common with both of these studies and that had a range of stellar parameters bracketing those of our sample. We made use of the spectra, which are of similar resolution and S/N as our spectra, available via the Spectroscopic Survey of Stars in the Solar Neighborhood (S^4N) website[3] and analyzed them in an identical manner as our sample. Our derived [Fe/H] values for this test sample

[3] `http://hebe.as.utexas.edu/s4n/index.html`

have a median internal uncertainty of 0.07 dex.

The derived T_{eff}, log g, and [Fe/H] values for the test sample from Allende Prieto et al. (2004), Valenti & Fischer (2005), and this study are collected in Table 2.4. Figures 2.2, 2.3, & 2.4 compare our derived T_{eff}, log g, and [Fe/H] for the test sample with those of Allende Prieto et al. (2004) and Valenti & Fischer (2005). Both solved for model atmosphere [M/H] and [Fe/H] separately whereas we equate the two. Therefore we compare our [M/H] $\equiv$ [Fe/H] with their [Fe/H] values in Figure 2.4.

For the 30 test sample stars, we find mean offsets ($X - X_{external}$, where "X" is a derived parameter) with respect to the results of Allende Prieto et al. (2004) of -12 $\pm$ 15 K (σ = 81 K), -0.04 $\pm$ 0.01 dex (σ = 0.04 dex), and 0.00 $\pm$ 0.01 dex (σ = 0.06 dex) for T_{eff}, log g, and [Fe/H] respectively. Good agreement for all the parameters is found due to the very similar analysis techniques. Compared to the results of Valenti & Fischer (2005), we find mean offsets of -117 $\pm$ 14 K (σ = 75 K), -0.02 $\pm$ 0.02 dex (σ = 0.10 dex), and -0.08 $\pm$ 0.01 dex (σ = 0.07 dex) for T_{eff}, log g, and [Fe/H] respectively. Our T_{eff} and [Fe/H] values for the test sample are systematically lower than their derived values over the entire range of the sample. Generally, this may be explained by systematic differences in techniques. The Valenti & Fischer (2005) analysis is purely spectroscopic, while ours relies on outside constraints of the stellar T_{eff} and log g. However, the exact reason for the systematic discrepancies is unknown. While detailed study of the causes of inter-study systematic differences is a worthwhile pursuit, it is beyond the scope of this

investigation.

Overall, the results of our analysis of the test sample are broadly consistent with the results of Allende Prieto et al. (2004) and Valenti & Fischer (2005) despite the differences in techniques and model atmospheres used. We conclude that our results for the primaries in the binary sample are robust against major external errors and precise enough to check for internal consistency with the results of our analysis of the M dwarf secondaries.

2.3 Application of the V98 Technique

Our initial goal was to determine whether the V98 approach used with existing model atmospheres yielded metallicities for M dwarfs that were consistent with those derived for solar-similar stars with well established methods. We did this by analyzing the secondaries in our binary sample and comparing the derived metallicities with those that we determined for the corresponding primaries. In this section we discuss our application of this technique and the necessary details. We refer the reader to the V98 paper for more specifics.

In the V98 approach, synthetic spectra are matched to two observed spectral regions of an M dwarf spectrum. One region contains strong atomic lines (8670 – 8700 Å) and another contains a TiO bandhead (7078 – 7103 Å). To duplicate this method as closely as possible, we synthesized a grid of spectra for the two spectral regions using a version of SYNTH (Piskunov 1992) that was modified to handle the molecular equation of state as described by V98, NextGen model atmospheres (Hauschildt et al. 1999), and the V98 line

lists. Our grid of spectra had an increased T_{eff} range, 3000 – 4000 K in steps of 100 K, compared to V98 in order to cover the anticipated range of our sample. Microturbulence was set to zero during the synthesis of the grid. Our implementation used the same χ^2 minimization algorithm that was used in our analysis of the primaries to determine the astrophysical parameters, T_{eff}, log g, [M/H], and η which gave the best match between the synthetic and observed spectra. Additionally, as in V98, we included two continuum normalization factors, a zero-point and slope, per analyzed echelle order as free parameters in the fit. There were eight fit parameters in total.

The spectral points used to constrain the fit include the entire TiO bandhead region and the atomic line profiles to begin with. For a particular iteration in the parameters of the minimization function, interpolation in the synthetic spectrum grid using the same procedure as V98 yielded synthetic spectra for the values of T_{eff}, log g, and [M/H]. Macroturbulent and instrumental broadening was added after interpolation by convolution with a Gaussian. After the first best-fit was found, points in the bandhead region where the fit deviated from the observed spectrum by 0.15 residual intensity units were flagged to be ignored and the fit was re-run. The process continued iteratively as the rejection limit was decreased to 0.04 residual intensity units in steps of 0.01. The final parameters were arrived at after the last rejection iteration.

We analyzed the spectra taken for the M dwarf secondaries in the binary sample using our adaptation of the V98 technique. We found that the

metallicities derived in this manner average 0.56 dex lower than the [Fe/H] values of the primaries. We considered that this systematic inconsistency could be reduced by improvements in the analysis method and model atmospheres as described in the next section.

2.4 Modifications to the V98 Approach

Motivated by the inconsistency found above, we made a systematic study of the V98 technique. We implemented some potential improvements in our spectrum synthesis code, cool-star model atmospheres, and analysis technique. We also derived empirical surface gravity and abundance trend relationships which we used to constrain our analysis. The following subsections detail our work in this area.

2.4.1 Spectrum Synthesis Code

Following V98, we used SYNTH2 to generate synthetic spectra in our original application described in the previous section. For the new analysis we chose to use MOOG (Sneden 1973) for spectrum synthesis. We have modified MOOG to extend its capabilities to the M dwarf domain, while also maintaining consistency with its pre-existing functionality. This allowed us to use MOOG for the analysis of the solar-similar primaries and M dwarf secondaries.

We altered MOOG so that the chemical equilibrium calculations were carried out for an extensive set of molecules and atoms. We identified the set of species to include by examining the PHOENIX version 13.13.00E partial

pressure tables. We selected all molecular species that have partial pressures greater than $10^{-7}\%$ of the total gas pressure above 1500 K. The atomic species included were the neutral and singly ionized species of any elements that are a part of the selected molecules or needed specifically for continuous opacities. The equilibrium calculation included 16 different elements and 40 molecules for a total of 72 species. The list of the species and their corresponding set of linear pressure equations are given in Appendix A.

We also updated the molecular data in MOOG. Using the PHOENIX partial pressure tables, we fit fourth order polynomials as a function of $\theta \equiv$ log (5040/T) to each molecular species' partial pressure to construct equilibrium constants. We adopted the dissociation energies from Sauval & Tatum (1984). The equilibrium constant fits are valid over the range in $1500 \leq \mathrm{T} \leq$ 10000 K. We checked the equilibrium constants against the direct calculations from the partition functions of Sauval & Tatum (1984). No major discrepancies were found and we adopted the equilibrium constants from the fits to the PHOENIX partial pressure data to maintain consistency with the model atmospheres we used in our analysis. The determined polynomial coefficients for the equilibrium constants and adopted dissociation energies are included in Appendix A.

Molecular energy level populations, which are needed to calculate line opacities, are normally calculated from the molecule's constituent elements' partition functions in MOOG. We chose to use the molecular partition function directly for TiO, the only molecular species included in our line list for

spectrum synthesis, to maintain consistency with the molecular equilibrium calculations. We modified MOOG to use the partition function for $^{48}Ti^{16}O$ (the dominant isotope) calculated by Kurucz (1999), which agrees well with that given by Sauval & Tatum (1984). The adopted expression for the TiO partition function used is also given in Appendix A.

We also adopted the TiO dissociation energy, $D_0 = 6.87^{+0.07}_{-0.05}\ eV$, from the lab measurement of Naulin et al. (1997). This is the same value as given by Huber & Herzberg (1979), Sauval & Tatum (1984), and the JANAF Thermochemical Tables (Chase et al. 1985), and 0.06 eV lower than, but within the uncertainties of, the lab measurement of Dubois & Gole (1977).

2.4.2 Model Atmospheres

We computed a new grid of model atmospheres with PHOENIX (version 13) for our revised M dwarf analysis. These models are an updated version relative to the NextGen version models used by V98 and in §3. Important updates and revisions since the NextGen models were released are discussed by Kučinskas et al. (2005). Additionally, we used the TiO partition function mentioned in the previous subsection, which is roughly a factor of three lower than that used in all previous versions of PHOENIX. We also used the recently updated solar abundances presented in the compilation by Asplund et al. (2005). Most relevant for this work was the reduction of the solar abundances of C, O, and Ti, by 0.17, 0.21, and 0.12 dex respectively from the values used in previous versions. Also, all of the model atmospheres were computed assuming

a microturbulent velocity of 2 km s^{-1}. The new model grid spans the range in parameters $3000 \leq T_{eff} \leq 4000$ K, $4.5 \leq \log g \leq 5.5$, and -1.0 $\leq$ [M/H] $\leq$ +0.5 in steps of 100 K, 0.5 dex, and 0.5 dex respectively.

2.4.3 TiO Line Data

One key aspect of the V98 analysis was their inclusion of a strong TiO bandhead (γ R_2 0 – 0) as a fit constraint. While molecular bandheads typically have good temperature sensitivity, they are complex and require significant consideration of line data for proper synthesis. Additionally, a minimum level of TiO line "haze" exists throughout the visible and near-IR regions of M dwarf spectra. This necessitates the inclusion of TiO lines for realistic spectrum synthesis in the atomic line spectral regions that we include in our analysis. We adopted the TiO line list of Plez (1998), which is based on the most recent laboratory measurements and theoretical calculations. We chose to use the version of the list that has the laboratory line positions substituted for the calculated values where they are available. We used the formula given by Schweitzer et al. (1996) to calculate the van der Waals damping for molecular lines.

The TiO line list of Plez (1998) includes data for 15.7 million lines and includes many more lines than have a meaningful impact on the spectra of M dwarfs. To save computational time, we used a similar procedure as V98 to determine a strength cutoff for lines to be included in our line lists. We calculated the strength, S, based on the formula given in V98, for all the lines

in the three spectral regions we use in our analysis. The formula is:

$$S = log(agf\lambda) - \theta\chi, \tag{2.1}$$

where a is the isotopic abundance fraction, g the statistical weight, f the oscillator strength, λ the wavelength, and χ the lower level excitation energy.

For each of the three regions separately, we progressively lowered the strength cutoff value from the maximum value by 0.5, until spectra generated for a characteristic model atmosphere did not change by more than 0.5%. This resulted in strength cutoff values of -0.30, -0.51, and -0.26 for the spectral regions 7080 – 7100, 8320 – 8430, and 8650 – 8700 Å and yielded 16,667, 35,695, and 14,487 TiO lines respectively. A comparison of spectra synthesized using MOOG with the V98 line list and the new line list showed that the revised log gfs in new list yielded smaller depths for the 7088 Å bandhead at all model temperatures. For unsmoothed spectra generated with a model atmosphere having $T_{eff} = 3500$ K, the V98 line list gave residual intensities an average of 0.07 lower than the new line list.

2.4.4 Atomic Line Data

In addition to the TiO bandhead around 7088 Å, V98 focused on fitting five relatively strong atomic lines in a second spectral interval, 8670 – 8700 Å. As part of our modification to the original technique, we have expanded this list of lines to include 11 more.

We examined our observed spectra for new lines that met our search

criteria, which was similar to that used in V98. Our first criterion was that the new lines must have fractionally small amounts of TiO line blending. This necessitated the use of fairly strong lines as a minimum level of molecular line haze exists throughout the observed spectral regions. The second criterion was that they must also be strong enough in a solar spectrum for the purpose of determining astrophysical log gfs.

The new lines we selected occupy a spectral interval adjacent to the original one and in the same echelle order, 8650 – 8670 Å, and a second echelle order, 8320 - 8430 Å, in our observed data. This makes for convenient spectral synthesis and increases the constraint on the continuum normalization, which introduces two free parameters into the fit for each echelle order utilized. The new lines also include a new elemental species, Ca. One of the lines added is a member of the Ca II "infrared triplet."

For consistency, we determined astrophysical log gfs for the lines originally used by V98 and the new ones used here. We did this using the same procedure described in §2.2.1. Eleven of the lines have accurate van der Waals damping data from Barklem et al. (2000), which we took advantage of. For the remaining five lines we used the approximation of Unsöld (1955) enhanced by a factor of 2.5 as was done by V98. The final data for the 16 lines is given in Table 2.5. Our log gf values are essentially identical with the V98 values for the two Fe I lines originally used. The log gfs for the Ti lines are different from the V98 values by larger amounts due to the 0.12 dex lower value for the solar Ti abundance that we adopted. Also, two of the Fe I lines that we

use to analyze the M dwarfs were also used in the analysis of the solar-similar primaries.

We constructed an atomic line list for our M dwarfs using data obtained from the Vienna Atomic Line Database (VALD, Piskunov et al. 1995; Kupka et al. 1999). We queried VALD for lines in the three spectral regions we analyze with assumed model temperatures of 3000 and 4000 K. The lists for each temperature were merged and we substituted our astrophysical gfs for the 16 lines we fit. These atomic line lists were then combined with the TiO line lists mentioned above to create the final line lists for our analysis.

2.4.5 Microturbulence

The use of a variable parameter representing a depth independent, small scale (relative to a photon mean free path) velocity distribution, microturbulence, is standard procedure in high precision, one-dimensional spectroscopic analyses. Following convention, we allowed microturbulence to vary in our analysis of the primaries in the binary sample. Also, we elected to introduce a variable microturbulence in our analysis of the M dwarfs. Microturbulence, unlike macroturbulence, must be accounted for in the spectral synthesis itself and cannot be be added by a later convolution. Therefore, a pre-synthesized grid of spectra for our purpose would have to include a range of values for a fourth parameter. We chose to abandon this approach as we had little indication of what the microturbulence values would actually be, and because the already significant grid creation time would be multiplied by the number of

microturbulence grid nodes.

Our revised technique was similar to that used in the analysis of the solar-similar primaries. A new model atmosphere was interpolated from the grid mentioned in §2.4.2 using the interpolation method described in §2.2.2 for each iteration in the stellar parameters by the χ^2 minimization algorithm. With that model atmosphere and the microturbulence suggested by the fitting program as inputs, MOOG was used to generate a synthetic spectrum. Macroturbulence and instrumental broadening were added by a convolution at this point. Then the synthetic spectra were resampled to the discrete wavelength scale of the spectrograph and compared to the observed spectra. We note that the individual microturbulences determined for the analyzed stars are lower by ~ 1 km s^{-1} from the value used to generate the model atmospheres. However, a change of the microturbulence adopted for generating the model atmospheres of this magnitude would not have a noticeable impact on their structure.

2.4.6 Surface Gravity

All spectroscopic analyses can benefit from outside constraint on any of the needed stellar parameters. In the case of M dwarfs, current theoretical models are not yet to the point where they can be used for this purpose. Fortunately, increasing attention has been focused on measuring the physical properties of M dwarfs since the V98 analysis. Specifically, the direct measurements of M dwarf masses, M, and radii, R, have permitted the calculation

of empirical surface gravities for a sample of M dwarfs.

We have deviated from the purely spectroscopic approach of V98 by calculating and adopting an empirical log g – M relationship. We compiled all the known M dwarf radii measurements with precisions better than 16%. The measurements come from the observations of M dwarfs in eclipsing binary systems (Metcalfe et al. 1996; Ribas 2003; Torres & Ribas 2002; Maceroni & Montalbán 2004; Maxted et al. 2004; Creevey et al. 2005; López-Morales & Ribas 2005) and interferometric observations of single M dwarfs (Lane et al. 2001; Ségransan et al. 2003; Berger et al. 2006). We also compiled the high precision mass measurements for the stars in the eclipsing binary systems. We calculated the masses for the single stars from the M_K – M relationship in Delfosse et al. (2000). The K magnitudes and parallaxes needed to calculated the M_K values were taken from the Two Micron All Sky Survey (2MASS) point source catalog (Cutri et al. 2003) and the *Hipparcos* (Perryman et al. 1997) catalog respectively. Uncertainties in the masses calculated in this manner were assumed to be 10%. We then calculated log g for each object from the mass and radius data. Uncertainties in both mass and radius were propagated through formula to give the the associated uncertainty in log g.

With this this dataset, we fit a third order polynomial to the surface gravity values as a function of mass. The data points were weighted according to their uncertainties in both parameters. Twenty-eight independent points were considered in the fit, with values spanning the range in mass: 0.123 –

0.621 $M_{\odot}$ and radius: 0.145 – 0.702 $R_{\odot}$. The function found was

$$\log g = 5.491 - 3.229 M_{\star} + 5.949 M_{\star}^2 - 4.929 M_{\star}^3, \tag{2.2}$$

where $\log g$ is in cgs units and M is in solar units. The standard deviation for this relationship is 0.08 dex and the data and fit are plotted in Figure 2.5.

Our revised technique for analyzing M dwarfs makes use of equation (2.2) to fix $\log g$. For the M dwarfs in our binary sample, we calculated M_K magnitudes based on 2MASS photometry and *Hipparcos* parallaxes. We converted those values to masses based on the M_K – M relationship in Delfosse et al. (2000) and then used these masses to estimate $\log g$ from equation (2.2). The theoretical $\log g$ – M and the M_K – M relationships are independent of stellar metallicity, unlike the M_V – M relationship (Baraffe et al. 1998). Therefore the use of both relationships is appropriate for our purposes. This approach eliminates one parameter to be determined from the fitting process and permitted a more robust test of the model atmospheres.

2.4.7 Abundance Trends

V98 fit synthetic spectra to various spectral features to derive a single abundance metric, metallicity. The shapes of these features are directly related to the abundances of three species, O, Ti, and Fe, and indirectly to the abundances of many other species through their affect on the chemical equilibrium. We retained this approach and added a Ca line as a further constraint. The determination of the individual abundances of these elements is

not possible at this point as the varied features are needed to break the degeneracies between the parameters that we determined from the spectra (T_{eff}, [M/H], ξ, η, and 6 continuum normalization factors). Given this, we had to adopt relationships between the abundances of various elements, [X/H], and our varying abundance parameter, [M/H].

First, we assumed [Fe/H] = [M/H], as we also did for the solar-similar primaries. Then we calculated relationships between alpha element and carbon abundances and [Fe/H] using the field star abundance data of Allende Prieto et al. (2004). For the alpha elements, we combined the elemental abundances of O, Mg, Si, Ca, and Ti into a single data set. Ti is not strictly an alpha element, but the observed trend of its abundance with [Fe/H] closely matched the other elements in the range of values covered so we included it. We fit these elemental abundances with a single parameter, [α/H], as a linear function of [Fe/H]. The expression found was

$$[\alpha/\mathrm{H}] = 0.11 + 0.87[\mathrm{Fe/H}] \tag{2.3}$$

for 607 data points with a standard deviation of 0.10 dex. This formula obviously gives super-solar abundances for the alpha elements at [Fe/H] = 0 and, as Allende Prieto et al. (2004) noted, suggests that either the Sun has an unusual abundance pattern compared to solar-neighborhood stars or that the data is affected by systematic errors. Adopting this formula means that our analysis was not strictly differential to the Sun. Rather, our revised method was differential to an artificial [M/H] = 0 model with mean solar neighborhood

abundances. This approach was not ideal, but was necessary to maximize our ability to analyze a sample of stars, rather than a single individual star.

We also constructed a dataset of C abundances and fit [C/H] as a linear function of [Fe/H]. The resulting formula for 101 data points is

$$[\mathrm{C/H}] = -0.01 + 0.62[\mathrm{Fe/H}] \tag{2.4}$$

and has a standard deviation of 0.14 dex. The alpha element and carbon abundance data are plotted as functions of [Fe/H] in Figure 2.6 along with the fits to the data given in equations (2.3) and (2.4).

For all other elements we assumed [X/H] = [Fe/H]. Of these, Na is particularly important because it is the dominant electron donor in M dwarf atmospheres. It was found that [Na/Fe] $\approx$ 0 for [Fe/H] > -1.0 by Reddy et al. (2003).

2.5 Results and Error Analysis

The results of our analysis of the M dwarf secondaries using the revised technique described in §2.4 are given in Table 2.6. Plots of the observed spectrum and best fit for the coolest M dwarf, HIP 12114B, are shown in Figures 2.7 and 2.8. The mean offset of the derived metallicities for the five M dwarfs from the expected values as given by their corresponding solar-similar companion ($[\mathrm{M/H}]_{secondary} - [\mathrm{M/H}]_{primary}$) is -0.08 $\pm$ 0.04 dex (σ = 0.07 dex).

The binary sample can be used for evaluating the errors in our technique because the derived metallicities are independent of the values derived

for the primaries. We calculated the RMS deviation for the sample metallicities to be 0.11 dex by adding the average offset and it's standard deviation in quadrature. Assuming the systematic offset is a product of random errors and a symmetrical distribution, the RMS value is the standard deviation of a Gaussian probability distribution with a mean of zero. We added this value in quadrature to the median uncertainty in our derived metallicities for the primaries metallicities, 0.06 dex, to get 0.12 dex. We adopt this as the uncertainty in [M/H] for our technique.

With respect to the log g values determined from our empirical log g – M relationship, we considered the uncertainty in the empirical relationship and the estimated masses needed for it. We assumed errors of 10% in the estimated masses from the empirical relationship of Delfosse et al. (2000). Propagating that through equation (2.2) yielded associated uncertainties of 0.06 dex in log g. Adding that value in quadrature to the uncertainty of equation (2.2), 0.08 dex, yielded 0.10 dex, our estimated uncertainty in the log g values for our M dwarfs.

The primary constraint of the stellar T_{eff} in our analysis technique comes from the TiO bandhead used in the fitting process. Molecular bandheads in general are very sensitive to the temperature and composition, but not the gas pressure of the physical environments in which they form. We therefore used the uncertainty in our derived [M/H] values, which were determined externally, to estimate the errors in our derived T_{eff} values. We repeated our analysis of the five M dwarfs with [M/H] fixed to values 0.12

dex above and below the best fit value. The parameters T_{eff}, ξ, and η were allowed to vary and log g was fixed to the value determined from equation (2.2). We calculated the deviations of the five pairs of T_{eff} values from the best fit values give in Table 2.6. The average of the 10 deviations is 48 K and we adopt this as the standard uncertainty in our derived T_{eff} values. As a check of the independence of the T_{eff} and log g parameters in our analysis, we repeated the above procedure with log g fixed to values 0.10 dex above and below that given by equation (2.2). We found an average deviation for T_{eff} of 4 K, an insignificant change which supports our supposition.

Finally, we adopted the same standard uncertainties in our derived microturbulence and macroturbulence values as for the primaries, 0.15 and 0.20 km s^{-1} respectively.

2.6 Discussion

We have carried out a test of the V98 technique to determine M dwarf metallicities using an analysis of binary star pairs. Our result is that the V98 technique yielded values that were systematically too low. Motivated by this, we have made modifications to the original technique and a re-analysis of the M dwarfs secondaries validates our new approach. Our modifications include expanding the stellar analysis code MOOG, adopting relationships for the abundances of the alpha elements and carbon to iron, using TiO line data from Plez (1998), inclusion of new atomic lines and data, introducing a variable microturbulence, and the use of an empirical surface gravity relationship. We

have also made improvements in the PHOENIX model atmospheres that could have implications beyond those noted in our focused study.

Our modified technique, in conjunction with new model atmospheres, has yielded a technique for determining M dwarf metallicities consistent to 0.11 dex with the techniques applied to solar-similar stars. We have assumed that the mean offset in derived metallicities between the primary and M dwarf parent samples is actually zero and that the observed offset of -0.08 $\pm$ 0.04 dex is due to random errors. The observed offset is actually 2σ from zero and might be indicative of an unknown systematic in our technique or the model atmospheres. We estimated the uncertainties in our derived stellar parameters for the M dwarfs to be 48 K, 0.10 dex, 0.12 dex, 0.15 km s^{-1}, and 0.20 km s^{-1} for T_{eff}, log g, [M/H], ξ, and η respectively based on the assumption of no systematic errors. In the studies of M dwarfs discussed in Chapters 3 and 4, we adopt these values as the standard uncertainties in our analysis method when used with the particular model atmospheres described here.

Although we find good results for our study of the five binary pairs presented here, we are aware of several issues that could affect the results of our analyses of the primaries and the M dwarfs. In our analysis of the solar-similar primaries, there are potential systematics introduced by using the $(B - V)$ – T_{eff} relationship of Ramirez & Meléndez (2005). Applying their relationship to the Sun using the most probable solar color $(B - V)_{\odot} = 0.64$ (Holmberg et al. 2006), yields a $T_{eff} = 5706$ K, which is 71 K lower than the true solar T_{eff}. We have estimated the errors in our derived metallicities for

the primaries due to uncertainties in our adopted T_{eff} values on the same order as this difference (§3.3), but our approach ignores the potential systematics in the Ramirez & Meléndez (2005) relationship for which it could be evidence. Nonetheless, we consider the T_{eff} values derived from the Ramirez & Meléndez (2005) relationship to be preferable to spectroscopically determined values for solar type stars which have their own potential problems (Ramirez & Meléndez 2004).

Additionally, the model atmospheres we used in our analysis of the the primaries used the "old" solar abundance values given by Anders & Grevesse (1989) and were not consistent with the models we used to analyze the M dwarfs. However, the abundances of the species that differed the most between the model versions used, C and O, affect the models of the primaries much less than the M dwarfs models. Model atmospheres of M dwarfs are heavily influenced by molecular opacities which depend directly and indirectly on the abundances of C and O. In comparison, the 1D model atmosphere structures of solar-similar stars are only minimally affected by opacities related to the C and O abundances at the level at which they have been altered (0.17 and 0.21 dex respectively).

All abundance analyses very much depend on the adopted line, atomic, and molecular data. In the best case scenario the critical data are measured in laboratories with very precise methods. Alternatively, the data can be determined for a reference star like the Sun and relative, but still very informative, abundance measurements can be made. Even still, the data can only be known

to finite precision and the unavoidable errors can introduce systematics. Our M dwarf analysis is dependent on more data than is generally needed in a typical analysis of solar-type stars. This is due to the additional degrees freedom in the chemical equilibrium and the large number of lines that must be considered. Of particular importance are the TiO dissociation energy and line log gfs because of their direct influence on the calculated synthetic spectra.

We repeated our analysis of the M dwarfs in order to quantify the sensitivity of our technique to errors in these parameters. To test the influence of the dissociation energy we increased and decreased our adopted value (6.87 eV) by 0.05 eV, which is the magnitude of the estimated uncertainty in the value. We found that there was only a general trend in the results from this analysis. When the dissociation energy was decreased all the derived effective temperatures and metallicities went up by about 40 K and 0.1 dex respectively. From inspecting the equations of chemical equilibrium (see Appendix 1), we expected that either the temperature would have gone down, the metallicity to have gone up, or some combination of the two to compensate for the reduced partial pressure of TiO. However, what seems to happen is that reduced TiO partial pressure leaves more neutral Ti. This results in an increase in those line strengths. The complex interplay between fitting Ca, Ti, Fe, and TiO lines simultaneously leads to a strongly nonlinear response to changes in the adopted data.

When we repeated our analysis with the dissociation energy increased 0.05 eV the derived effective temperatures went up by about 25 K and the

metallicities were essentially unchanged. This was the result that was expected from the chemical equilibrium equations. The temperature has to be increased to account for the higher calculated partial pressure of TiO.

We tested the influence of the TiO line log gfs by increasing and decreasing them 0.1 dex. We found that generally the determined effective temperatures were unchanged and the metallicities 0.1 dex higher when the log gfs were reduced. When the log gfs were increased the determined effective temperatures went up about 25 K and the metallicities went down 0.05 dex. The first result is consistent with expectations, while the second is similar to the complex response elicited by decreasing the dissociation energy. The results from both of these investigations do support our error analysis because the size of the deviations are smaller than our estimated uncertainties. Errors in any of the other adopted data will not have effects on the analysis results as large as those from the TiO dissociation energy and line data.

Our technique for deriving the stellar parameters for M dwarfs relies on a number of assumptions that are not needed in analyses of solar-similar stars. These assumptions could potentially introduce systematic errors that are not obvious given our test sample size. Improvements in our technique, including determining the abundances of specific elements instead of just the global metallicity, would be possible if there were more robust ways to estimate the stellar T_{eff} and log g values as there are for solar-type stars.

Our derived T_{eff} values for the M dwarfs follow the expected trend and decrease smoothly with spectral type. However, when comparing these

values with the T_{eff} values as functions of spectral type in Table 4.1 of Reid & Hawley (2005), there is a systematic trend of increasing deviation with spectral type. For the earliest M dwarf in our sample (HIP 32423B, M0.5), there is essentially no difference in our derived T_{eff} and that given by interpolating in Table 4.1. For our sample, the deviation increases linearly with spectral type and is roughly 300 K for the latest M dwarf in our sample (HIP 12114B, M3.5). This comparison assumes that there is minimal dispersion in the spectral type – T_{eff} relationship, which is only true at a rough level (N. Reid, private communication) as such a relationship ignores the effects of metallicity. Also, only two M dwarfs, GJ 699 (Dawson & De Robertis 2004) and GJ 411 (Leggett et al. 1996; Ségransan et al. 2003) have known strictly empirical T_{eff} values based on measured bolometric fluxes and radii. However, the suggestion of a systematic error in our derived temperature scale should not be ignored lightly. As we have shown in §2.5, changes in our adopted stellar T_{eff} values of ~ 50 K correspond to differences of 0.12 dex in [M/H].

Also, we use an empirical relationship to constrain the surface gravity of our M dwarfs. Adopting values derived from fully validated evolutionary models might be more reliable because it would be possible to include the effects of varying stellar ages. We suggest that the biggest opportunity to advance detailed spectroscopic analyses of M dwarfs would by improving low-mass stellar evolutionary models. All stellar structure models depend on realistic model atmospheres as a boundary condition. Therefore, the new PHOENIX model atmospheres that we have validated in our analysis could be used to produce

more reliable evolutionary models.

Although there is much left to do in the area of abundance analyses for M dwarfs, the work presented here has been the next step in the detailed study of these neglected objects. We considered our new technique to be robust enough for application to two outstanding problems. The results from our applications are discussed in Chapters 3 and 4.

Table 2.1. Observed Binary Pairs

Name	Primary (A) Spectral Type	V	Secondary (B) Spectral Type	V	π (mas)[a]	ρ (arcsec)[b]
HIP 12114	K3 V	5.79	M3.5 V	11.66	138.72 ± 1.04	165[d]
HIP 26907	K1 V	8.56	M V[c]	13.21	31.90 ± 1.28	53[e]
HIP 32423	K3 V	8.80	M0.5 V	12.17	40.02 ± 1.22	31[d]
HIP 40035	F7 V	5.53	M2 V	12.26	44.47 ± 0.77	92[d]
HIP 102040	G5 V	6.44	M2.5 V	11.80	47.65 ± 0.76	125[d]

[a]ESA (1997); Perryman et al. (1997).

[b]Component separation on the sky.

[c]Based on position in an HR diagram.

[d]Poveda et al. (1994).

[e]Allen et al. (2000).

Table 2.2. Line Data Used in the Analysis of the Primaries

λ (Å)	χ (eV)	log gf Lab	log gf Solar
5956.6943	0.859	-4.498	-4.515
6065.4824	2.608	-1.410	-1.653
6079.0093	4.652	-1.020	-0.949
6082.7104	2.223	-3.570	-3.516
6085.2588	2.758	-3.050	-2.899
6093.6445	4.607	-1.400	-1.298
6096.6655	3.984	-1.830	-1.768
6127.9067	4.143	-1.399	-1.368
6229.2285	2.845	-2.830	-2.896
6232.6411	3.654	-1.223	-1.238
6240.6460	2.223	-3.173	-3.249
6246.3188	3.602	-0.877	-0.878
6252.5552	2.404	-1.767	-1.813
6265.1338	2.176	-2.550	-2.665
6270.2251	2.858	-2.609	-2.546
6322.6855	2.588	-2.430	-2.446
6411.6494	3.654	-0.717	-0.695
6430.8462	2.176	-1.946	-2.202
6481.8701	2.279	-2.980	-2.920
6498.9370	0.958	-4.689	-4.592
6593.8706	2.433	-2.420	-2.440
6597.5610	4.795	-0.970	-0.874
6609.1104	2.559	-2.692	-2.635
6810.2627	4.607	-1.000	-0.959
6828.5913	4.638	-0.820	-0.810
6841.3389	4.607	-0.710	-0.645
6843.6558	4.548	-0.830	-0.817
6858.1499	4.607	-0.940	-0.931
8327.0674	2.200	-1.525	-1.575
8688.6426	2.170	-1.212	-1.236

Table 2.3. Derived Parameters for the Primaries

Name	T_{eff} (K)	σ	log g (cgs)	σ	[Fe/H]	σ_l	σ_t	σ_g	σ	ξ (km s^{-1})	η (km s^{-1})
Sun	5777[a]	...	4.44[a]	...	0.00[a,b]	...	...	...	...	1.24	1.90
HIP 12114	4867	119	4.64	0.04	-0.12	0.01	0.04	0.02	0.05	0.84	1.44
HIP 26907	5054	122	4.60	0.10	+0.03	0.01	0.06	0.01	0.06	0.88	1.60
HIP 32423	4730	117	4.66	0.03	-0.23	0.01	0.02	0.01	0.03	0.69	0.81
HIP 40035	6262	102	4.30	0.10	-0.02	0.02	0.06	0.02	0.07	1.69	6.52
HIP 102040	5737	111	4.49	0.22	-0.14	0.01	0.06	0.01	0.06	1.16	2.10

[a]Fixed.

[b]The quantity log $\epsilon(\mathrm{Fe})_{\odot} = 7.45$.

Table 2.4. Determined Parameters for the Test Sample Stars

	Allende Prieto et al. (2004)			Valenti & Fischer (2005)			This Study		
Name (HIP)	T_{eff} (K)	log g (cgs)	[Fe/H]	T_{eff} (K)	log g (cgs)	[Fe/H]	T_{eff} (K)	log g (cgs)	[Fe/H]
544	5353	4.55	0.03	5577	4.58	0.11	5360	4.54	0.00
3093	5117	4.58	0.13	5221	4.45	0.16	5144	4.56	0.15
3765	4980	4.65	-0.25	4944	4.51	-0.27	4881	4.65	-0.30
3821	5801	4.47	-0.40	5941	4.44	-0.25	5710	4.30	-0.41
7513	6100	4.17	0.02	6213	4.25	0.15	6089	4.12	0.03
7981	5138	4.60	-0.04	5181	4.53	-0.04	5088	4.59	-0.06
8362	5257	4.58	-0.04	5327	4.54	0.03	5215	4.57	0.00
12777	6210	4.35	-0.08	6344	4.42	0.06	6162	4.28	-0.06
14632	5877	4.27	0.01	6032	4.31	0.16	5853	4.20	0.01
15457	5564	4.52	-0.11	5742	4.49	0.12	5553	4.50	-0.05
16537	5052	4.62	-0.06	5146	4.57	-0.03	4988	4.62	-0.05
16852	5914	4.12	-0.17	6038	4.21	-0.02	5824	4.03	-0.21
17420	4801	4.63	-0.02	4991	4.59	-0.06	4869	4.63	-0.04
19849	5164	4.61	-0.17	5151	4.57	-0.28	5046	4.61	-0.34
22449	6424	4.34	0.00	6424	4.29	0.03	6300	4.27	-0.05
23311	4641	4.63	0.26	4827	4.69	0.33	4746	4.61	0.34
24813	5781	4.33	-0.01	5911	4.37	0.12	5737	4.24	-0.01
26779	5150	4.58	0.14	5351	4.60	0.19	5145	4.58	0.09
37349	4889	4.62	0.04	4964	4.71	0.07	5012	4.63	0.09
27913	5820	4.49	-0.17	5882	4.34	-0.01	5818	4.47	-0.15
37279	6677	4.08	0.03	6543	3.99	0.00	6482	4.00	-0.13
40693	5331	4.57	-0.12	5361	4.46	-0.06	5340	4.56	-0.05
43587	5063	4.56	0.34	5235	4.45	0.31	5173	4.53	0.34
51459	6057	4.43	-0.17	6126	4.34	-0.07	5968	4.35	-0.23
53721	5751	4.35	-0.10	5882	4.38	0.04	5740	4.26	-0.07
56997	5402	4.57	-0.16	5488	4.43	-0.03	5409	4.56	-0.10
57757	6076	4.14	0.08	6161	4.22	0.18	6252	4.18	0.19
58576	5361	4.47	0.14	5565	4.56	0.27	5428	4.45	0.21
61317	5743	4.47	-0.35	5930	4.44	-0.16	5748	4.37	-0.30
64394	5910	4.44	-0.05	6075	4.57	0.07	5956	4.43	-0.00

Table 2.5. Line Data Used in the M Dwarf Analysis

Species	λ (Å)	χ (eV)	log gf	Damping
Fe I[a]	8327.067	2.20	-1.575	barklem
Ti I	8364.237	0.84	-1.684	unsöld
Ti I	8377.861	0.83	-1.521	unsöld
Ti I	8382.530	0.82	-1.549	unsöld
Ti I	8382.780	0.81	-1.652	unsöld
Fe I	8387.772	2.18	-1.562	barklem
Ti I	8396.898	0.81	-1.646	unsöld
Ti I	8412.358	0.82	-1.376	barklem
Ti I	8426.506	0.83	-1.136	barklem
Fe I	8661.897	2.22	-1.537	barklem
Ca II	8662.141	1.69	-0.716	barklem
Fe I[b]	8674.746	2.83	-1.846	barklem
Ti I [b]	8675.372	1.07	-1.465	barklem
Ti I[b]	8682.980	1.05	-1.762	barklem
Fe I[a,b]	8688.643	2.17	-1.236	barklem
Ti I[b]	8692.331	1.05	-2.098	barklem

Note. — The damping types are "barklem," which refers to data from Barklem et al. (2000) and "unsöld," which refers to the approximation of Unsöld (1955) enhanced by a factor of 2.5.

[a]Also used in the analysis of the solar-similar primaries.

[b]Used in the original V98 analysis.

Table 2.6. Derived Stellar Parameters for the M Dwarf Secondaries

Name	T_{eff} (K)	log g (cgs)	[M/H]	ξ (km s^{-1})	η (km s^{-1})	Δ([M/H])[a]
HIP 32423B	3722	4.82	-0.31	0.94	0.73	-0.08
HIP 40035B	3659	4.72	-0.12	0.91	1.60	-0.10
HIP 102040B	3556	4.76	-0.21	0.83	1.41	-0.07
HIP 26907B	3531	4.82	-0.13	0.91	0.82	-0.16
HIP 12114B	3444	4.98	-0.09	0.85	0.62	+0.03

Note. — Adopted uncertainties are 48 K, 0.10 dex, 0.12 dex, 0.15 km s^{-1}, and 0.20 km s^{-1} for T$_{eff}$, log g, [M/H], ξ, and η respectively.

[a]Deviation with respect to the value of the primary given in Table 2.3.

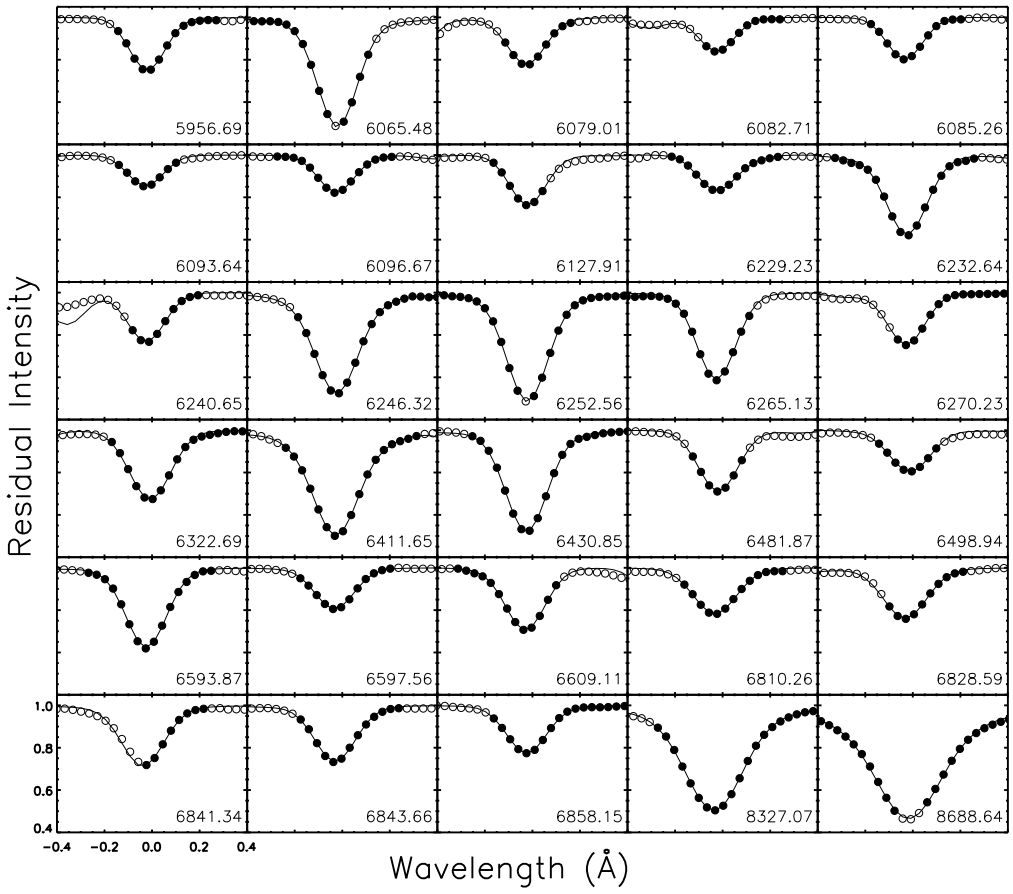

Figure 2.1 Best individual fits of synthetic spectra (solid lines) to the 30 Fe I line profiles (circles) of the solar-similar primary HIP 102040A. Line center wavelengths are given in the corresponding panel. The filled points were used in the fitting process; the open points were ignored. The number of points ignored in the cores of the strong lines depends on their strength and therefore varies with the stellar parameters.

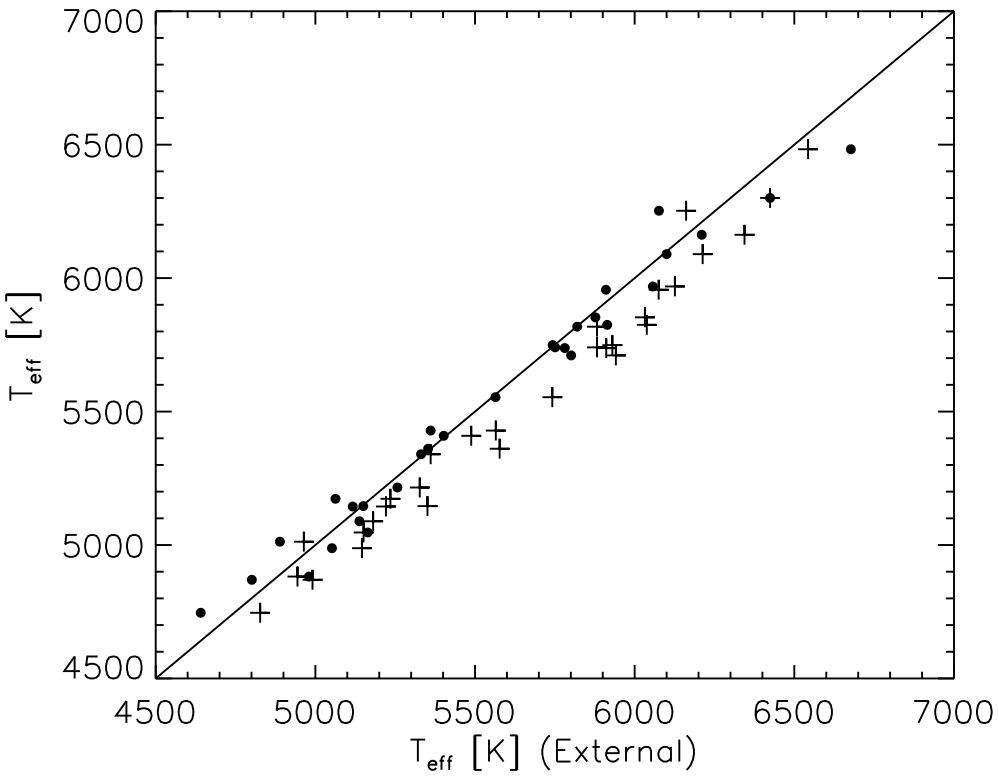

Figure 2.2 Comparison of our determined T_{eff} for the test sample with Allende Prieto et al. (2004) (circles) and Valenti & Fischer (2005) (plusses).

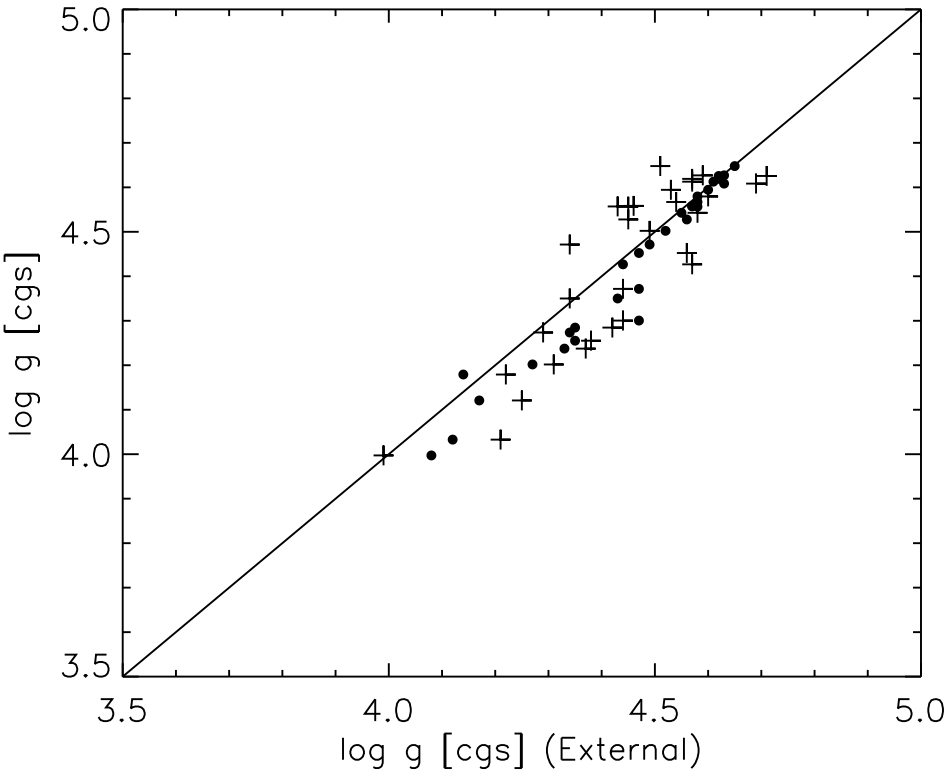

Figure 2.3 Same as Figure 2.2, except for log g.

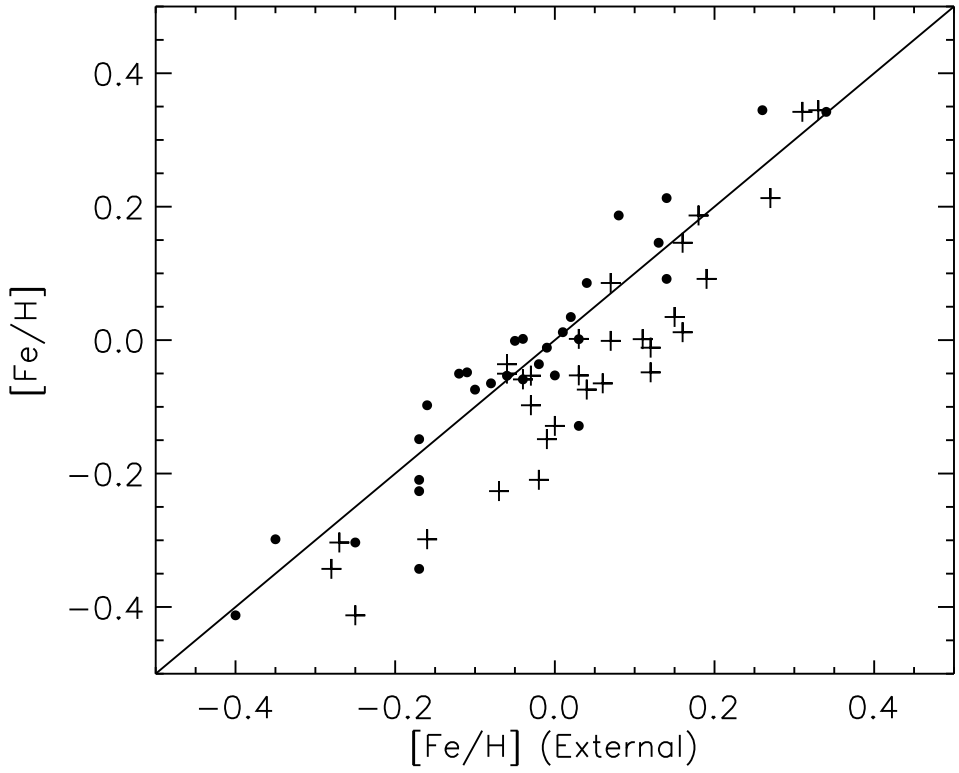

Figure 2.4 Same as Figure 2.2, except for [Fe/H].

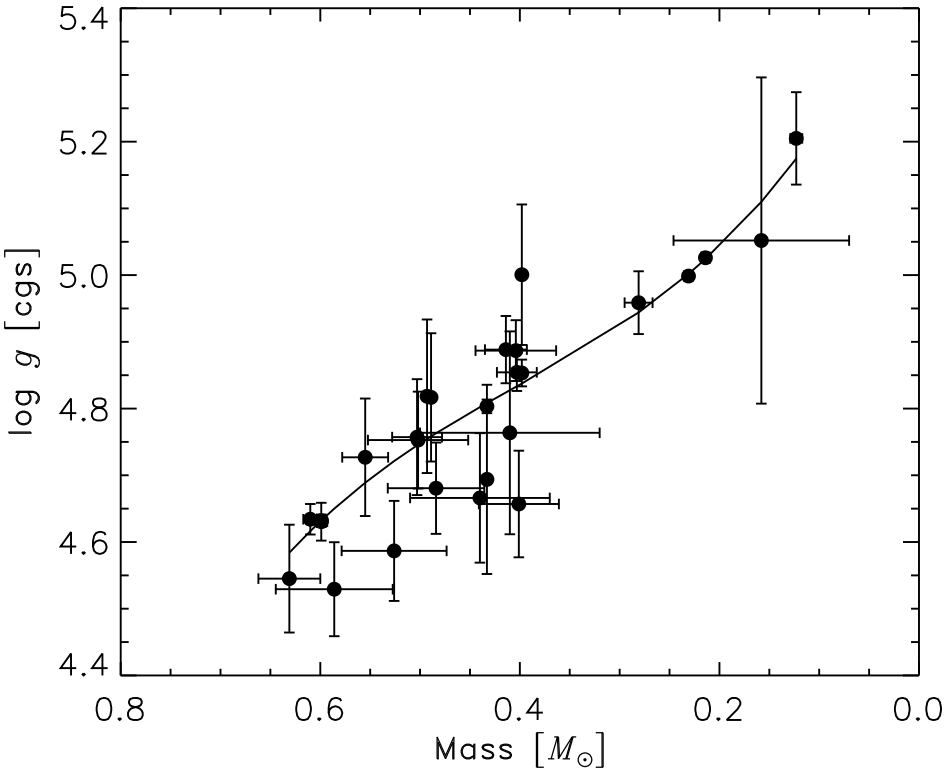

Figure 2.5 Plot of the empirical log g and M data (circles) and the fit given in eq. (2.2) (solid line).

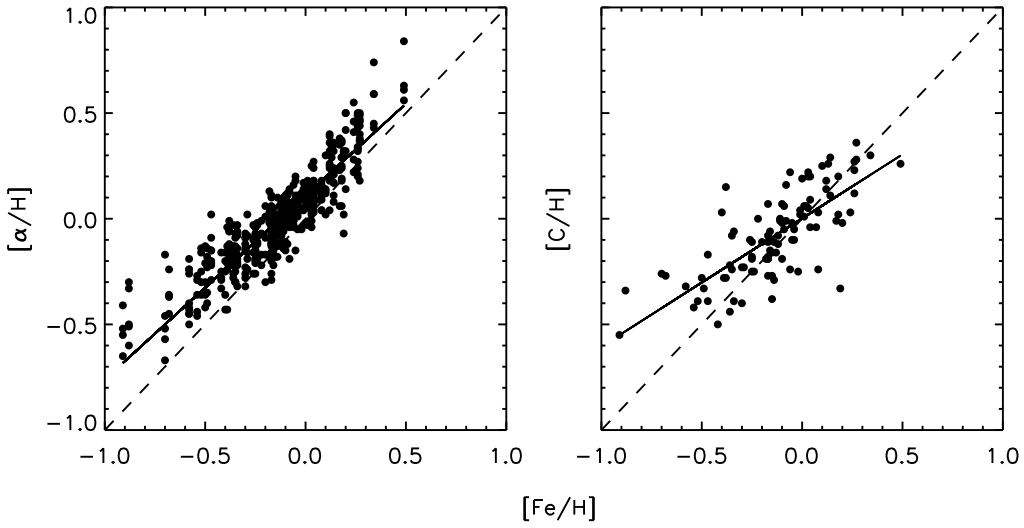

Figure 2.6 Alpha element (left panel) and carbon (right panel) abundances versus [Fe/H] (circles) from Allende Prieto et al. (2004). Error bars are omitted for clarity. The median uncertainties for the alpha element and iron abundances are 0.05 dex and 0.06 dex respectively. Carbon abundance uncertainties were set to 0.20 dex. The fits (solid lines) given in eqs. (2.3) and (2.4) and [X/H] = [Fe/H] relationships (dashed lines) are shown for comparison.

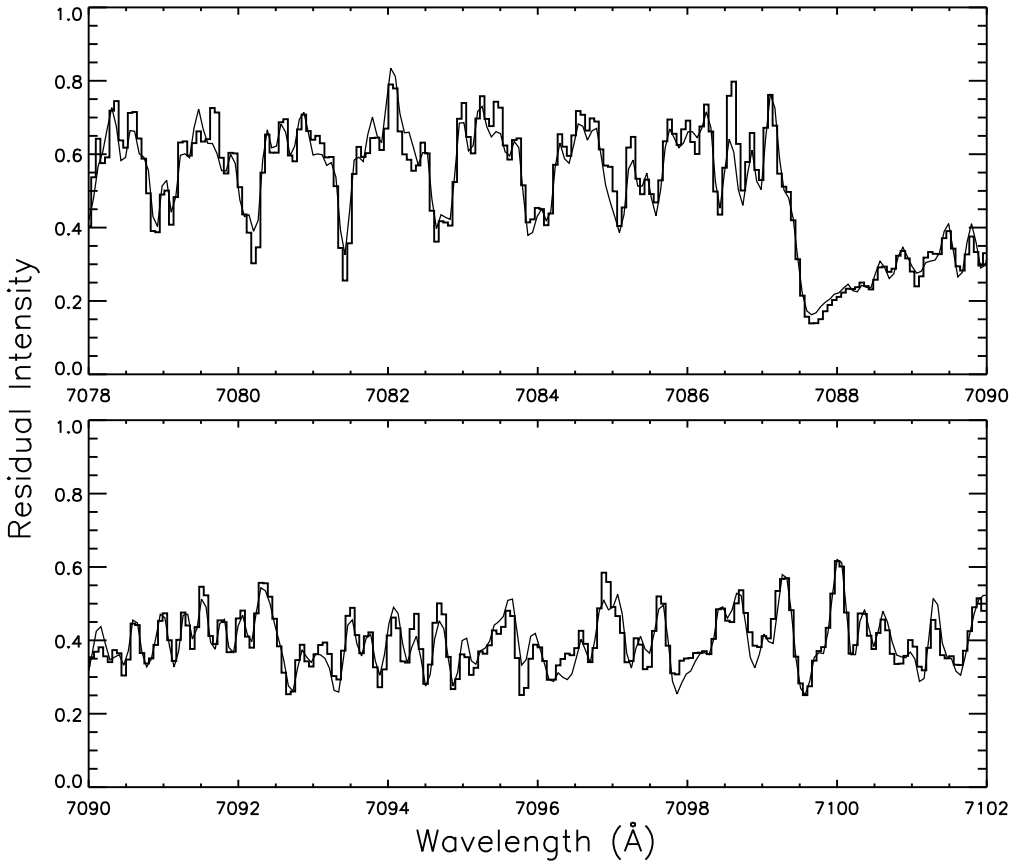

Figure 2.7 Spectral region near the strong TiO γ R_2 0 – 0 bandhead for HIP 12114B (histogram). The best fit used to determine the stellar parameters is over-plotted (solid line).

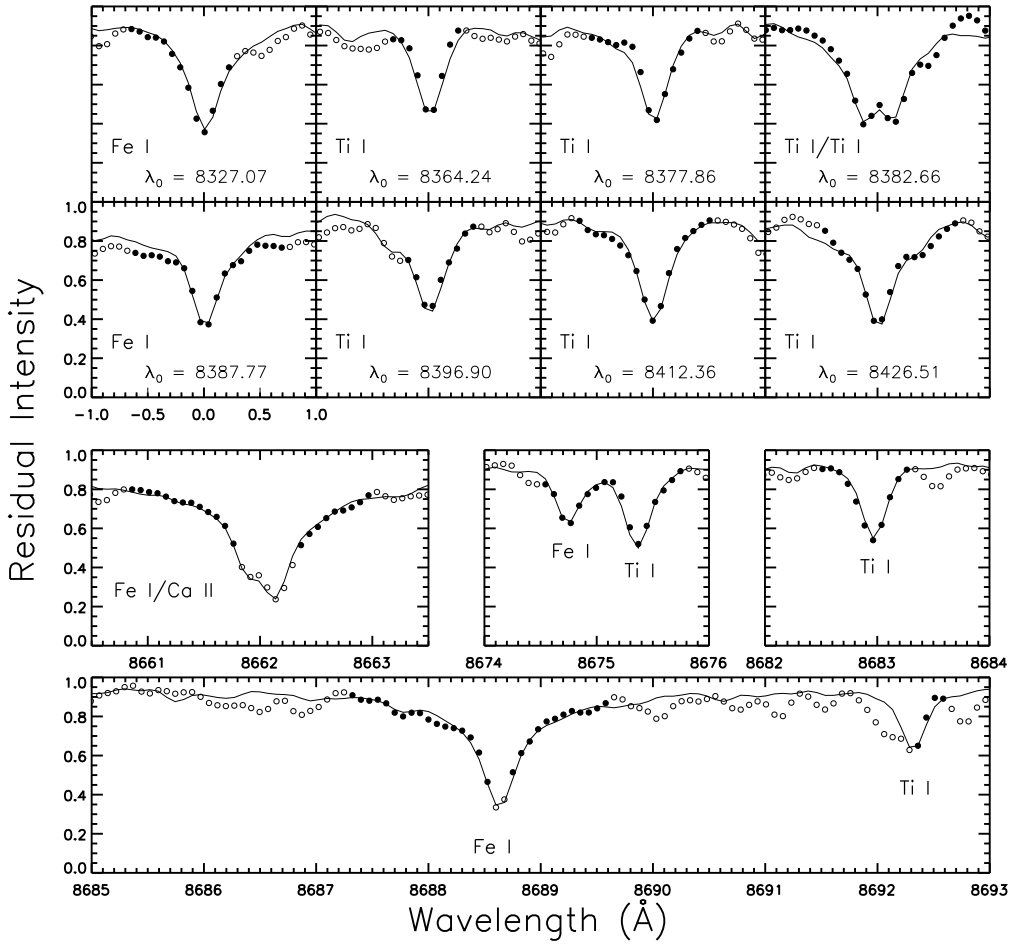

Figure 2.8 Fit of synthetic spectra (solid line) to atomic line profiles (circles) for HIP 12114B. The filled circles were used in the fitting process; the open circles were ignored. The panels are sorted by wavelength and the linear scaling in both parameters is the same throughout. The lines in each half, top and bottom, make up a contiguous spectral order in our observed spectra. The lines from 8674 – 8693 Å were used originally by V98; the others were added in this study. All apparent "lines" in the figure that aren't fit are actually multiple TiO lines.

Chapter 3

Metallicities of M Dwarf Planet Hosts

In a seminal paper, Gonzalez (1997) showed that the host stars to the first four extrasolar planets discovered had higher metallicities relative to the abundance distribution of stars in the solar neighborhood. This trend was found to continue as more stars were identified as potential extrasolar planet hosts with the Doppler method, and followed up with high precision abundance analyses (Fuhrmann et al. 1997, 1998; Gonzalez 1998, 1999; Gonzalez et al. 2001; Santos et al. 2000, 2003, 2004, 2005; Laws et al. 2003; Fischer & Valenti 2005).

The most likely explanation for the observed high metallicity trend is the so-called "primordial" hypothesis. That is, the high photospheric metal abundances in the host stars are relics of protostellar clouds and disks with a proportionally high metal content (Santos et al. 2004; Fischer & Valenti 2005; Gonzalez 2006). It is theorized that high-mass planet formation is increased in high metal-content protoplanetary disks under the core-accretion paradigm (Pollack et al. 1996). This hypothesis explains why more Jupiter and higher-mass planets have been detected around stars with high metallicities.

The majority of extrasolar planets have been found around FGK-type

stars as these are the stellar types that make up the majority of targets in Doppler surveys. High precision abundance analyses for these types of stars are relatively straightforward and, therefore, these are the types of stars for which the metallicity – giant planet connection has been established. However, because the majority of stars in the solar neighborhood are M dwarfs, a complete understanding of planet formation must necessarily include late-type stars.

To date, only two M dwarfs, GJ 876 and GJ 849, are known to harbor a Jupiter-mass companion (Delfosse et al. 1998; Marcy et al. 1998; Benedict et al. 2002a; Butler et al. 2006b). In addition to the astrometrically confirmed outer planet, another Jupiter-mass planet and a very low-mass planet in shorter-period orbits have been detected around GJ 876 (Marcy et al. 2001; Rivera et al. 2005). The M dwarfs GJ 436 (Butler et al. 2004), GJ 581 (Bonfils et al. 2005b), and GJ 674 (Bonfils et al. 2007) are hosts to Neptune-mass planets in short-period orbits. The planet around GJ 436 was very recently found to transit (Gillon et al. 2007), which makes it the first transiting Neptune-like exoplanet. Also, it was recently announced that GJ 581 hosts two additional super-Earth type planets ($M_p \sim 5$ and 8 $M_\oplus$, Udry et al. 2007).

Other planets, including a gas giant planet and a ~ 6 $M_\oplus$ planet, have been detected around suspected M dwarfs using the microlensing technique (Beaulieu et al. 2006; Gould et al. 2006). These host stars are still confused with the source stars and unavailable for further study. The first star that was identified as an extrasolar planet host with the microlensing technique was

thought to be an M dwarf (Bond et al. 2004), but recent observations have shown that it is actually a K dwarf (Bennett et al. 2006).

In this Chapter, I present the results of an abundance analysis of the planet hosting M dwarfs GJ 876, GJ 436, and GJ 581. In §3.1 I describe the spectroscopic observations of these objects. I present the analysis and results in §3.2. I discuss the implications of the results in §3.3.

3.1 Observations and Data Reduction

We observed GJ 876 with the 2.7 m telescope and 2dcoudé spectrograph at McDonald Observatory during the same observing run described in §2.1. We observed GJ 436 using the same telescope and instrument with the same setup on January 24, 2005 during an observing run that is also described in §4.1. Two 30 minute exposures were taken for both objects and co-added before reduction and extraction.

GJ 581 was observed using the 9.2 m effective aperture Hobby-Eberly Telescope (HET) at McDonald Observatory on May 11, 2006 with the High Resolution Spectrograph (HRS, Tull 1998) fed by a 2″optical fiber. The HRS was used in the R = 60,000 mode with a 316 gr mm^{-1} cross-dispersion grating. The cross-dispersion grating was positioned so that the break between the two CCD chips was at 7940 Å. Two 10 minute exposures were taken for GJ 581 and co-added before reduction and extraction.

CCD reduction and optimal order extraction were carried out using the

REDUCE package (Piskunov & Valenti 2002). The wavelength calibrations for each object were calculated based on the identification of roughly 1000 lines in thorium-argon emission spectra taken at the beginning of each respective night and have RMS precisions of 0.002 Å. The final one-dimensional spectra of GJ 876, 436, and 581 have S/N, of 430, 360, and 190 pixel^{-1} respectively at 8700 Å.

3.2 Analysis and Results

We analyzed the observed spectra of the three M dwarf planet hosts using the technique described in Chapter 2 and Bean et al. (2006a) to determine their metallicities. The results from our analysis are given in Table 3.1. We find [M/H] = -0.12, -0.32, and -0.33 for GJ 876, GJ 436, and GJ 581 respectively. We adopt the standard uncertainties in the parameters derived using this technique as also given in Chapter 2 and Bean et al. (2006a). They are 48 K, 0.10 dex, 0.12 dex, 0.15 km s^{-1}, and 0.20 km s^{-1} for T_{eff}, log g, [M/H], ξ, and η respectively.

Plots of the observed spectrum and best fit synthetic spectrum for GJ 876 are shown in Figures 3.1 and 3.2. Synthetic spectra computed with [M/H] values 0.3 dex lower and higher than the best fit value are also included in these Figures to illustrate the sensitivity of our measurement technique. The "high" and "low" metallicity synthetic spectra clearly do not match the observed spectrum as well as the synthetic spectrum computed with the determined stellar parameters.

An interesting aspect of this result is the closeness of the derived T_{eff} values for all three stars (range of 20 K) despite a range of 1.5 spectral types. The explanation for this is that metallicity and effective temperature are degenerate in the M dwarf spectral classification system. Therefore, only a detailed analysis such as the one we have employed can break the degeneracy and give a precise estimate of these parameters for an M dwarf.

3.3 Discussion

Butler et al. (2004) report an occurrence rate of Jupiter-mass planets ($0.5\ M_{Jup} < M < 13\ M_{Jup}$) with orbital semimajor axes $a < 1$ AU, of 3.5% around FGK-type stars. In contrast, Endl et al. (2006) found a frequency of 0.46% with an upper limit of 1.27% for the occurrence of Jupiter-mass planets around M dwarfs based on a dedicated survey of the spectral type. This result is similar to the value (0.7%) also reported by Butler et al. (2004) based on a survey of 150 M dwarfs with potential overlap with the Endl et al. (2006) sample. There have been no detections of so-called "hot Jupiters" ($a \sim 0.04$ AU) around M dwarfs despite the stronger sensitivity of the Doppler detection method to these types of planets around low-mass stars. Around FGK-type stars, Marcy et al. (2005) cites a frequency of 1.2% for hot Jupiters.

While the limits that can be currently placed on the frequency of Jupiter-mass planets around M dwarfs are not entirely inconsistent with those of FGK-type stars, there does seem to be a trend to fewer high-mass planet detections around M dwarfs. If further results support this observation, it

would be consistent with the predictions of the core-accretion planet formation model. Laughlin et al. (2004) and Ida & Lin (2005) have shown that the formation probability of high-mass planets decreases with stellar mass for this model. Conversely, Boss (2006) suggests that giant planets might actually form more efficiently around M dwarfs if the gravitational instability mechanism is considered.

Further clouding the issue is the question of host star metallicity. As mentioned earlier, planets are more often detected around stars with high metallicities. In §3.2 I presented the results from a spectroscopic metallicity analysis of three M dwarfs that harbor extrasolar planets. The results indicate that all three have sub-solar metallicities which is a departure from the observed trend in the FGK-type stars that harbor extrasolar planets. In contrast, Bonfils et al. (2005a) presented metallicity measurements for these M dwarfs based on a lower precision photometric relationship. Our derived [M/H] values are lower by 0.09, 0.08, and 0.34 dex for GJ 876, GJ 581, and GJ 436 respectively than those determined by Bonfils et al. (2005a). In the case of the first two, the values are well within the overlapping errors for the two measurements (0.32 dex), while our measurement for GJ 436 is just outside this differential range.

Taken together, the results from our analysis and that of Bonfils et al. (2005a) do appear to rule out super-solar metallicities for these M dwarf planet hosts. The results for GJ 436 and GJ 581 are not surprising because current models do not predict a dependence of Neptune or lower mass planet

formation on metallicity. Future planet searches that will be sensitive to low-mass planets, including Earth analogs, should avoid a metallicity bias when selecting target samples to test this.

The result for GJ 876 on the other hand is curious because it hosts two high-mass planets. These kinds of planets should be rare around M dwarfs, but two were able to form around GJ 876 without even the benefit of high metallicity. One possible explanation is that GJ 876 had a more massive than normal protoplanetary disk than is typical for M dwarfs. However, there is a long history of odd discoveries in astronomy at first being explained away by very rare coincidences, but later turning out to be indicative of a misunderstanding about a particular process. The special GJ 876 system should not be dismissed as a fluke because it could be an opportunity to correct an error in the current planet formation paradigm.

This result also raises some other interesting questions. Are the metallicities for these stars representative of the metallicities of the M dwarfs on planet search programs and might that explain the lower detection rates of planets for the M dwarfs? If that were the case, are the solar neighborhood M dwarfs in general metal deficient relative to the other spectral type? Or, what is causing the selection effect to lower metallicity M dwarfs for the planet search programs? More observations and careful consideration of M dwarfs are needed in order to fully understand the effects of stellar mass on planet formation.

Table 3.1. Stellar Parameters for the M Dwarf Planet Hosts

Name	Spectral Type	T_{eff} (K)	log g (cgs)	[M/H]	ξ (km s^{-1})	η (km s^{-1})
GJ 876	M4	3478	4.89	-0.12	0.77	0.64
GJ 436	M2.5	3498	4.80	-0.32	1.02	0.00
GJ 581	M3	3480	4.92	-0.33	0.91	1.35

Note. — Adopted uncertainties are 48 K, 0.10 dex, 0.12 dex, 0.15 km s^{-1}, and 0.20 km s^{-1} for the derived parameters T$_{eff}$, log g, [M/H], ξ, and η respectively.

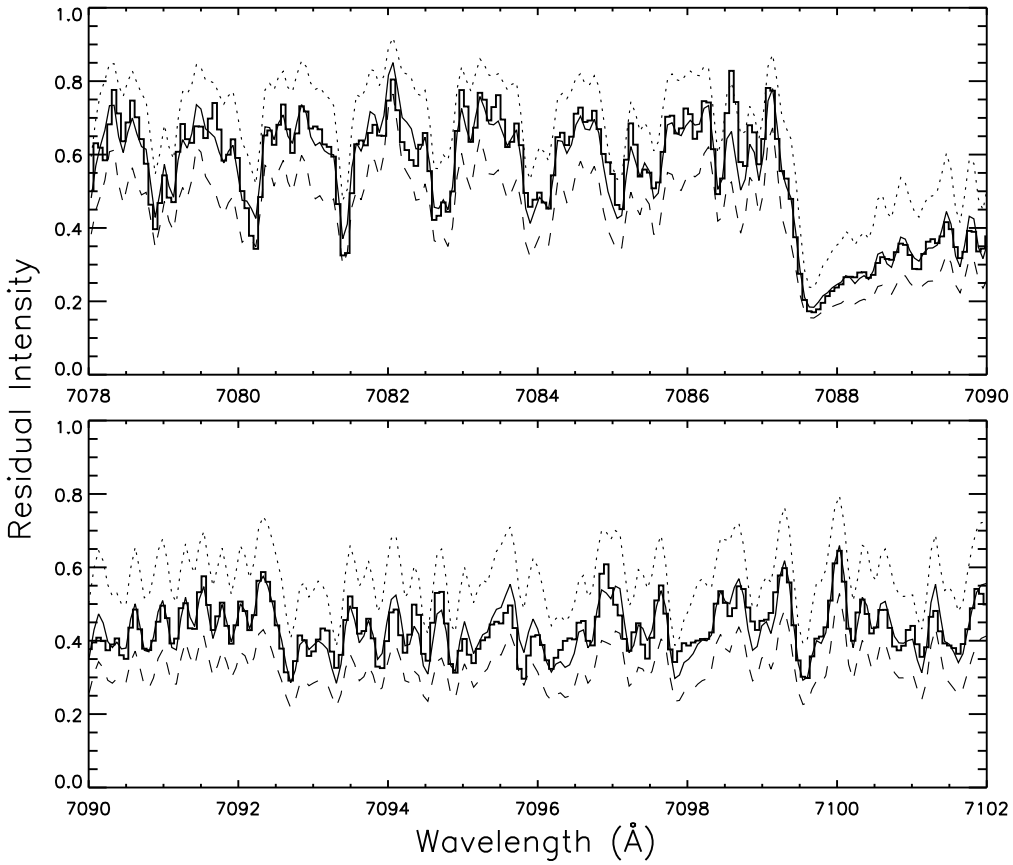

Figure 3.1 Spectral region near the strong TiO γ R_2 0 – 0 bandhead for GJ 876 (histogram). The best fit used to determine the stellar parameters is over-plotted (solid black line). For comparison, synthetic spectra computed with [M/H] values 0.3 dex lower (dotted line) and higher (dashed line) than the best fit value are also over-plotted.

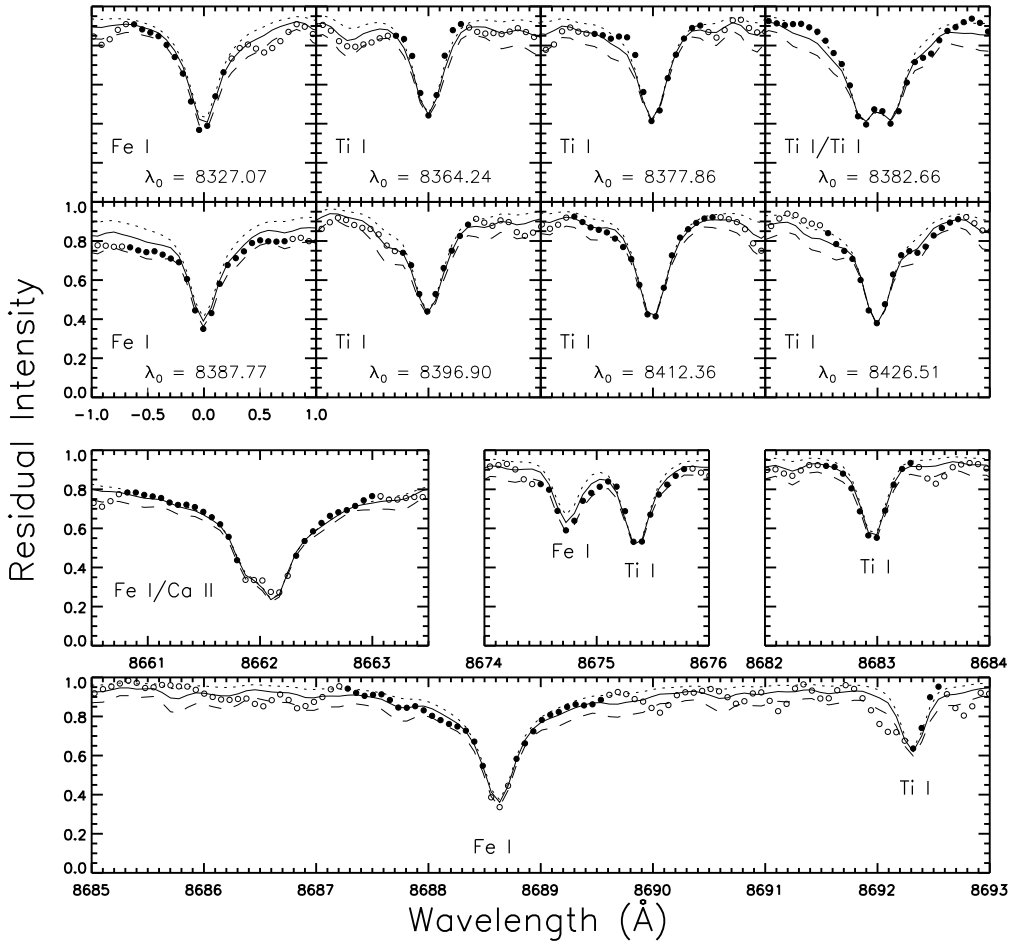

Figure 3.2 Fit of synthetic spectra (solid line) to atomic line profiles (circles) for GJ 876. The filled circles were used in the fitting process; the open circles were ignored. For comparison, synthetic spectra computed with [M/H] values 0.3 dex lower (dotted line) and higher (dashed line) than the best fit value are also over-plotted. The panels are sorted by wavelength and the linear scaling in both parameters is the same throughout. The lines in each half, top and bottom, make up a contiguous spectral order in our observed spectra. All apparent "lines" in the figure that aren't fit are actually multiple TiO lines.

Chapter 4

Metallicities of MLR M Dwarfs

Theoretical models of stellar structure and evolution are crucial tools for interpreting a wide variety of astronomical observations. The relevant application in the context of this dissertation is their use for estimating the masses of M dwarf planet hosts. In this Chapter I consider the inverse of this application of stellar models as a test of their accuracy. I evaluate how well the state-of-the-art theoretical models reproduce the absolute magnitudes of M dwarfs with measured masses and metallicities.

As discussed in Chapter 1, determining the masses of most exoplanets depends on assuming the masses of their host stars. This is because most exoplanet hosts are effectively single stars due to our current inability to directly image their planets. Therefore, the reliability of the models needed for estimating the masses of exoplanet host stars is an important foundation for the study of the exoplanets themselves. Because the reliability of theoretical models is only as good as the empirical data used to constrain them, the study of exoplanets would benefit from precise measurements of stellar physical parameters to challenge model predictions. This is especially true for models of M dwarfs, which are necessarily more complex than earlier type stars.

The variety and details of the available models for low-mass stars were recently discussed by Hillenbrand & White (2004). Currently, the most sophisticated models are those produced by the Lyon group and presented in Baraffe et al. (1998, hereafter B98). The most important aspect of the B98 models is that they use realistic model atmospheres, the NextGen models calculated with the PHOENIX computer code, as an outer boundary for the stellar interior and to calculate the emergent flux. Previous studies by the same group illustrated the necessity of this approach for low-mass stars. The technique used up to that point employed model atmospheres calculated assuming a wavelength-averaged absorption coefficient (i.e. "grey" model atmospheres, Chabrier & Baraffe 1997).

The need for realistic model atmospheres when calculating the structure and evolution of low-mass stars is due primarily to the effects of molecule formation. The formation of molecules in the cool atmospheres of these stars changes the adiabatic gradient, which leads to the extension of the convection zone into their photospheres and a departure from radiative equilibrium. Therefore, boundary conditions given by the deep layers of a grey model will be incorrect because they do not account for convective energy transport. Also, the breadth, strength, and wavelength dependence of molecular absorption (i.e. "line blanketing") causes significant flux redistribution in the resulting spectra compared to that given by grey models.

Masses for single stars are typically estimated by comparing the stars' observable properties, like luminosity, effective temperature, surface gravity,

and composition, to the the predictions of theoretical models. The same approach is not yet reliable for M dwarfs because of the difficulty of accurately determining those properties for them. Instead, M dwarf masses are typically estimated using one of the most basic relationships of stellar astrophysics, the Mass-Luminosity Relationship (MLR). However, as is true for earlier type stars, the concept of a MLR for M dwarfs is a simplification of the more complex dependence of luminosity on composition and age in addition to mass.

The predicted influence of metallicity on the M dwarf V and K band MLRs from the B98 models is illustrated in Figure 4.1. For M dwarfs with masses above 0.1 $M_{\odot}$ and ages more than 0.5 Gyr, higher metallicity should cause a significant reduction of their V band luminosity. However, the predicted effect of metallicity on their K band luminosity is minimal. B98 noted this and explained it as the result of two metallicity dependent processes in the atmospheres of M dwarfs.

The first metallicity dependent process is the formation of metal oxide and hydride molecules, which are the primary absorbers at visible wavelengths. The formation of these molecules is of course greater in atmospheres with higher metal abundances. Thus the opacity in the visible depends on the metallicity. An increase in the opacity at visible wavelengths causes increased absorption and heating of the atmosphere. The absorbed energy is released as redistributed flux to near-infrared wavelengths (J, H, and K bands). Thus, one effect of higher metallicity then is a diminishing of the V band luminosity, but an increase of the J, H, and especially K band luminosities.

The second metallicity dependent process in M dwarf atmospheres is the formation of the H^- ion, the dominant continuous opacity source in cool-star atmospheres. Metals are the main source of the free electrons needed to form H^-. Therefore, a higher metal abundance yields more H^- and continuous opacity, which reduces the luminosity at almost all bands.

The ultimate result predicted by the B98 models is that these two effects combine to significantly reduce the V band luminosities of M dwarfs with relatively high metallicities. On the other hand, the two effects compete at longer wavelengths and the K band luminosities are almost completely independent of metallicity.

The predicted effect of age on the the M dwarf MLR from the B98 models is also illustrated in Figure 4.1. For M dwarfs with masses above 0.1 $M_\odot$ and ages more than 0.5 Gyr, the effect of observable age variation on their luminosities should be minor. This is because M dwarfs evolve much slower than earlier type stars and have main sequence lifetimes up to and above 10^{12} years (Laughlin et al. 1997). Therefore, of the two additional parameters to consider for their effects on the intermediate mass M dwarf MLR, metallicity and age, metallicity is predicted to be the most important.

For the very lowest mass M dwarfs, those with masses less than 0.1 $M_\odot$, the effects of metallicity and age are more complex. These stars can take up to 4 Gyr just to evolve to the main sequence. Metallicity effects on the core temperature also become more pronounced. This influences the evolutionary speed and even whether or not the object initiates hydrogen fusion. As in-

teresting as the issues near the minimum stellar mass limit are, the dearth of objects with measured masses puts this regime outside the consideration of the current study. From this point on, I will discuss M dwarfs with masses $> 0.1 M_{\odot}$ and drop the qualifying term "intermediate mass" for conciseness.

Previous tests of the ability of the B98 models to reproduce the absolute magnitudes of the M dwarf stars with measured masses, which I hereafter refer to as the "MLR M dwarfs", were carried out by B98, Siess et al. (2000), Delfosse et al. (2000), Mazeh et al. (2001), Torres & Ribas (2002), and Torres et al. (2002). For illustration, a compilation of the published data for all the MLR M dwarfs with masses determined to better than 10% is plotted in Figures 4.2 (K band) and 4.3 (V band) along with the predictions of the B98 models. The data were taken from Henry & McCarthy (1993), Metcalfe et al. (1996), Martin et al. (1998), Henry (1999), Forveille et al. (1999), Torres et al. (1999), Benedict et al. (2000a), Ségransan et al. (2000), Benedict et al. (2001), Mazeh et al. (2001), Ségransan (2001), Torres & Ribas (2002), Torres et al. (2002), and Martinache et al. (2007). Note that the V band MLR is more populated because many of the objects do not have measured K band magnitudes.

One result that has emerged from the previous studies, and that can be seen in Figure 4.2, is that the B98 models reproduce the K band empirical MLR data very well. Also, the small amount of scatter in the empirical data beyond that expected from the measurement uncertainties supports the prediction of the minimal effect of metallicity and age on the K magnitudes of M

dwarfs.

The other important result that has emerged from the previous studies is that B98 models do not match the empirical V band MLR data. This is demonstrated in Figure 4.3. The models seem to over-predict the luminosities (under-predict the magnitudes) of M dwarfs. However, the increased scatter among the V band data relative to the K band is circumstantial evidence for the predicted effect of metallicity on their spectral energy distributions.

There have been no previous measurements of the metallicities for any of the MLR M dwarfs. This is primarily due to a lack of a reliable method to determine M dwarf metallicities. With our development of a such a needed technique, we were in a position to carry out such measurements for the first time.

Of course, all the MLR M dwarfs are in binary systems and the ones in double-lined spectroscopic systems (SB2) would not be amenable to easy chemical abundance study. In addition, some are known to be very fast rotators and the broadening of their spectral lines would limit the precision of a metallicity determination. Nevertheless, the importance of metallicity for testing low-mass stellar models led us to attempt to analyze as many of the MLR M dwarfs as possible. We were indeed able to measure the metallicities for a selection of systems that were effectively single-lined spectroscopic (SB1) or visual binaries. In these cases, their multiplicity was a benefit because the metallicity measured for one object in a system was applicable to two or more stars with precisely measured masses. Ultimately, the data obtained from our

analyses enabled us to quantify the error in the B98 V band model predictions for intermediate mass M dwarfs to a higher precision than was previously possible.

In §4.1 I describe our spectroscopic observations of the majority of the MLR M dwarfs systems. In §4.2 I discuss the culling of the data for the best selection of the observed systems to measure their metallicities. In §4.3 I give the results of our metallicity analysis for the selected stars. In §4.4 I compare the measured masses, metallicities, and V magnitudes with the predictions of the B98 models. I conclude the Chapter with a discussion of the results in §4.5.

4.1 Observations and Data Reduction

We observed many of the MLR M dwarf systems using the 2.7m telescope at McDonald Observatory during three observing runs. In addition to the already published systems described above, we also observed some M dwarf systems where precise mass determinations were in progress (T. Henry & G. F. Benedict, private communication). The list of observed systems is given in Table 4.1. One of the target systems, GJ 644, has a M dwarf visual companion, GJ 643. We therefore observed GJ 643 as a proxy for the GJ 644 system because it is a single star and would be easier to analyze.

The three McDonald observing runs were May 5 – 7, 2004, August 5 – 6, 2004, and January 24 – 25, 2005. The data during all the runs were obtained with the 2dcoudé spectrograph using the same setup described in

§2.1. Exposure times varied from 10 to 30 minutes. Multiple exposures were taken for all objects and co-added with cosmic ray removal before reduction and extraction. The maximum total exposure time was 120 minutes for the faintest targets.

CCD reduction and optimal order extraction were carried out using the REDUCE package (Piskunov & Valenti 2002). The wavelength calibrations for each object were calculated based on the identification of roughly 1000 lines in thorium-argon emission spectra taken at the beginning of each respective night and have RMS precisions of 0.002 Å. The final one-dimensional spectra all have S/N $>$ 100 pixel^{-1} in the spectral regions that were analyzed.

4.2 Culling the Sample

We analyzed the obtained spectra using two methods to discriminate which could be reliably analyzed using our metallicity measurement technique. The first was a simple visual inspection of the 8670 – 8695 Å spectral region, which is one of the regions we model in our metallicity determination. This region is relatively free of molecular haze and has some narrow atomic lines. We visually inspected these lines for strong broadening due to high rotational velocities. Also, we looked for duplicate sets of lines offset in wavelength, which would be indicative of the spectrum being a composite of the two unresolved objects in the system. Some examples of the spectra to illustrate the visual discrimination are shown in Figure 4.4.

The second method we used to determine which systems were amenable

to abundance measurement was a cross-correlation analysis. For the systems that passed the visual inspection test, we cross-correlated their spectra with synthetic spectra generated as for our metallicity determination technique and with the observed spectrum of GJ 623. The synthetic spectra were useful for analyzing the spectral regions used in our metallicity analysis and provided fully resolved line profiles and narrower correlation functions. The observed spectrum had the same spectral format and allowed cross-correlation for all the spectral orders. GJ 623 is a well established SB1 and has been used as a cross-correlation template for radial velocity determinations of M dwarfs previously (e.g. Benedict et al. 2001).

We analyzed the cross-correlation functions by fitting the data with a Gaussian function, which represented a single star model. We looked for deviations from the best fit due to multiple significant peaks or asymmetries in a single peak. Both of these morphologies would be due to the target spectrum being a composite. Some examples of the computed and fitted cross-correlation functions are shown to illustrate this analysis method in Figure 4.5. The final classifications of the observed systems are listed in Table 4.1.

4.3 Analysis and Results

We determined the metallicities for the observed MLR M dwarfs classified as SB1 using our spectrum synthesis method as described in Chapter 2, with one exception. We have used an updated version of MOOG that includes corrections of some code errors that were in the previous version. We have re-

analyzed the spectra presented in previous chapters using this new version and found results that were different at or below the 0.5σ level with no apparent systematic trend.

The determined stellar parameters for each system are given in Table 4.2. As for the analyses in Chapter 3, we adopt the uncertainties in the derived parameters that were estimated in Chapter 2. They are 48 K, 0.10 dex, 0.12 dex, 0.15 km s^{-1}, and 0.20 km s^{-1} for T_{eff}, log g, [M/H], ξ, and η respectively.

For all the systems except GJ 643 and GJ 747 AB, the parameters are for the primary in the system. GJ 643 is a single star so there is no ambiguity of which component the parameters apply to. For GJ 747 AB, the components are of nearly equal mass and magnitude (see Table 4.3). They most likely have very similar individual spectra and contribute equally to the observed spectrum. They also must have a low velocity difference at the orbital phase of the observations because the system was classified as a SB1 from the analysis discussed in §4.2. Therefore, the parameters derived for GJ 747 AB are likely a mean of the system and the determined metallicity is suitable for testing the B98 models.

Four of the primaries have published resolved K magnitudes in addition to the V magnitudes used for the model comparison in §4.4. This allows the estimation of their metallicities using the Bonfils et al. (2005a) photometric relationship. These metallicities are also given in Table 4.2. A comparison of the results from the two methods indicate that the values we determine are on

average 0.08 dex lower than those determined from the Bonfils et al. (2005a) relationship and none are outside the overlapping error ranges. This result is similar to that found in §3 for the M dwarf planet hosts. The close and consistent agreement between the two methods is support for the reasonableness of our results.

The slightly subsolar metallicities and also low variation among the objects studied here indicates a bias in the sample. We identify two factors that contribute to this. First, we only analyzed objects that were slow rotators. This preferentially selects for older stars that will typically have subsolar metallicities. Secondly, all the studied objects are in resolvable binaries. Therefore, they are all nearby and will not have exceptionally low metallicities. Further support of the metallicity homogeneity of the sample is the low scatter in the offset from model predictions that is calculated in §4.4.

4.4 Comparison with Model Predictions

The masses and absolute V magnitudes for the selected MLR M dwarfs taken from the literature are given in Table 4.3 along with the metallicities we determined for them. For two systems (GJ 623 AB and GJ 644 ABC), two different groups have measured the masses and magnitudes of the components. The listed values for these stars are the weighted mean of the two published results. Three other systems (GJ 469 AB, GJ 22 AC, and GJ 1081 AC) do not have published masses and magnitudes. The masses for these systems are from preliminary analyses of *Hubble Space Telescope* interferometric

and ground-based speckle astrometry and radial velocities (T. Henry & G. F. Benedict, private communication). Observations of these systems are still underway and the final results are pending. However, these preliminary results are reliable because, in each case, enough of the orbit has been observed to yield an accurate characterization of the uncertainty in the orbital parameters and, thus, the masses. The magnitudes for these systems are what their final published values from the ongoing project will be because the observations to measure them have already been completed and analyzed.

We compare the data for the MLR M dwarfs to the predictions of the B98 models in Figures 4.6, 4.7, and 4.8. To calculate the predicted M_V values from the B98 models we used a cubic convolution interpolation in the grid of model data for a given object mass, metallicity, and age. In Figures 4.6 and 4.7 we compare the M_V values for the components in each system with a 5 Gyr MLR interpolated from the B98 models for each system's metallicity.

In Figure 4.8 we show the difference in the B98 predicted and the measured M_V values for all the objects as a function of mass. The uncertainties in the deviations from the B98 models includes the uncertainties in the measured magnitudes, masses, and metallicities and also a consideration of the effects of age variations. To account for the uncertainties in the measured masses, the predicted M_V values were calculated for the mass value plus and minus the mass uncertainty. The average absolute deviation of these calculated M_V values from that calculated from the actual mass were assumed to represent the uncertainty in the model predictions due to the uncertainty in the measured

mass. The same was done to account for uncertainties the measured metallicities by incrementing these values plus and minus the uncertainty (0.12 dex) and also for the age using an adopted 4 Gyr variance. The component uncertainties were added in quadrature with the uncertainty in the measured M_V values to yield the uncertainty in the deviation from the model predictions.

The dominant contribution to the error budget for the deviations from the model predictions for most of the stars is the uncertainty in the metallicity measurements. The adopted 0.12 dex error in [M/H] corresponds to 0.14 – 0.22 mag uncertainty in the predicted M_V values. This further illustrates the sensitivity of the M dwarf V band luminosities to metallicity, and the importance of measuring this parameter for these stars to the highest precision possible.

The error contributions from the measured masses are typically 0.03 – 0.14 mag, which is similar to the errors in the measured magnitudes. The notable exception is for the GJ 1081 AC system, which has component mass errors of 12% and 13%. All the other systems have masses measured to better than 6%. The mass errors for GJ 1081 AC correspond to 0.33 and 0.46 mag uncertainties in the predicted M_V values. The least important factor is the adopted 4 Gyr age variance, which contributes ≤ 0.04 mag uncertainty.

The comparison of the empirical data with the B98 models clearly shows that the models over-predict the V band luminosities (under-predict the magnitudes) of the intermediate mass M dwarfs. The data in Figure 4.8 does not suggest that there is a mass dependence of the deviation over the range 0.15 –

0.42 $M_{\odot}$. Neglecting the star with a mass outside this range (GJ 623 B) and the GJ 1081 AC data, the weighted average residual is 0.75 ± 0.07 mag (σ = 0.25 mag).

4.5 Discussion

Our measurements of the metallicities for a sample of the MLR M dwarfs has yielded a confirmation of an error in the B98 models for intermediate mass M dwarfs. The inaccuracy of the predicted V magnitudes compared to the apparent accuracy of the predicted K magnitudes could be indicative of a shortcoming in the model atmospheres used for the stellar structure and evolution calculations. B98 had previously noted the inaccuracy of their predicted V magnitudes and attributed it to a missing opacity source in the visible. They claimed that an increase in the total V band opacity by a factor of five would lead to an increase in predicted V magnitudes of $\sim$ 0.5 mag without significantly affecting the longer wavelength bands or the atmosphere temperature profiles.

At the time of the B98 work, the available empirical data were not of sufficient quality to precisely quantify the error in the models. Since then, the number and quality of the mass measurements for M dwarfs has increased and our metallicity analysis of some of these stars has allowed us to quantify the error in the B98 models more precisely. We find that the models are deviant in predicted M_V values by 0.75 ± 0.07 mag, which is slightly larger than previously thought. Finding the "missing" V band opacity could potentially

rectify most or all of this problem.

Significant advances in the model atmospheres of low-mass have been made since the NextGen version of the PHOENIX models were calculated, including some discussed in Chapter 2 of this Dissertation. It is possible that stellar structure models calculated assuming the new atmospheres as a boundary condition would yield much better agreement with the empirical data. The test of the current models that we have presented here will hopefully motivate a new generation of models and serve as a benchmark for their continuing evolution.

Table 4.1. Observed MLR M Dwarf Systems

Name	Observation Date	Type[a]
GJ 473 AB	05/05/2004	FR
Cm Dra AB	05/05/2004	SB2
GJ 623 AB	05/06/2004	SB1
GJ 644[b]	05/06/2004	S
GJ 661 AB	05/06/2004	SB2
GJ 747 AB	05/07/2004	SB1
GJ 469 AB	05/07/2004	SB1
GJ 831 AB	08/05/2004	SB2
GJ 860 AB	08/05/2004	SB1
GJ 22 AC	08/05/2004	SB1
GJ 748 AB	08/06/2004	SB1
GJ 1081 AC	01/24/2005	SB1
YY Gen AB	01/24/2005	SB2, FR
Cu Cnc AC	01/24/2005	FR
GJ 234 AB	01/25/2005	FR

[a]The classification types are: FR - fast rotator, SB2 - double-lined spectroscopic binary, SB1 - single-lined spectroscopic binary, and S - single star.

[b]Visual companion to GJ 643 ABC and observed as a proxy for that system.

Table 4.2. Derived Stellar Parameters for the MLR M Dwarf Systems

Name	T_{eff}[a] (K)	log g[a] (cgs)	[M/H][a]	ξ[a] (km s^{-1})	η[a] (km s^{-1})	[M/H][b]
GJ 623 AB	3455.0	4.80	-0.41	0.97	0.94	-0.38
GJ 643	3491.7	4.90	-0.31	1.27	3.53	-0.24
GJ 860 AB	3424.7	4.95	-0.40	0.94	0.00	-0.20
GJ 1081 AC	3422.5	4.92	-0.39	0.92	1.25	···
GJ 469 AB	3443.1	4.88	-0.25	0.54	2.19	···
GJ 747 AB	3427.0	5.02	-0.36	0.95	0.71	-0.33
GJ 22 AC	3552.8	4.82	-0.38	0.78	0.62	···
GJ 748 AB	3406.9	4.85	-0.34	0.83	2.01	···

Note. — Adopted uncertainties are 48 K, 0.10 dex, 0.12 dex, 0.15 km s^{-1}, and 0.20 km s^{-1} for the derived parameters T_{eff}, log g, [M/H], ξ, and η respectively.

[a]Determined from the spectral synthesis analysis.

[b]The value determined using the Bonfils et al. (2005a) photometric relationship for the primary if deconvolved K magnitudes are available.

Table 4.3. Data for the MLR M Dwarfs

Name	M ($M_\odot$)	M_V	[M/H]	Ref.
GJ 623 A	0.365 ± 0.013	10.75 ± 0.03	-0.41	1,2
GJ 623 B	0.115 ± 0.002	16.03 ± 0.08	-0.41	1,2
GJ 469 A	0.352 ± 0.019	11.63 ± 0.12	-0.25	3
GJ 469 B	0.219 ± 0.014	13.22 ± 0.13	-0.25	3
GJ 22 A	0.417 ± 0.012	10.56 ± 0.07	-0.38	4
GJ 22 C	0.164 ± 0.005	13.64 ± 0.12	-0.38	4
GJ 748 A	0.379 ± 0.005	11.26 ± 0.03	-0.34	5
GJ 748 B	0.192 ± 0.003	13.09 ± 0.04	-0.34	5
GJ 644 A	0.416 ± 0.006	10.70 ± 0.02	-0.31[a]	6,7
GJ 644 B	0.346 ± 0.005	11.28 ± 0.05	-0.31[a]	6,7
GJ 644 C	0.313 ± 0.004	11.77 ± 0.05	-0.31[a]	6,7
GJ 860 A	0.271 ± 0.010	11.76 ± 0.05	-0.40	8
GJ 860 B	0.176 ± 0.007	13.46 ± 0.09	-0.40	8
GJ 1081 A	0.309 ± 0.037	12.42 ± 0.15	-0.39	3
GJ 1081 C	0.168 ± 0.022	14.09 ± 0.15	-0.39	3
GJ 747 A	0.214 ± 0.001	12.30 ± 0.06	-0.36	6
GJ 747 B	0.200 ± 0.001	12.52 ± 0.06	-0.36	6

References. — (1) Ségransan (2001), (2) Martinache et al. (2007), (3) T. Henry, private communication, (4) G. F. Benedict, private communication, (5) Benedict et al. (2001), (6) Ségransan et al. (2000), (7) Mazeh et al. (2001), (8) Henry (1999)

[a]Taken from the analysis of the visual companion GJ 643.

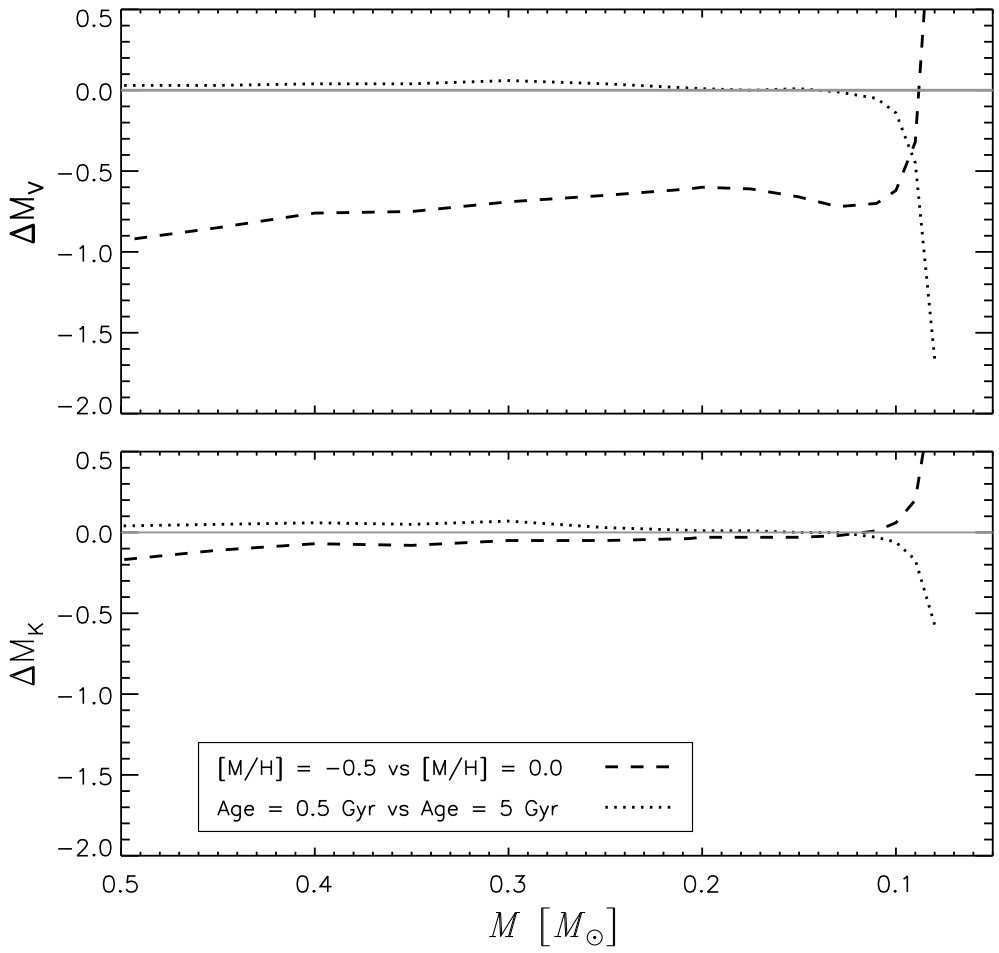

Figure 4.1 Predicted changes in the absolute magnitudes of M dwarfs due to variation of metallicity and age from the B98 models. The baseline isochrone is for [M/H] = 0.0 and Age = 5 Gyr. The dashed line represents the predicted difference between a model with the same age, but [M/H] = -0.5. The dotted line shows the difference between the baseline isochrone and one with the same metallicity, but Age = 0.5 Gyr.

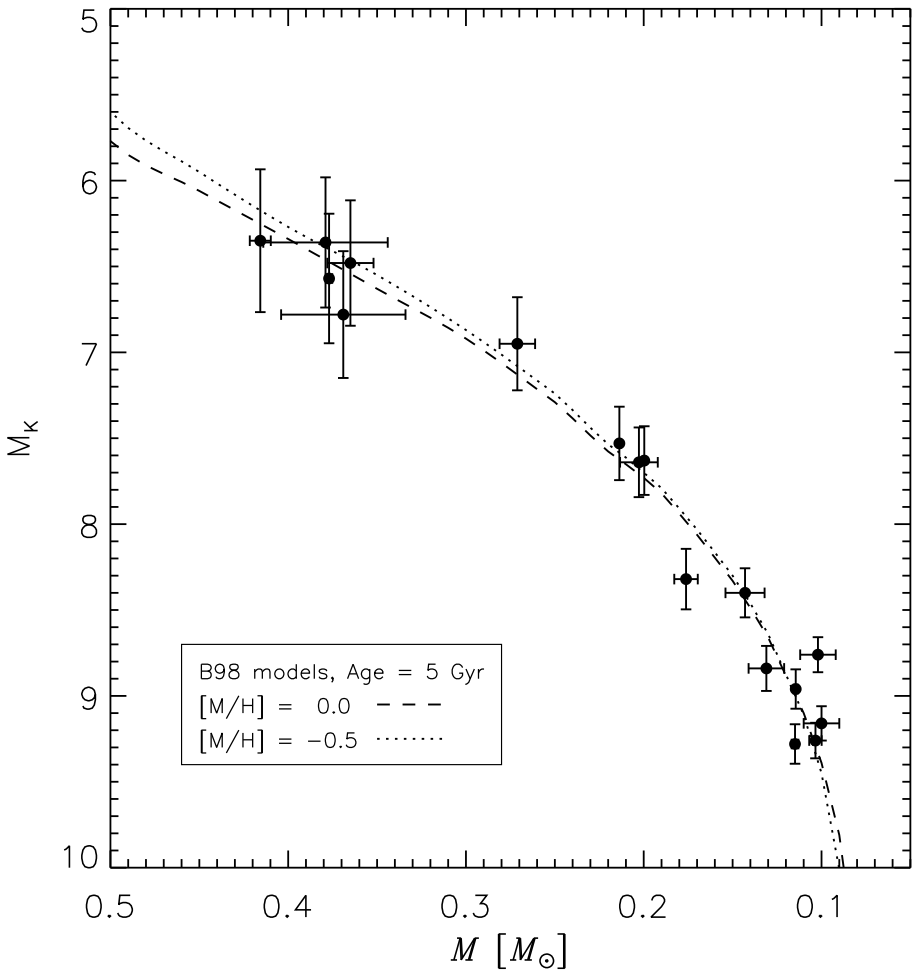

Figure 4.2 Absolute K magnitudes for the M dwarfs with masses measured to better than 10% (circles). The B98 5 Gyr isochrones for [M/H] = 0.0 (dashed line) and [M/H] = -0.5 (dotted line) are also shown.

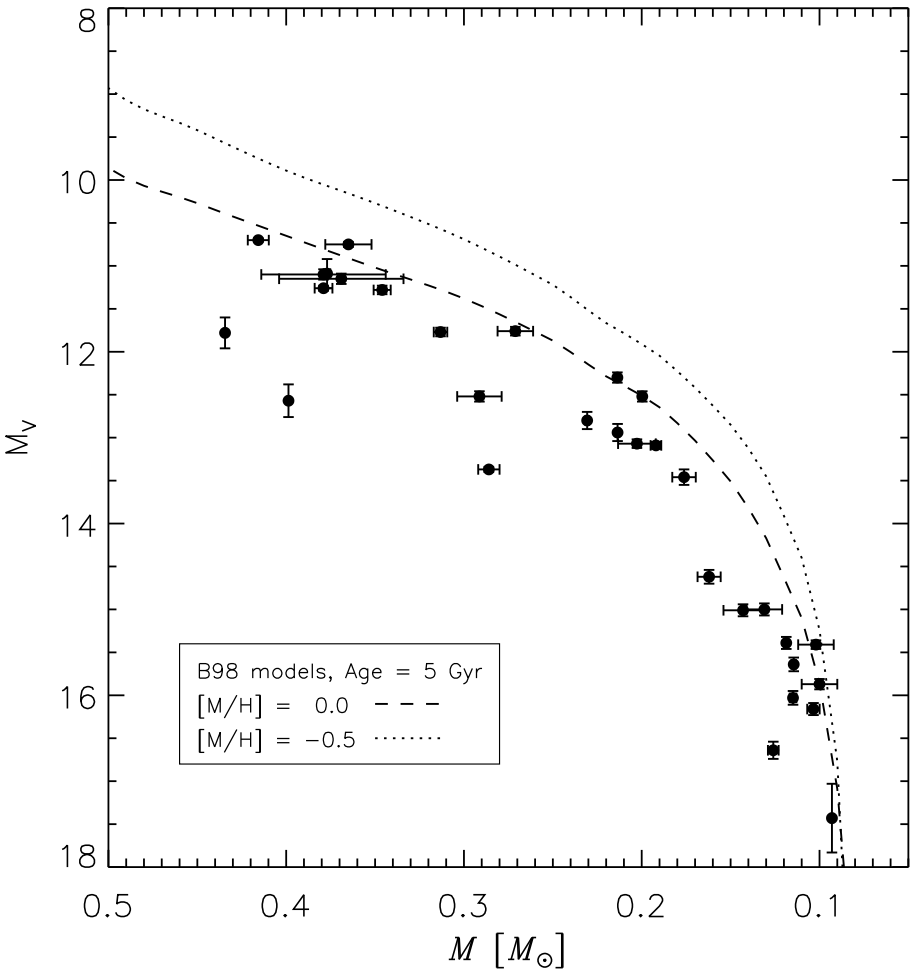

Figure 4.3 Same as Figure 4.2, except for absolute V magnitudes.

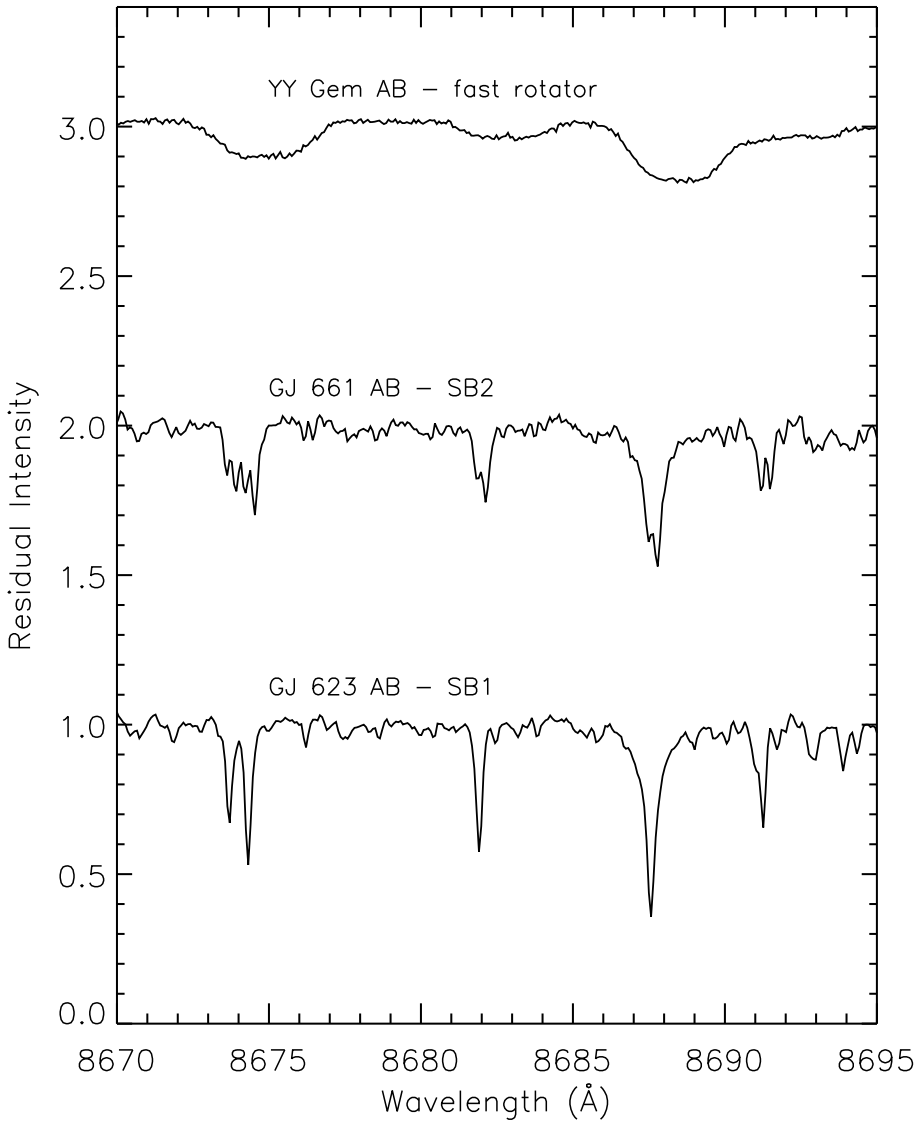

Figure 4.4 Spectra of example systems parsed by visual inspection. YY Gem AB (top) is a fast rotator with spectral lines too broadened for a precise chemical abundance analysis. The spectrum of GJ 661 AB (middle) shows two sets of spectral lines, which indicates the system is a SB2. GJ 623 AB (bottom) appears single by visual analysis of the spectrum.

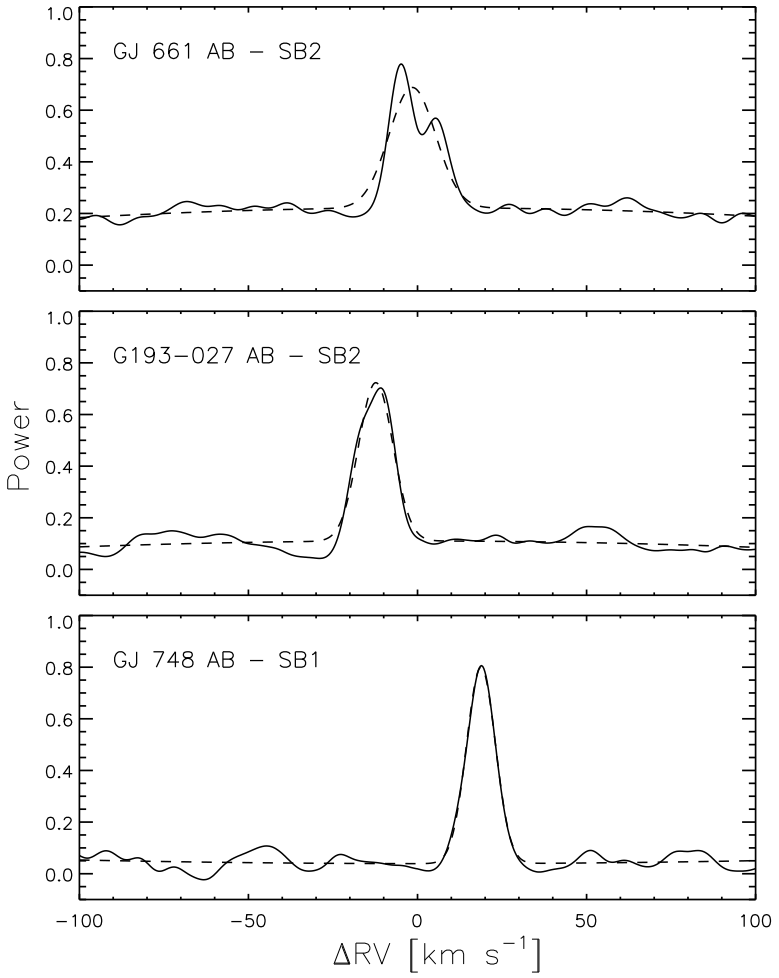

Figure 4.5 Cross-correlation functions of a single echelle order for the spectra of three example systems (solid line) with a single star model fit (dashed line). GJ 661 AB (top) was clearly double in the visual inspection and shows the expected double peaked cross-correlation morphology. G193-027 AB (middle) looked like a SB1 by visual inspection, but the asymmetry of the cross-correlation function indicates that its spectrum includes a significant contribution from both components. The cross-correlation function for GJ 748 AB (bottom) is well fitted by a single star model and is therefore classified as a SB1.

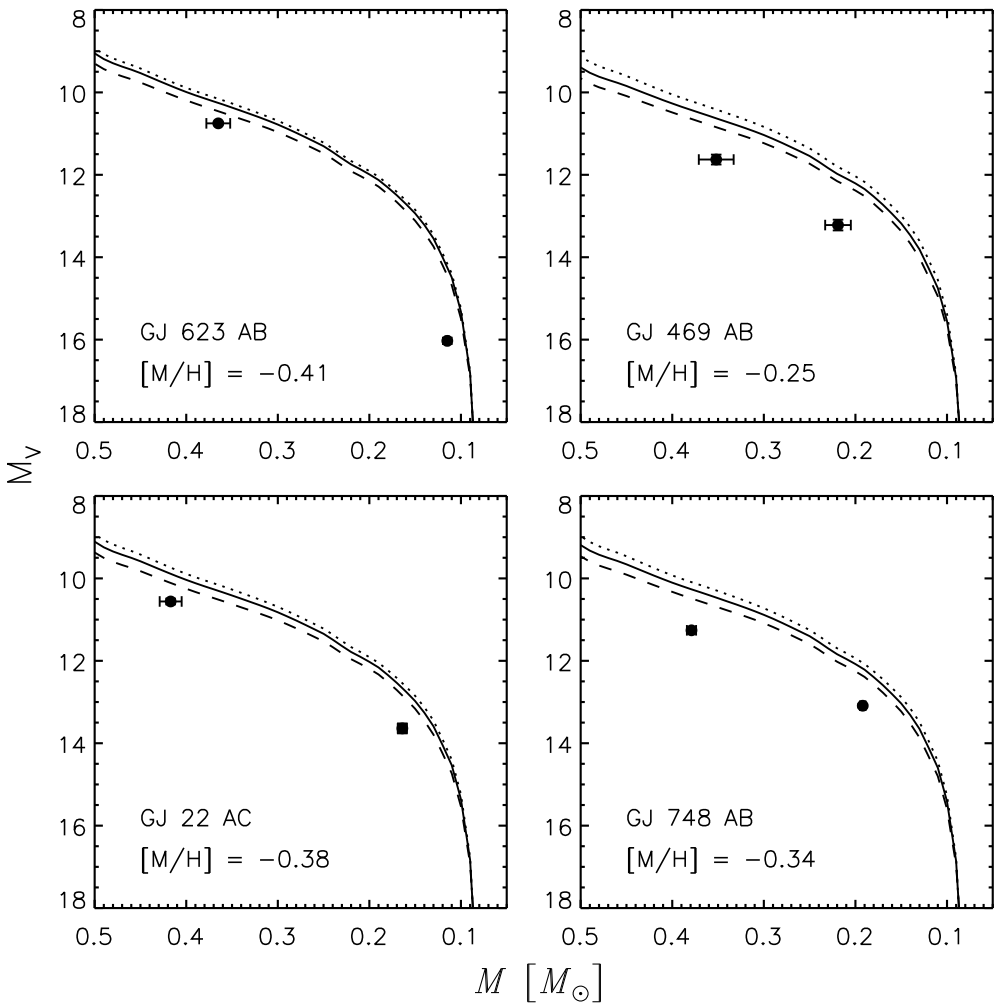

Figure 4.6 Absolute V magnitudes and masses for the MLR M dwarfs for which we measured metallicities (circles). The components of each system are plotted in the same panel because they are presumably coeval. An interpolated 5 Gyr isochrone from the B98 models with the metallicity of the system is shown (solid line). The dashed and dotted lines are the interpolated isochrones with metallicity equal to plus one sigma (dashed) and minus one sigma (dotted).

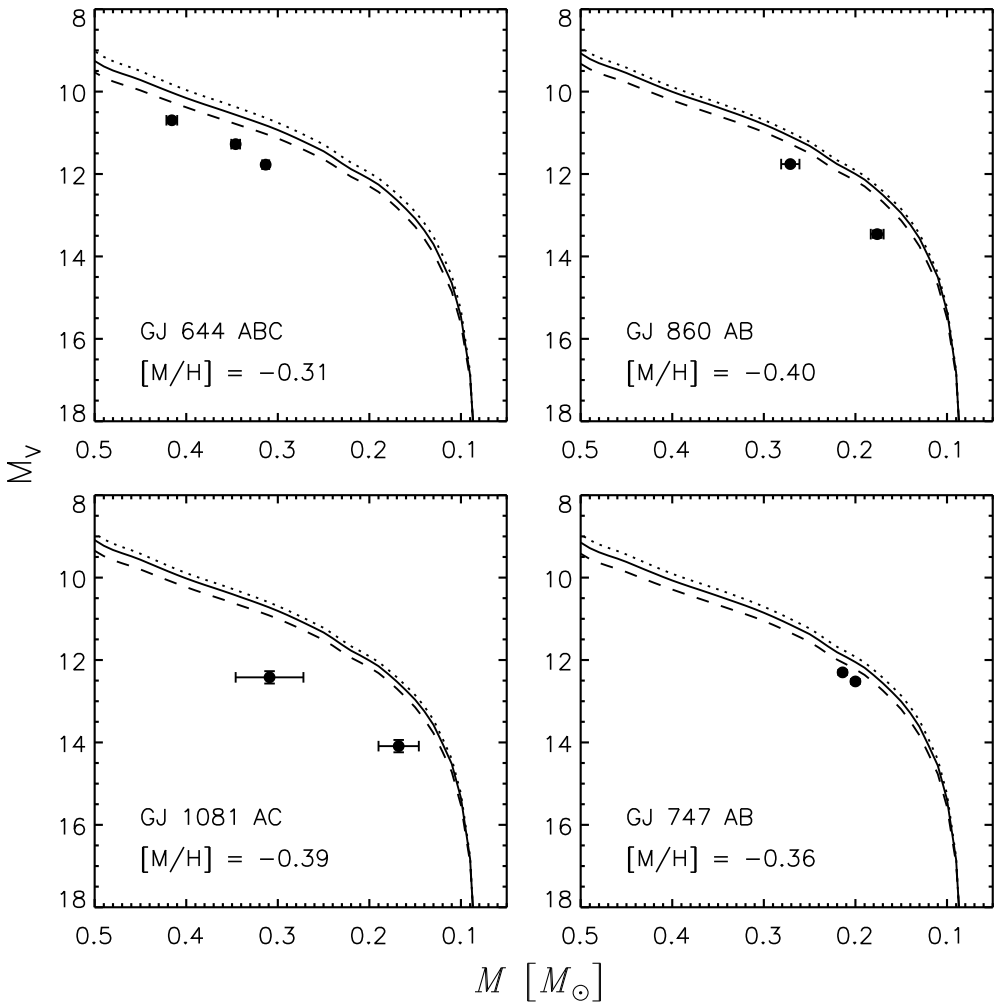

Figure 4.7 Same as Figure 4.6, except with four different systems.

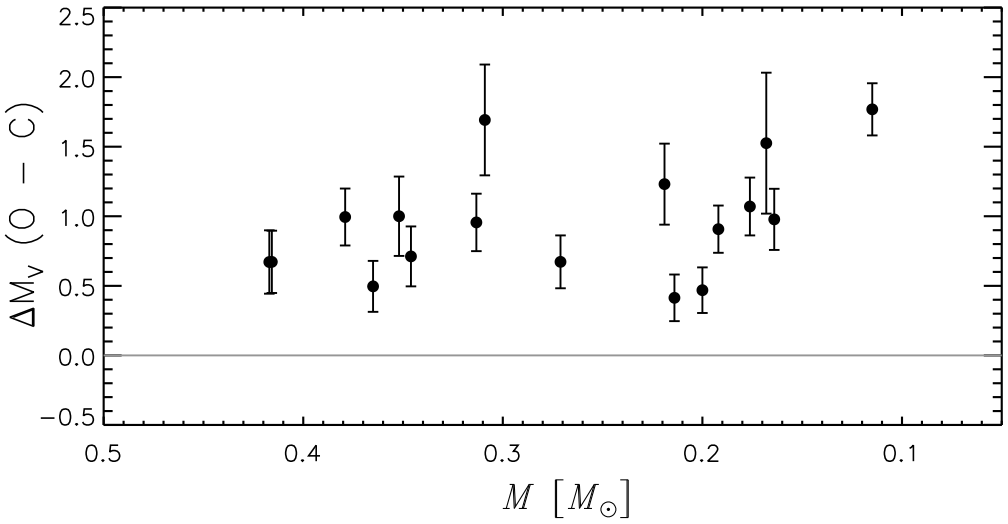

Figure 4.8 The difference between the 5 Gyr model predicted and measured magnitudes for the study stars (circles). The error bars include the uncertainties in the measured magnitudes, masses, and metallicities and a ± 4 Gyr age variance. For the range $0.42 \geq M \geq 0.16\ M_\odot$ and neglecting the two stars with mass errors > 10%, we find a weighted average deviation from the models of 0.75 ± 0.07 mag.

Chapter 5

The Mass of the Candidate Exoplanet Companion to HD 33636

Mass is the most important physical property of exoplanets because it is the one parameter that can establish a star's companion as an actual planet rather than a brown dwarf or low-mass star. Exoplanet masses also provide important constraints for theoretical models. As for stars, mass critically determines most of the instantaneous characteristics and long-term evolution of a planet. Therefore, we can test, and ultimately improve, our understanding of planet formation and evolution by comparing model predictions with the observed physical and orbital properties of exoplanets with measured masses.

Currently, fewer than 10% of the more than 200 candidate exoplanets[1] orbiting nearby stars have determined true masses. Only the minimum masses are known for the other 90%. This is because the most successful technique for detecting candidate exoplanets, the radial velocity method, cannot be used to remove the degeneracy between the mass and orbital inclination for most of the known exoplanet candidates. In principle, radial velocities alone can be used to determine the masses of exoplanets in multi-planet systems where two

[1] A regularly updated list of reported exoplanets can be found at `http://exoplanet.eu/`.

or more planets are experiencing significant mutual gravitational interactions on short timescales (e.g. Nauenberg 2002; Rivera et al. 2005). However, only one such system is known (GJ 876), results from different groups vary significantly, and the effects of non-coplanarity have yet to be considered. Thus, establishing precise masses, rather than arguing statistically, for the majority of exoplanet candidates requires observations with complementary techniques. The techniques that have been employed to break the mass – inclination degeneracy in radial velocity data are astrometry (e.g. Benedict et al. 2002a) and transit (e.g. Henry et al. 2000) observations. In this Chapter I report the determination of a dynamical mass for the exoplanet candidate companion to HD 33636 based on combined modeling of radial velocity and astrometric measurements of its perturbation orbit.

HD 33636 (= G 97-25, HIP 24205) is G0 V star at a distance of 28.7 pc (Perryman et al. 1997). Vogt et al. (2002) reported the discovery of a candidate planetary mass companion orbiting HD 33636 in a long period and eccentric orbit based on its radial velocity variations. Perrier et al. (2003), and later Butler et al. (2006a), refined the companions's orbit parameters based on additional velocity measurements. Butler et al. (2006a) found the spectroscopic orbit parameters period $P = 2128$ days, eccentricity $e = 0.48$, and velocity semiamplitude $K = 164$ m s^{-1}, which resulted in an estimated minimum mass $M \sin i = 9.3\ M_{Jup}$ for the companion.

Assuming the Butler et al. (2006a) orbit parameters, the corresponding minimum astrometric perturbation, $a_A \sin i$, of HD 33636 due to its low-mass

companion would be 1.0 mas. This suggested that the perturbation from even an edge-on system orientation ($i = 90°$) would be detectable using the *Hubble Space Telescope* (*HST*) Fine Guidance Sensors (FGS), and was the motivation for this work. Benedict et al. (2002a), McArthur et al. (2004), and Benedict et al. (2006) have previously used the *HST* FGS in combination with radial velocity measurements obtained with ground-based telescopes to directly determine the masses of three exoplanets. Our observations and analysis to determine the mass of HD 33636's companion are similar and described in the following sections.

In §5.1 I describe radial velocity measurements of HD 33636 with the Hobby-Eberly Telescope (HET), which we have used to supplement the previously published velocity data for this object and search for additional low-mass, short-period companions. In §5.2 I describe *HST* observations and astrometric measurements. The reference star spectroscopy, photometry, resulting spectrophotometric parallaxes, and estimated proper motions are discussed in §5.3. In §5.4 I present our simultaneous modeling of the radial velocity and astrometry data. From this modeling we determine the perturbation orbit parameters, which allow us to calculate the mass of the companion to HD 33636. In §5.5 I show our analysis of the radial velocity residuals from the single companion model and present a calculation of our detection limits for additional companions. I discuss the implications of this result in §5.6.

5.1 Radial Velocity Data

The ultimate precision and accuracy of our measurement of the mass for HD 33636's unseen companion depends strongly on the quality and quantity of the radial velocity data used. Unaccounted for, but detectable, additional companions or poorly constrained spectroscopic orbit parameters for the known companion would each cause a systematic error in our result. We therefore carried out high-cadence spectroscopic observations for radial velocity measurements of HD 33636 with the HET. We used these data to supplement the previously published velocities for this object and the combined data set of radial velocities spans just over nine years.

5.1.1 HET Spectroscopic Observations

We observed HD 33636 on 65 nights using the HET to feed the High Resolution Spectrograph (HRS, Tull 1998) between UT dates September 20, 2005 and January 21, 2007. The HET is queue, rather than classically, scheduled, and the nights were randomly distributed throughout the observing seasons that the star was available. The HRS was used in the resolution R = 60,000 mode with a 316 gr mm^{-1} echelle grating. The cross-dispersion grating was positioned so that the central wavelength of the order that fell in the break between the two CCD chips was 5936 Å. A temperature controlled ($T = 70\overset{\circ}{.}0 \pm 0\overset{\circ}{.}1$ C) iodine cell (HRS3) was inserted in front of the spectrograph slit entrance for all exposures to imprint lines that provided a contemporaneous wavelength scale and instrumental profile (IP) fiducial. Three separate

exposures were taken within 15 minutes on all but a few nights. In total, 195 "target" observations of HD 33636 were made, including 64 sets of three observations each and three additional solitary exposures. Exposure times were nominally 120 s, but varied up to twice that occasionally to account for increased seeing and/or cloud cover.

Additionally, we observed HD 33636 once on December 6, 2006 without the iodine cell and with the same instrument setup, but in the R = 120,000 mode. The exposure time for that observation was 600 s. We used the spectrum from this "template" observation as the model template in the radial velocity analysis of the target spectra described in §5.1.2.

CCD reduction and optimal order extraction were carried out for all the individual spectra using the REDUCE package (Piskunov & Valenti 2002). The final median signal-to-noise (S/N) per pixel of the target spectra is 89 and the template spectrum S/N per pixel is 188. For the CCD binning we used (two pixels in the cross-dispersion direction and one in the echelle dispersion direction), there are roughly four pixels per resolution element in the R = 60,000 mode spectra and two in the R = 120,000 spectrum.

5.1.2 Radial Velocity Analysis

We used an independent adaptation of the canonical spectrum modeling technique described by Valenti et al. (1995) and Butler et al. (1996) to measure relative radial velocities in the extracted target spectra. The observed spectra between 5020 and 5860 Å were broken up into 637 separate 100 pixel

"chunks." Each chunk was modeled as the product of a high-resolution FTS spectrum of the iodine cell[2] and a template stellar spectrum convolved with an IP. The template spectrum was Doppler shifted before being multiplied by the iodine spectrum, and this constituted the measurement of the star's relative radial velocity. Additionally, the wavelength scale of the observations was simultaneously modeled as a second order polynomial. The reduced observed spectra have an arbitrary normalization and the model normalization was a free parameter as well.

We used the sum of 11 Gaussians, one central and five satellites on each side, to represent the HRS IP. The variable parameters were the width, σ, of the central Gaussian and the heights of the satellites. The height of the central Gaussian was calculated from the σ with the standard formula ($h = 1/2\pi\sigma$). The IP of the HRS varies considerably in shape and size along each echelle order. Therefore, we used a dynamic spacing of the satellites from the center of the central Gaussian. The spacing was set so that there were four satellites per the FHWM of the central Gaussian ($\Gamma \simeq 2.355\sigma$). The σ of the satellites were also set dynamically. They were equal to the σ of the central Gaussian multiplied by 0.35. Including the Doppler shift, three parameter wavelength scale, 11 parameter IP description, and spectrum normalization there was a total of 16 free parameters in the model for each spectrum chunk.

We based our model template spectrum on the R = 120k HD 33636

[2]The FTS spectrum of the HRS3 iodine cell is available at `ftp://nsokp.nso.edu/FTS\_cdrom/FTS50/001023R0.004`.

spectrum taken without the iodine cell. We modeled a flat field spectrum with the iodine cell that was obtained using the same instrument setup as the template observation, taken immediately after it in the same manner as for the velocity measurements, but without the Doppler shift parameter (15 free parameters). This yielded an accurate wavelength scale and IP description as a function of the spectral position on the CCD at that time. We used this information to estimate the intrinsic spectrum of HD 33636 by removing the IP from the template observation. We used a modified Jansson technique (Gilliland et al. 1992) for the deconvolution. This estimate of the HD 33636 intrinsic spectrum was used as the model template for the velocity measurement of the target spectra.

The spectral modeling yielded a velocity measurement for each of the 637 chunks in a spectrum. For each target spectrum, we calculated the weighted mean of the velocities from the chunks in a spectrum to give a single measured velocity and uncertainty. We weighted the velocities for each chunk according to the velocity error computed according to the formula for the intrinsic Doppler error in a section of stellar spectrum given by Butler et al. (1996). The median uncertainty in our 195 measured weighted mean velocities is 2.1 m s^{-1}. We converted the velocity determined from each spectrum into a relative radial velocity by correcting each measurement for the barycentric motion of the observatory in the line-of-sight direction using the JPL ephemeris DE405[3].

[3]The JPL ephemeris data may be obtained at `ftp://ssd.jpl.nasa.gov/pub/eph/`

The RMS deviation of the HET velocities from the perturbation orbit we determine (see §5.4) is 6.1 m s^{-1}. Using the method of Wright (2005), Butler et al. (2006a) estimated the intrinsic radial velocity "jitter" due to variations of the stellar photosphere for HD 33636 to be 5.2 m s^{-1}. Adding this value in quadrature to our velocity uncertainties we find $\chi^2_\nu = 1.1$ for the fit to the orbit, which indicates general agreement between our radial velocity measurement and error estimation technique and that of the California – Carnegie Planet Search group.

Our scheme of taking three successive exposures over the course of $\sim$ 10 minutes during most nights gives us the opportunity to somewhat reduce the impact of short-term stellar noise and random errors on our orbit analysis. In addition to calculating a simple weighted mean, we also used the program *Gaussfit* (Jefferys et al. 1988) to calculate a robust weighted midpoint time, velocity, and uncertainty for each of the 64 three observation sets. Comparing the resulting data to the fit for the weighted and robust mean methods, we find RMSs of 4.4 and 3.3 m s^{-1} respectively. Because of the higher quality of the robust combined velocities, we ultimately adopted those data in the analysis presented in §5.4. The velocity values, velocity uncertainties, and the corresponding heliocentric Julian dates are given in Table 5.1. The velocities we measured are relative to an arbitrary zero-point, and we have subtracted a constant value determined during our orbit analysis. Therefore, the velocities given are relative to the HD 33636 system barycenter under the assumption

`export/DE405/`

that our single-companion model for the system is correct.

5.1.3 Total Radial Velocity Data Set

In addition to our own measurements from the HET, we included published high precision radial velocity measurements of HD 33636 from Perrier et al. (2003, "Elodie" sample) and Butler et al. (2006a, "Lick" and "Keck" samples). G. Marcy (private communication) provided us with an updated version of the Keck velocities published in Butler et al. (2006a). These updated velocities result from a reanalysis of old spectra with an improved version of the California – Carnegie Planet Search Doppler analysis software and include an additional epoch of data taken since publication that overlaps with our HET observations. Table 5.2 lists the source, time coverage, number of data points, and RMS deviation from the final orbit fit for the individual samples.

The complete data set contains radial velocities from four different telescope and instrument combinations and has a time baseline of 3289 days (9.01 years). The preexisting data were a crucial component of our analysis, because HD 33636's companion has an orbital period more than four times the time span of our HET observations. However, the use of a heterogeneous data set does require particular care, because the velocities in each sample are relative to a different zero point. We found in the course of our analysis (see §5.4) that a simple offset parameter for each sample was sufficient to correct the velocities to the same zero-point.

5.2 *HST* Astrometry Data

We used the *HST* Fine Guidance Sensor 1r (FGS1r) to carry out astrometric observations of HD 33636 and five reference stars between UT dates August 20, 2005 and October 26, 2006. A detailed overview of the FGS1r as a science instrument was given by Nelan et al. (2003). Our data acquisition and reduction follow the procedure outlined by Benedict et al. (2000b) as for the FGS3. We used the FGS1r for the current study because it provides superior fringes from which to obtain stellar positions (McArthur et al. 2002).

Table 5.3 lists the log of the *HST* observations. The data span 432 days (1.18 years) and include 18 epochs. Each epoch contains 2 – 4 positional measurements of HD 33636 and the references stars, which were acquired contiguously over a time span of 26 – 35 minutes. The observation time listed is for the midpoint of each epoch. The field was observed at multiple spacecraft roll values, and HD 33636 had to be placed in different non-central locations within the field of view (FOV) to accommodate the distribution of reference stars. The F5ND neutral density filter was used for the observations of HD 33636, while the F583W filter was used for the reference stars due to their being much fainter. To account for using a different filter for the reference stars, we included a cross-filter correction term (Benedict et al. 2002b) in the astrometry model (see §5.4) for HD 33636.

5.3 Astrometric Reference Star Data

Because of the high sensitivity of the FGS as an astrometer, and despite the relatively large distance of the astrometric reference stars, we had to take into account their parallaxes and proper motions in our model (see §5.4). To establish these, we determined spectrophotometric parallaxes, and adopted proper motions that could be input as constraints to our model. Additionally, our model requires input $(B - V)$ colors for all the stars to correct for chromatic aberration (lateral color). Our method for estimating reference star spectrophotometric parallaxes is discussed extensively in Benedict et al. (2007) and we followed the same approach in the present study.

We obtained classification spectra of our astrometric reference stars with the R-C Spectrograph on the Cerro Tololo Inter-American Observatory (CTIO) Blanco 4 m telescope[4]. The spectral types were determined from these spectra by a combination of template matching and line ratios and are generally better than ± 2 subclasses.

We also obtained BVI photometry for the reference stars using the New Mexico State University 1m telescope and adopted JHK magnitudes from the Two Micron All-Sky Survey (2MASS) Point Source Catalog (Cutri et al. 2003). We estimated the stars' luminosity classes with this photometry and the reduced proper motion method. We estimated V band extinctions, A_V,

[4]CTIO is operated by the Association of Universities for Research in Astronomy Inc. (AURA), under a cooperative agreement with the National Science Foundation (NSF) as part of the National Optical Astronomy Observatories (NOAO).

for the reference stars by comparing their measured colors with the expected colors for their spectral type taken from Cox (2000).

We next estimated M_V values for the reference stars by assuming the prototypical values for their spectral types and luminosity classes given by Cox (2000). We calculated their spectrophotometric parallaxes from their measured V and the estimated A_V and M_V values. The determined spectral types and luminosity classes, measured V and $(B - V)$ values, estimated A_V values, assumed M_V values, and estimated spectrophotometric parallaxes for the reference stars are given in Table 5.4. Proper motions for these stars were taken from the 2nd data release of the USNO CCD Astrograph Catalog (UCAC2, Zacharias et al. 2004). These proper motions, along with the spectrophotometric parallaxes and measured $(B - V)$ values, enter our model as observations with error.

5.4 Simultaneous Radial Velocity and Astrometry Solution

We modeled the radial velocity and astrometry data simultaneously to determine the parallax, proper motion, and complete set of perturbation orbit parameters for HD 33636. With these determined parameters, we then calculated the mass of its companion. The method we used is very similar to that previously employed by Benedict et al. (2002a), McArthur et al. (2004), and Benedict et al. (2006) to determine the same parameters for other exoplanet host stars and their companions.

The astrometric model for HD 33636 that we used is represented by four solved equations of condition. They are

$$x' = x + LC_x(B-V) - XF_x, \tag{5.1}$$

$$y' = y + LC_y(B-V) - XF_y, \tag{5.2}$$

$$\xi = Ax' + By' + C - P_\alpha\pi - \mu_\alpha\Delta t - ORBIT_\alpha, \tag{5.3}$$

$$\eta = -Bx' + Ay' + F - P_\delta\pi - \mu_\delta\Delta t - ORBIT_\delta. \tag{5.4}$$

Identifying terms, x and y are the measured coordinates; $(B-V)$ is the photometric color; LC_x and LC_y are the lateral color corrections; XF_x and XF_y are the cross-filter corrections; A and B are plate scale and rotation parameters; C and F are offsets; μ_α and μ_δ are proper motion components, Δt is the time difference from the mean epoch; P_α and P_δ are parallax factor components; π is the parallax; $ORBIT_\alpha$ and $ORBIT_\delta$ are the astrometric components of the perturbation orbit; and ξ and η are the standard coordinates. The astrometric orbit is a function of the orbital parameters period (P), time of periastron passage (T_P), eccentricity (e), semimajor axis (a_A), position angle of the ascending node (Ω), inclination (i), and the longitude of periastron passage (ω).

We also modeled the astrometry for the five reference stars in parallel with HD 33636. The equations of condition for those stars are the same as given in Equations (1 – 4) minus the cross-filter corrections and perturbation orbit motion. The plate scale and rotation parameters and the offsets are the

same for HD 33636 and the reference stars at each epoch. The parallax and proper motion are unique for each star.

The radial velocity model for HD 33636 is given by a fifth solved equation of condition,

$$\gamma = RV + G_S - ORBIT_R, \tag{5.5}$$

where RV is the measured relative radial velocity; G_S is the velocity offset for each of the four velocity samples described in §5.1.3; $ORBIT_R$ is the radial component of the orbital velocity; and γ is the adopted velocity of the HD 33636 system barycenter. The exact choice of γ is arbitrary and immaterial because our analysis is based on the relative motion of HD 33636. The important point is that its value is the same for each radial velocity sample and the G_S values are used to correct the sample velocities to the same frame of reference. The radial velocity orbit depends on the parameters P, T_P, e, and ω, which are the same for the astrometric and radial velocity orbit models. The radial velocity orbit is also dependent on the velocity semiamplitude (K_A), which does not influence the astrometric orbit.

In addition to the shared orbit parameters, we enforced a relationship between the astrometric and radial velocity models using a constraint from Pourbaix & Jorissen (2000),

$$\frac{a_A \sin i}{\pi_{abs}} = \frac{P K_A \sqrt{1-e^2}}{2\pi(4.7405)}, \tag{5.6}$$

where astrometric only quantities are on the left. Quantities determined primarily or only by the radial velocities are on the right.

We solved for HD 33636's cross filter correction, coordinates, parallax, proper motion, and perturbation orbit parameters, the reference stars' coordinates, parallaxes and proper motions, the plate parameters for each astrometry epoch, lateral color corrections, and the velocity sample offsets by fitting the above models to the radial velocity and astrometry data. The HD 33636 cross-filter correction, lateral color corrections, and the reference star spectrophotometric parallaxes and proper motions were input into the model as observations with error. We used the *Gaussfit* program with robust estimation and the "fair" metric to determine the parameter values that gave the lowest χ^2 between our model and the measured data. We adopted the uncertainties returned by *Gaussfit*, which were generated from a maximum likelihood estimation that is an approximation to a Bayesian maximum a posteriori estimator with a flat prior (Jefferys 1990).

The radial velocity data, our best fit, and the fit residuals as a function of time are plotted in Figure 5.1. The radial velocities for each sample in the Figure have been corrected to the system barycenter using the corresponding offset values determined in the analysis. The RMS deviations for the individual samples are given in Table 5.2. We find RMS residuals for the Keck and HET velocities of 4.2 and 3.3 m s^{-1} respectively.

The right ascension and declination component astrometry data as a function of time with the plate scale variation, parallactic motion, and proper motion removed are shown in Figure 5.2. These data illustrate the astrometric orbital motion of HD 33636. The fit to the data is indicated and the RMS

residuals from our fit for HD 33636 are 1.4 mas and 1.0 mas in the right ascension and declination directions respectively. These values are consistent with the previously characterized FGS1r observation precision of $\sim$ 1 mas and the median residual RMSs for the 5 reference stars, which is 1.3 mas. The quality of the simultaneous orbit fit to the astrometry and radial velocity data is evidence of the clear detection of HD 33636's perturbation due to the known companion. The same data from Figure 5.2 are also shown as in the flat plane of the sky in Figure 5.3. The direction of orbital motion and the location and time of the next periastron passage (2010.65) are also indicated in Figure 5.3.

Relative coordinates and our determined absolute parallaxes and proper motions for HD 33636 and the five reference stars are given in Table 5.5. A summary of the *HST* astrometry for HD 33636 is given in Table 5.6. For HD 33636 we find π_{abs} = 35.6 $\pm$ 0.2 mas, μ_α = 169.0 $\pm$ 0.3 mas, and μ_δ = -142.3 $\pm$ 0.3 mas. Our parallax value is in excellent agreement with, but more precise than, the *Hipparcos* value π_{abs} = 34.9 $\pm$ 1.3 mas (Perryman et al. 1997). However, our determined proper motion is significantly different than the *Hipparcos* values μ_α = 180.8 $\pm$ 1.1 mas and μ_δ = -137.3 $\pm$ 0.8 mas (Perryman et al. 1997). The reason for this is that the *Hipparcos* model did not account for the large perturbation orbit of HD 33636. As discussed by Black & Scargle (1982), the proper motion parameters can absorb orbital motion in astrometry data. The *Hipparcos* satellite only made 16 measurements of HD 33636's position with a reported precision of better than 5 mas over a period of 2.1 years. The orbital motion of HD 33636 during this time led to the

underestimation of southerly proper motion component and overestimation of the westerly proper motion component. The *Hipparcos* measurements were not precise enough and did not span a sufficient amount of time to distinguish between proper motion and orbit curvature at the level necessary to trigger a multiplicity flag in the standard analysis (ESA 1997).

In the case of our analysis, we have the benefit of foreknowledge about the existence of a companion due to the radial velocity variations. The radial velocity data that we modeled simultaneously with the astrometry data is very sensitive to most of the orbit parameters and carries the most weight in the determination of those parameters because of its quantity and quality. Additionally, we have five times the per observation astrometric precision and four times the number of observations than *Hipparcos* for HD 33636. The *Hipparcos* data are not useful to include in our analysis because that would necessitate the inclusion of additional transformation terms similar to the velocity offsets used to combine the radial velocity datasets. This would result in further degradation of the *Hipparcos* precisions because there is no astrometric plate overlap between our *HST* observations and those of *Hipparcos*. Because of this, it would not have been useful to include the *Hipparcos* measurements in our analysis.

Our derived values and uncertainties for the perturbation orbit parameters are given in Table 5.7. Figure 5.4 shows a plot of the relationship between a_A and i for fixed P, K_A, e, and π_{abs} through the Pourbaix & Jorissen (2000) relationship (eq. [6]). We find that the orbit is nearly face-on, with

$i = 4.^{\circ}1 \pm 0.^{\circ}1$ from the plane of the sky. Correspondingly, we find a large perturbation size, $a_A = 14.2 \pm 0.2$ mas, relative to the previously calculated minimum perturbation $a_A \sin i = 1.0$ mas. We also find $P = 2117.3 \pm 0.8$ days. Assuming the mass of HD 33636 $M_A = 1.02 \pm 0.03 M_{\odot}$ (Takeda et al. 2007), we find the mass of the companion, M_B, by iterating the equation

$$\left(\frac{a_A}{\pi_{abs}}\right)^3 = M_B^3 \left(\frac{P}{M_A + M_B}\right)^2. \tag{5.7}$$

This yields $M_B = 142^{+3.3}_{-1.8}\ M_{Jup} = 0.136^{+0.003}_{-0.002}\ M_{\odot}$, which is relatively large compared to the minimum mass $M \sin i = 9.3 M_{Jup}$, calculated from the spectroscopic orbit parameters. We have elected to round up to the next significant figure in solar units to account for possible systematic errors in the adopted mass of HD 33636 and other aspects of the analysis. Our final adopted companion mass uncertainty, which is also given in Table 5.7, is $0.01 M_{\odot} = 11 M_{Jup}$. We conclude from this result that HD 33636's companion is a low-mass star and not an exoplanet.

5.5 Limits On Additional Companions

As discussed in §5.1, one motivation for obtaining additional radial velocity data beyond the previously published data was to search for, and place limits on, additional companions in the system. To do this we analyzed the radial velocity residuals from the orbit model described in §5.4. We calculated a (Lomb) periodogram (Press et al. 1992) for the residuals from the model fit and the result is shown in Figure 5.5. We searched for prominent peaks

at periods shorter than the time span of the data set (3289 days) and found none with significant power or having a $< 70\%$ false alarm probability (FAP). We also carried out this analysis on the residuals for the individual samples separately and, again, found no signs for regular periodicity. In addition, we analyzed the radial velocity data by fitting trends to the total data set and individual samples' residuals and found nothing significant. For the total data set we found a trend of 0.3 m s^{-1} over the 9 year span, which is within the velocity amplitude uncertainty (0.6 m s^{-1}, see Table 5.7).

To quantify our detection limits for additional companions we used a method similar to that of Wittenmyer et al. (2006). We adopted the velocity residuals as a noise sample for simulated orbits. We generated simulated radial velocity orbits for each of 200 period values from 0.8 to 3289 days. The discrete period values were spaced evenly on a logarithmic scale. For each period, we began by assuming a starting velocity semimajor amplitude of 4 m s^{-1}. We calculated 100 orbits for the given period and velocity semiamplitude and selected different time and longitude of periastron passage values with a pseudo-random number generator. We calculated the radial velocity values of the orbits at each of the dates in our measured velocity data set. We scrambled our velocity residuals, also with a pseudo-random number generator, and added them to the simulated data as noise. For each of the 100 trials we calculated a periodogram of the simulated velocity data. If the power at the period used to generate the orbit was found to correspond to a FAP $< 0.1\%$ then that was counted as a successful detection. If 99 of the 100 trials at a velocity semi-

major amplitude resulted in detections then that velocity was considered the detection limit at the period value and the next period value was considered. If two or more non-detections occurred then the velocity semimajor amplitude was increased 0.5 m s^{-1} and the process continued until the velocity limit for the simulated period was found. We carried out this analysis for three different values of orbital eccentricity $e = 0.0$, 0.4, and 0.7. The upper eccentricity limit of 0.7 was chosen because $> 95\%$ of radial velocity detected exoplanet candidates have eccentricities lower than that value. For the simulations with an eccentricity of 0.0, the longitude of periastron is a meaningless parameter, and the 100 randomized values of the time of periastron served to set the relative phase.

With the set of eccentricities, periods, and velocity detection limits derived from this procedure we calculated the corresponding minimum companion masses and astrometric perturbation sizes. The results are shown in Figure 5.6. From these data we infer that our radial velocity data were at least sensitive enough to detect companions with minimum masses $M \sin i > 0.2\ M_{Jup}$, orbital periods $P < 100$ days, and orbital eccentricities < 0.4. For the same orbital eccentricities, companions with $M \sin i > 1.2\ M_{Jup}$ and orbital periods up to 3300 days are ruled out. We also find that radial velocity undetected companions would have a minimum astrometric signature $a \sin i < 0.05$ mas for $P < 1000$ days and reasonable eccentricities, which is beyond the detection threshold of the *HST* observations. Taken together, the periodogram analysis, slope analysis, and simulation of the residuals indicate no additional compan-

ions in the system, verifying that our single companion model to fit the radial velocity and astrometry data was appropriate.

5.6 Discussion

The companion to HD 33636 is likely a M6 V star, with magnitudes $\Delta V \approx 8.0$ and $\Delta K \approx 4.0$ from the G0 V primary (Cox 2000). From this we estimate that HD 33636 should have only a 0.03 mag enhancement in K from that expected for a solitary G0 V star. The two stars' separation at apastron will be $0\farcs15$. Therefore, high-resolution imaging could be useful for additional study of this system.

The mass we find for the companion indicates that it is not a planet at the $\sim 12\sigma$ level assuming the standard 13 M_{Jup} upper limit for planets. This is the first definitive example of a planet candidate that was detected with the radial velocity method and later found to have a non-planetary mass. Previously, Reffert & Quirrenbach (2006) analyzed the *Hipparcos* Intermediate Astrometric Data for HD 38529 and 168443 with radial velocity data as a constraint and found companion masses $M = 37^{+36}_{-19}$ M_{Jup} and $M = 34 \pm 12$ M_{Jup} respectively. However, these are both < 1.8 σ results and more observations are needed to refine these estimates.

In contrast, Benedict et al. (2002a), McArthur et al. (2004), and Benedict et al. (2006) have directly confirmed the planetary nature of exoplanets around GJ 876, ρ^1 Cancri, and ϵ Eridani with the same method used in this study. The GJ 876 and ρ^1 Cancri systems contain additional, non-

astrometrically detected companions. If these systems are coplanar then the additional companions are also planets. Four other planet candidates originally detected with the radial velocity method have been observed to transit their host star, HD 209458 b (Henry et al. 2000; Charbonneau et al. 2000), HD 189733 b (Bouchy et al. 2005), HD 149026 b (Sato et al. 2005), and GJ 436 b (Gillon et al. 2007), and thus have measured masses and are confirmed planets.

From mathematical arguments, the median value for the inclination of binary (star + star or star + planet) orbits is 60°. This is supported by the distribution of the inclinations of visual binary star orbits in the Washington Double Star Catalog (Mason & Hartkopf 2006), which has a broad peak in frequency centered around 60°. An inclination $i = 60°$ corresponds to a multiplicative factor of 1.15 to the minimum mass calculated from spectroscopic orbit parameters. Therefore, we expect that most of the candidate exoplanets detected with the radial velocity method and having minimum masses $M \sin i < 11 M_{Jup}$ are actually planets.

Nearly face-on orbits, like the one we have determined for the HD 33636 system, should be rare. Orbits with $i \leq 5°$ are expected to make up only 0.4% of an unbiased distribution. Nevertheless, our result is a striking example proving that minimum masses are not true masses and that not all of the planet candidates are actual planets. This demonstrates the value of follow-up astrometric observations and photometric monitoring for potential transits to determine the true masses of exoplanet candidates detected with the radial

velocity method.

Valenti & Fischer (2005) found HD 33636's iron abundance [Fe/H] = -0.13 ± 0.03, which is consistent with the solar neighborhood average (Allende Prieto et al. 2004), but on the lower end of the distribution of stars with detected planet candidate companions (Fischer & Valenti 2005). Although HD 33636's companion falls outside the period range ($P < 4$ years) considered by Fischer & Valenti (2005), it is reasonable to assume that the metallicities of host stars to high-mass planets at all periods should be distributed at similar high values as is suggested by the core accretion model of planet formation. For stars with -0.50 $\leq$ [Fe/H] $\leq$ 0.0, Fischer & Valenti (2005) found a planet candidate detection rate $< 3\%$. Above solar metallicity, they found the detection rate increased, and was up to 25% for stars with [Fe/H] $> +0.3$ dex. In this context, the fact that HD 33636 is not a planet hosting star is not as surprising as it would have been if it had [Fe/H] $\gg 0.0$, because removing it from the sample strengthens the correlation between planets and host star metallicity.

Along the lines of planet host star abundances, Ecuvillon et al. (2006) and Chen & Zhao (2006) have included HD 33636 as a planet hosting star for studies of oxygen and lithium abundances respectively. Ecuvillon et al. (2006) found that planet hosting stars could have oxygen abundances, [O/H], enhanced from a volume limited control sample by 0.1 – 0.2 dex, but that there was a large uncertainty in the measurements and ambiguity with the effects of galactic chemical evolution. Chen & Zhao (2006) found that planet

hosting stars could have depleted lithium abundances relative to stars without detected planet companions. HD 33636 was found to be slightly oxygen rich ($\sim$ 0.1 dex) relative to control samples stars with similar [Fe/H] in the Ecuvillon et al. (2006) study. Conversely, Chen & Zhao (2006) found that HD 33636 showed no signs of lithium depletion as was the case in many other ostensibly planet hosting stars.

Another study with conclusions that could be affected by our result was done by Beichman et al. (2005), who looked for infrared excess due to debris disks around planet hosting stars with *Spitzer*. HD 33636 was one of six planet hosting stars that showed excess emission at 70 μm and it also was one of the three that showed the most significant excess. In addition, Beichman et al. (2005) found six stars that did not have detected planets showing the same type of excess. Moving HD 33636 from the planet hosting sample to the non-planet hosting sample has the effect of increasing the offset in the frequency distribution for 70 μm excess between the two samples. Surprisingly, the non-planet hosting stars then have a higher infrared excess detection rate (7/60) than the planet hosting stars (6/80). This indicates there is no special correlation between planets and debris disks within the current planet and disk detection limits. Both this study, and the two mentioned above, depend on data that is difficult to measure. Resolving a true planet population from the sample of planet candidates with mass measurements will ultimately increase the impact of these and other similar studies and also permit new studies to be undertaken.

Table 5.1. HET Radial Velocities for HD 33636

HJD - 2450000.0	RV (m s^{-1})
3633.9377	85.6 ± 3.2
3646.9084	64.7 ± 3.3
3653.9013	74.5 ± 3.5
3663.8716	65.8 ± 2.9
3666.8409	66.9 ± 3.2
3668.8329	62.5 ± 3.4
3676.8395	61.8 ± 3.5
3678.8104	58.0 ± 2.9
3680.8050	56.1 ± 3.0
3682.7969	55.4 ± 3.2
3683.8119	48.8 ± 3.3
3689.9219	44.3 ± 3.2
3691.7897	51.9 ± 3.0
3692.7895	47.8 ± 2.9
3696.7711	47.4 ± 3.0
3697.7683	50.3 ± 2.9
3700.7600	47.3 ± 2.6
3703.7523	43.0 ± 4.0
3708.8624	43.2 ± 3.3
3709.8785	40.5 ± 3.4
3713.7238	48.2 ± 3.9
3714.8699	43.7 ± 3.9
3719.6983	41.3 ± 4.1
3719.8439	43.1 ± 3.9
3724.8191	41.2 ± 3.4
3724.8225	39.7 ± 3.6
3730.6675	31.5 ± 3.7
3731.6737	40.8 ± 3.5
3732.6648	41.4 ± 3.5
3738.6609	38.7 ± 3.1
3739.6456	32.5 ± 3.4
3746.6229	37.7 ± 4.7
3748.6334	30.4 ± 3.7
3751.7516	25.9 ± 3.4
3753.7481	28.9 ± 3.7
3754.6125	28.6 ± 3.7
3755.6016	28.7 ± 3.6
3757.7514	24.6 ± 3.9
3762.5922	26.2 ± 4.4
3985.9800	-21.3 ± 3.4
3987.9655	-31.4 ± 2.7
3988.9695	-30.3 ± 2.7
3989.9691	-31.3 ± 2.7
3990.9631	-32.3 ± 2.7
3997.9516	-27.1 ± 2.7
4007.9220	-33.6 ± 2.8
4008.9051	-32.9 ± 3.1
4014.9009	-35.0 ± 2.7

Table 5.1 (cont'd)

HJD - 2450000.0	RV (m s^{-1})
4015.9059	-33.7 ± 3.3
4018.8874	-35.4 ± 3.0
4019.8780	-36.6 ± 2.8
4020.8750	-38.4 ± 3.0
4021.8729	-37.5 ± 3.0
4031.8466	-38.2 ± 3.1
4072.7382	-45.0 ± 3.4
4073.7364	-43.6 ± 3.0
4075.8628	-46.1 ± 3.0
4076.7277	-44.4 ± 3.1
4079.7194	-37.6 ± 3.3
4080.8438	-45.4 ± 3.0
4081.8592	-48.9 ± 3.2
4105.6559	-48.5 ± 4.0
4106.7734	-50.6 ± 3.7
4108.7813	-50.5 ± 3.9
4109.7746	-51.8 ± 3.7
4110.7867	-48.8 ± 4.3
4121.6098	-51.6 ± 4.1

Table 5.2. The Radial Velocity Samples

Sample	Time Span	N	RMS (m s^{-1})
Lick	1998.05 – 2001.69	12	13.6
Keck	1998.07 – 2006.68	27	4.2
Elodie	1998.13 – 2003.23	42	12.2
HET	2005.72 – 2007.05	67	3.3

Table 5.3. Log of FGS1r Observations

HJD - 2450000.0	N[a]	*HST* Roll (°)
3603.2802	4	281.4
3605.2786	4	281.0
3606.5443	4	281.0
3610.2767	4	281.0
3613.1421	3	281.5
3615.4771	4	281.0
3658.0422	2	246.9
3662.0402	4	247.6
3667.3715	4	247.7
3669.1033	4	250.9
3670.2403	4	245.6
3723.0689	4	182.0
3967.5470	4	281.7
3969.6785	3	281.0
3972.3435	3	281.0
4031.4272	4	251.9
4033.1582	4	251.9
4035.2237	4	251.9

[a]Number of observations of HD 33636 per epoch.

Table 5.4. Astrometric Reference Star Data

Identification	Spectral Type	V	$B-V$	A_V	M_V[a]	π_{abs} (mas)
Ref-1	F6 V	15.2	0.6	0.5	3.6	0.6 ± 0.1
Ref-2	F6 V	14.1	0.6	0.4	3.6	0.9 ± 0.2
Ref-3	K6 V	15.3	1.3	0.1	7.3	2.6 ± 0.5
Ref-4	G2 V	13.1	0.6	0.1	4.6	2.0 ± 0.4
Ref-5	K3 III	9.9	1.3	0.1	0.3	1.2 ± 0.2

[a]Taken from Cox (2000) for the measured spectral types.

Table 5.5. Astrometry Catalog

Star	α^{a} (arcsec)	δ^{a} (arcsec)	π_{abs} (mas)	μ_{α} (mas)	μ_{δ} (mas)
HD 33636	-97.8347 ± 0.0003	803.0143 ± 0.0005	35.6 ± 0.2	169.0 ± 0.3	-142.3 ± 0.3
Ref-1	-172.1200 ± 0.0004	800.5260 ± 0.0005	5.7 ± 0.1	8.6 ± 0.6	-9.2 ± 0.5
Ref-2	-159.6280 ± 0.0002	775.5080 ± 0.0005	9.2 ± 0.1	0.6 ± 0.3	-12.2 ± 0.3
Ref-3	-113.6041 ± 0.0004	588.7119 ± 0.0005	2.6 ± 0.2	-4.1 ± 0.6	4.8 ± 0.5
Ref-4	-216.5286 ± 0.0003	618.6621 ± 0.0005	2.0 ± 0.2	-1.2 ± 0.4	-2.5 ± 0.4
Ref-5	-262.7320 ± 0.0002	583.6012 ± 0.0005	1.2 ± 0.1	0.0 ± 0.2	-6.0 ± 0.2

[a]The right ascension and declination coordinates are relative to $\alpha = 4^{h}10^{m}22\overset{s}{.}66, \delta = 5^{\circ}13'29\overset{''}{.}0$, J2000.0

Table 5.6. Summary of *HST* Astrometry

Parameter	Value
HST study duration	1.2 yr
Number of HD 33636 obsrvations	67
Number of epochs	18
Number of reference stars	5
HD 33636 (V)	7.1
Reference stars $\langle(V)\rangle$	13.5
HD 33636 ($B-V$)	0.6
Reference stars $\langle(B-V)\rangle$	0.9
HST parallax[a]	35.6 ± 0.2 mas
Hipparcos parallax	34.9 ± 1.3 mas
HST proper motion[a]	220.9 ± 0.4 mas yr^{-1}
In position angle[a]	130.°1 ± 0.°1
Hipparcos proper motion	227.0 ± 1.4 mas yr^{-1}
In position angle	127.°2 ± 0.°3

[a]From the simultaneous modeling of the radial velocity and astrometry data.

Table 5.7. HD 33636 Perturbation Orbit Parameters and Companion Mass

Parameter	Value
K_A	163.5 ± 0.6 m s^{-1}
P	2117.3 ± 0.8 days
T_0(JD)	2451198.3 ± 2.0
e	0.48 ± 0.02
ω	$337\overset{\circ}{.}0 \pm 1\overset{\circ}{.}6$
a_A	14.2 ± 0.2 mas
Ω	$125\overset{\circ}{.}6 \pm 1\overset{\circ}{.}6$
i	$4\overset{\circ}{.}0 \pm 0\overset{\circ}{.}1$
M_B	142 ± 11 M_{Jup}[a]
M_B	0.14 ± 0.01 $M_\odot$[a]

[a]Assuming $M_A = 1.02 \pm 0.03 M_\odot$ (Takeda et al. 2007).

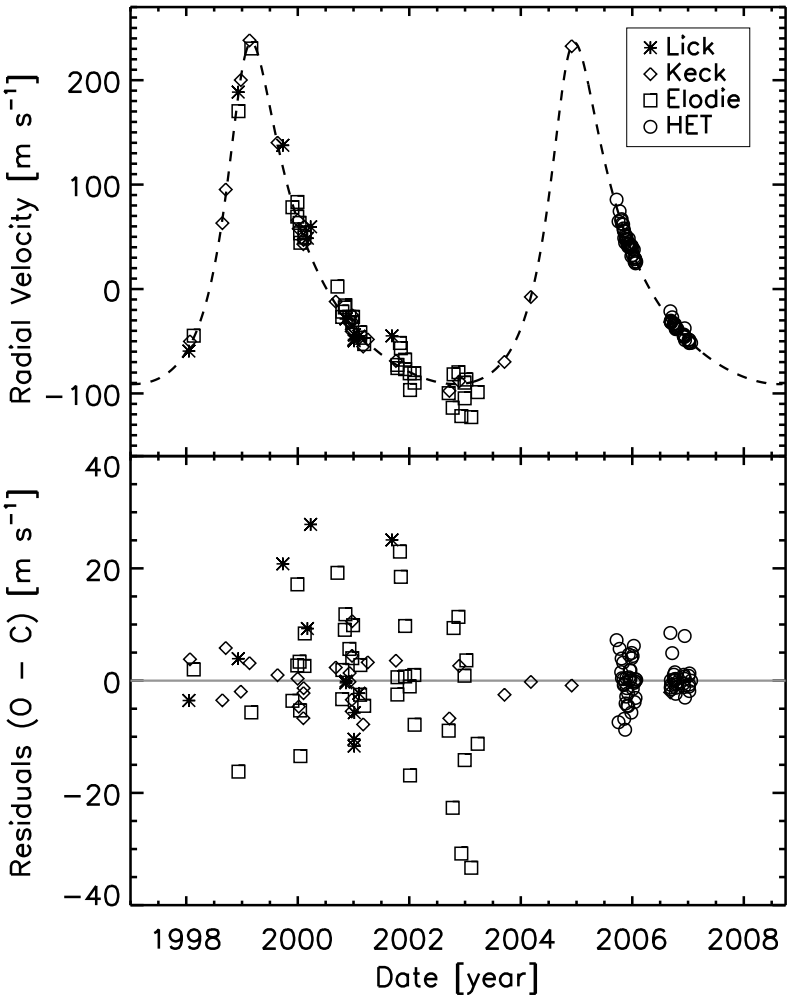

Figure 5.1 Upper panel: Radial velocities (points) as function of time and the best fit (dashed line) from the simultaneous fit to the radial velocity and astrometry data. The error bars are omitted for clarity. Bottom Panel: Residuals from the fit (points).

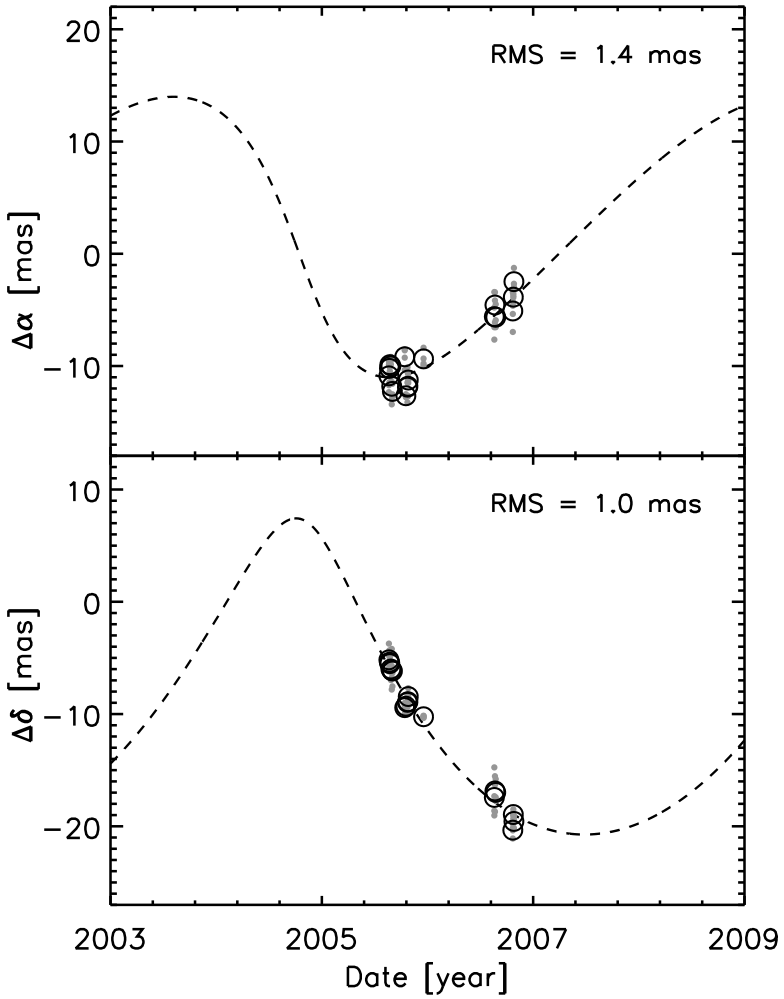

Figure 5.2 Right ascension (α) and declination (δ) components of HD 33636's perturbation orbit as a function of time (points) and the best fit (dashed line) from the simultaneous modeling of the radial velocities and astrometry. The dots are the individual observations and the circles are per epoch (single *HST* orbit) normal points consisting of 2 – 4 individual observations.

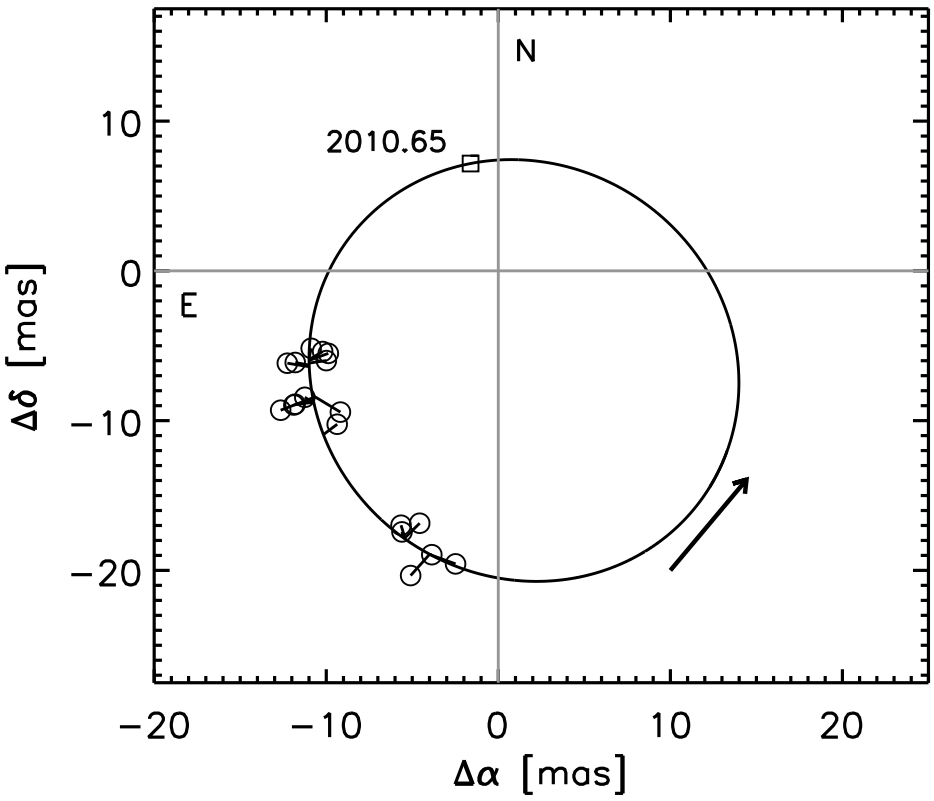

Figure 5.3 Perturbation orbit of HD 33636 on the sky (line). The open circles are the *HST* epoch normal points and are connected to the derived orbit by residual vectors. The *HST* data cover 20% of the orbit period. The orbital motion direction is indicated by the arrow. The square marks the location of periastron passage and the next time of occurrence is labeled.

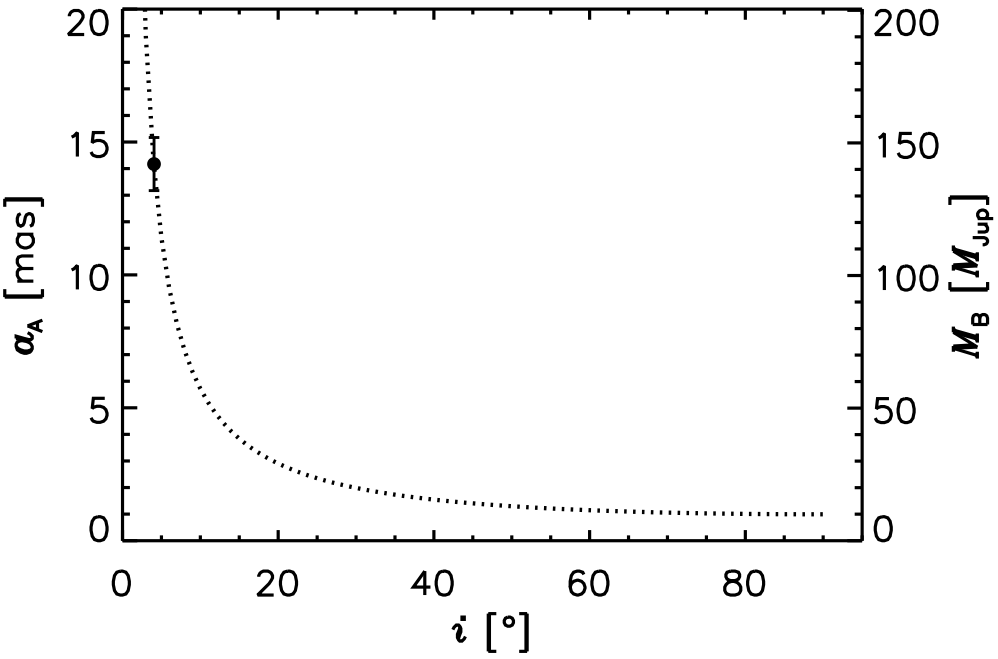

Figure 5.4 The relationship (dotted line) between the perturbation size (a_A) and inclination angle (i) for fixed P, K_A, e, and π_{abs} through the Pourbaix & Jorissen (2000) relationship (eq. [6]). Our determined value for the perturbation size and inclination is given by the filled circle. The right axis maps the inclination to the corresponding companion mass (M_B). Our adopted value for the uncertainty in the companion mass is plotted as the error bar for this axis. The formal uncertainties in our determined a_A and i are smaller than the point.

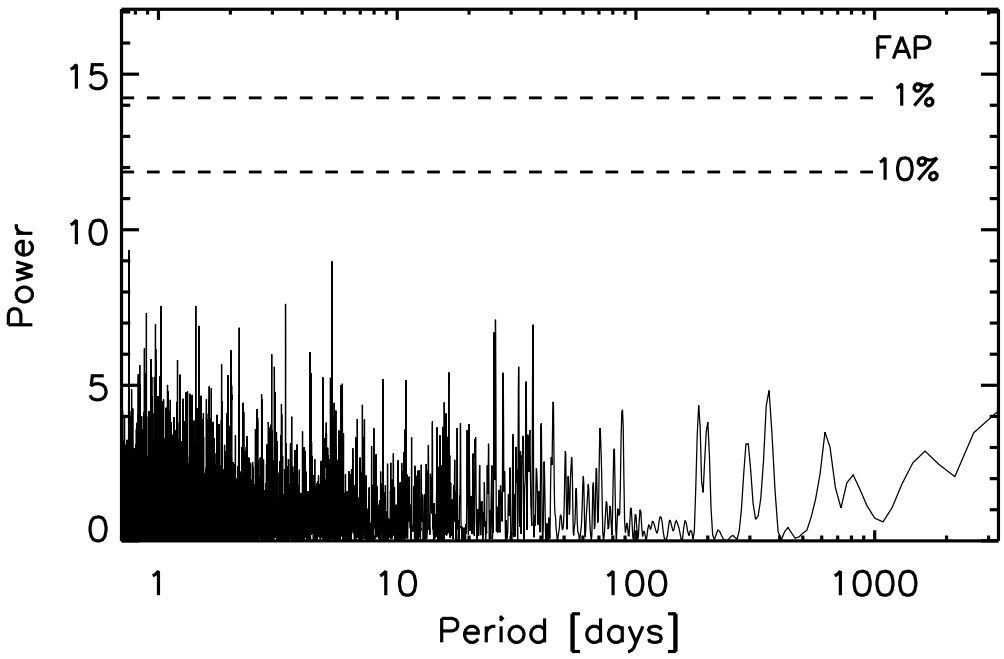

Figure 5.5 Periodogram of the radial velocity residuals from the best fit, single-companion orbit with 1% and 10% false alarm probability (FAP) limits indicated. No periodicity is detected with FAP $< 70\%$, which indicates that there are no additional companions in the system for our detection limits (see §5.5).

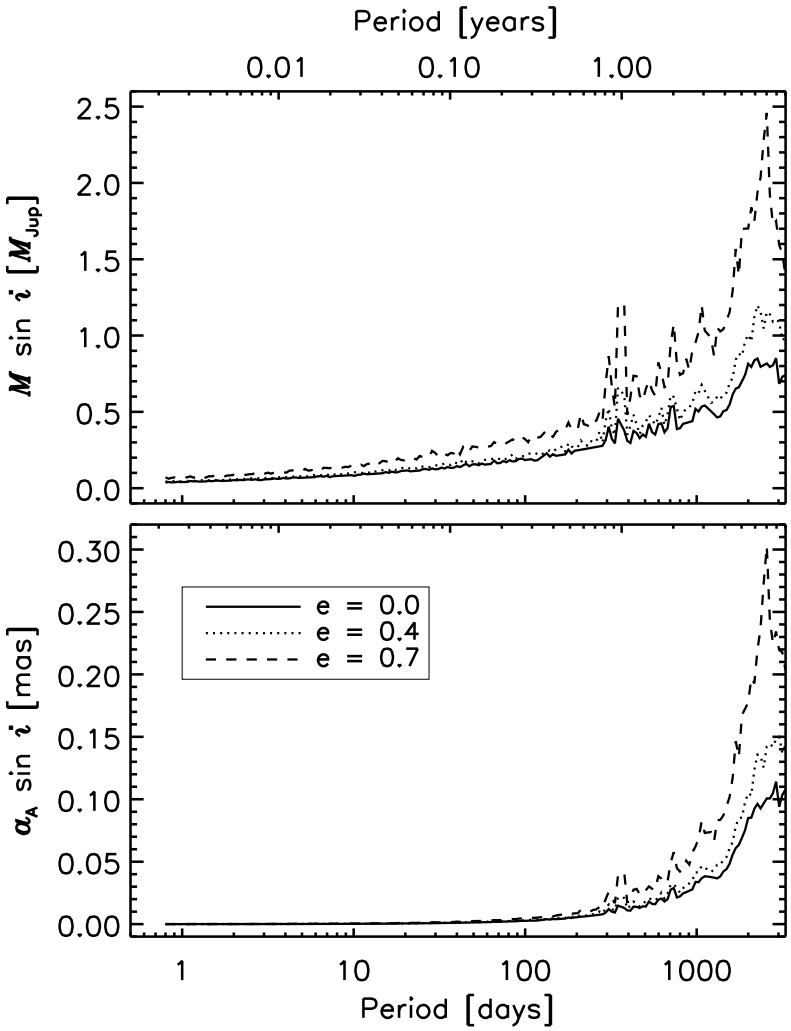

Figure 5.6 Results from the detection limit simulations converted to hypothetical companion minimum masses ($M \sin i$, upper panel) and minimum astrometric perturbation size of HD 33636 ($a_A \sin i$, lower panel). The different lines represent the different assumed eccentricity values. Values above the lines would have been detected with a periodogram analysis of the radial velocity data.

Chapter 6

Conclusion

The research contained in this dissertation was primarily focused on the determination of M dwarf metallicities to aid the study of extrasolar planets. I first described the development of a spectral analysis technique that yields accurate metallicities for M dwarfs. This technique depends on newly revised cool-star model atmospheres and spectrum synthesis code. I then presented the results of applying this technique to determine the metallicities of some M dwarf planet hosts and M dwarfs with precisely measured masses and luminosities. In addition, I presented complementary work to determine the true mass of an extrasolar planet candidate. The specific implications of the results from each project were discussed at the end of their respective chapters. Here I discuss the broader implications and the future prospects for this type of research.

The long-term impact of my work on M dwarf metallicities will not be any particular result that was or is obtained with the technique I developed. Spectral analysis techniques are constantly changing and there is never a consensus on the "right" way to determine stellar abundances even for solar type stars. It is entirely possible, and even likely, that a better way to determine

M dwarf compositions will be developed in the near-future. It might require just a small change in our approach, or it might be a wholesale change. I note that obtaining and analyzing M dwarf spectra in the near-IR is a particularly promising avenue for research. The ongoing development of high resolution, large format near-IR spectrographs like CRIRES (Käufl et al. 2004) could be just the tool necessary to advance chemical abundance determinations for M dwarfs.

So rather than the technique or specific results, the biggest long-term impact will be through the improvements in the PHOENIX model atmospheres and the MOOG stellar analysis code that were made during the course of this research. These models and code are used by a large number of people working on many different projects. MOOG in its various forms has been in popular use for over 30 years, while the PHOENIX models have been synonymous with the analysis of cool-stars for 15 years. The improvements to both reinforce and expand their usefulness for cutting-edge research. The benefits of this will continue to be felt long after the specific results of this dissertation have been superseded.

Stellar astrophysics research to assist the study of extrasolar planets will remain a profitable enterprise for a long time to come, and not just for "problematic" stars like M dwarfs. Planetary host stars will always be much easier to study than the planets themselves and we still do not know enough about even solar-type stars. Seemingly simple things like estimating the mass, composition, and age of a normal star remain fraught with systematics, but

are crucial for exoplanet studies.

The recent discoveries by Udry et al. (2007) that GJ 581 hosts two super-Earth planets and by Gillon et al. (2007) that the Neptune-mass planet around GJ 436 transits underline the extra importance of M dwarfs in the field of planetary science. It is easier to detect low-mass planets with the radial velocity and transit methods around M dwarfs than higher mass stars. Five out of the ten lowest mass exoplanets found so far are orbiting M dwarfs, this despite the larger attention placed on FGK-type stars by extrasolar planet searches. In the coming years the importance of M dwarfs in the study of planets will only grow as more low-mass planets are discovered around these stars. It is very possible that the first truly Earth-mass in a star's habitable zone will be found around an M dwarf. Therefore, these stars warrant continued study. The research on these stars that I have described in this dissertation will hopefully only be a benchmark for future progress.

The work I have presented on determining the mass of an extrasolar candidate with astrometry and radial velocities further illustrates the value of using astrometry to study extrasolar planets. High-precision astrometry is a necessary component for the full characterization of exoplanetary systems. However, it is a severely under-appreciated and under-utilized tool. Such fundamental knowledge as component masses and orbital coplanarity for the vast majority of exoplanet systems will remain unknown without the development of technology to permit higher-precision astrometric measurements than are currently possible. With the looming cancellation of the *Space Interferometry*

Mission (*SIM*), the prospects for astrometry to make a very significant impact on the field of extrasolar planets is severely reduced. *SIM* represents perhaps the best chance to discover an Earth analog in the next ten years.

Work with the FGS on the *HST* will continue, but this is limited to very select systems and results in incomplete characterization of multi-planet systems. The European Space Agency's (ESA) *GAIA* mission has the potential to vastly improve the characterization of the majority of known exoplanetary systems and discover giant planets at further separations from their host stars than is feasible with radial velocity surveys (Perryman et al. 2005). It will be the first astrometric survey with the ability to detect significant numbers of planets. But, the breakthrough detection of Earth analogs will likely be out of its reach and will require an astrometry-capable space telescope dedicated to exoplanetary science like *SIM*.

High-precision ground-based astrometry with interferometry looked very promising 5 – 10 years ago. But, progress in developing the needed technology has been slower than expected. Telescope systems like the Keck Interferometer and the Very Large Telescope Interferometer remain in development and the first definitive ground-based exoplanet detection remains elusive. Nevertheless, ground and space-based astrometry should continue to be pursued aggressively in order to advance the field of exoplanetary science.

Appendix

Appendix 1

Modifications to MOOG

As mentioned in §2.4.1, we modified MOOG extensively to extend its capabilities to the low temperature regime of M dwarfs. The following sections detail the specific changes we made regarding the treatment of molecules and their basic data. Some, but not all, of these changes have been incorporated in the standard release of MOOG available at C. Sneden's website[1]. We also made a number of changes to the code structure, like increasing the number of lines allowed per spectrum point for example, that were necessary for this project. These are all included in the latest code release and should be invisible to most users.

1.1 Default Species for Chemical Equlibrium

We modified MOOG to carry out chemical equilibrium calculations for an extensive set of molecules and atoms. This list includes species needed for continuous opacity and damping calculations in addition to the ions and molecules that have an affect on the partial pressures of the following: H, He, C, N, O, Mg, Al, Si, P, S, Cl, Ca, Ti, V, Cr, and Fe for gas temperatures

[1] `http://verdi.as.utexas.edu/moog.html`

$T > 1500$K. The list of the species and the corresponding set of linear equations relating the parent element fictitious pressures, P, to the species partial pressures, p, and satisfying the conservation of nuclei condition are

$$\begin{aligned}
P(\mathrm{H}) &= p(\mathrm{H}) + p(\mathrm{H}^+) + 2p(\mathrm{H_2}) + p(\mathrm{CH}) + p(\mathrm{NH}) + p(\mathrm{OH}) + \\
&\quad p(\mathrm{MgH}) + p(\mathrm{AlH}) + p(\mathrm{SiH}) + p(\mathrm{PH}) + p(\mathrm{SH}) + p(\mathrm{ClH}) + \\
&\quad p(\mathrm{CaH}) + p(\mathrm{CrH}) + p(\mathrm{FeH}) + 2p(\mathrm{CH_2}) + 2p(\mathrm{NH_2}) + \\
&\quad 2p(\mathrm{H_2O}) + 2p(\mathrm{PH_2}) + 2p(\mathrm{SH_2}) + p(\mathrm{HCO}) + p(\mathrm{MgOH}) + \\
&\quad p(\mathrm{AlOH}) + p(\mathrm{CaOH}), \qquad (1.1) \\
P(\mathrm{He}) &= p(\mathrm{He}) + p(\mathrm{He}^+), \qquad (1.2) \\
P(\mathrm{C}) &= p(\mathrm{C}) + p(\mathrm{C}^+) + p(\mathrm{CO}) + p(\mathrm{CH}) + 2p(\mathrm{CH_2}) + p(\mathrm{HCO}) + \\
&\quad p(\mathrm{CN}) + p(\mathrm{CS}) + p(\mathrm{CO_2}), \qquad (1.3) \\
P(\mathrm{N}) &= p(\mathrm{N}) + p(\mathrm{N}^+) + 2p(\mathrm{N_2}) + p(\mathrm{NH}) + p(\mathrm{NH_2}) + p(\mathrm{CN}) + \\
&\quad p(\mathrm{NO}) + p(\mathrm{SiO}) + p(\mathrm{PN}) + p(\mathrm{SN}), \qquad (1.4) \\
P(\mathrm{O}) &= p(\mathrm{O}) + p(\mathrm{O}^+) + p(\mathrm{CO}) + p(\mathrm{OH}) + p(\mathrm{H_2O}) + p(\mathrm{HCO}) + \\
&\quad p(\mathrm{MgOH}) + p(\mathrm{AlOH}) + p(\mathrm{CaOH}) + 2p(\mathrm{CO_2}) + p(\mathrm{NO}) + \\
&\quad 2p(\mathrm{O_2}) + p(\mathrm{MgO}) + p(\mathrm{SiO}) + p(\mathrm{PO}) + p(\mathrm{SO}) + \\
&\quad p(\mathrm{TiO}) + p(\mathrm{VO}) + p(\mathrm{FeO}), \qquad (1.5) \\
P(\mathrm{Mg}) &= p(\mathrm{Mg}) + p(\mathrm{Mg}^+) + p(\mathrm{MgH}) + p(\mathrm{MGOH}) + p(\mathrm{MgO}), \qquad (1.6) \\
P(\mathrm{Al}) &= p(\mathrm{Al}) + p(\mathrm{Al}^+) + p(\mathrm{AlH}) + p(\mathrm{AlOH}), \qquad (1.7) \\
P(\mathrm{Si}) &= p(\mathrm{Si}) + p(\mathrm{Si}^+) + p(\mathrm{SiH}) + p(\mathrm{SiO}) + p(\mathrm{SiS}), \qquad (1.8) \\
P(\mathrm{P}) &= p(\mathrm{P}) + p(\mathrm{P}^+) + p(\mathrm{PH}) + p(\mathrm{PH_2}) + p(\mathrm{PN}) + p(\mathrm{PO}), \qquad (1.9)
\end{aligned}$$

$$
\begin{aligned}
P(\mathrm{S}) &= p(\mathrm{S}) + p(\mathrm{S}^+) + p(\mathrm{SH}) + p(\mathrm{SH_2}) + p(\mathrm{SC}) + p(\mathrm{SN}) + \\
&\quad p(\mathrm{SO}) + p(\mathrm{SiS}), && (1.10)\\
P(\mathrm{Cl}) &= p(\mathrm{Cl}) + p(\mathrm{Cl}^+) + p(\mathrm{ClH}), && (1.11)\\
P(\mathrm{Ca}) &= p(\mathrm{Ca}) + P(\mathrm{Ca}^+) + p(\mathrm{CaH}) + p(\mathrm{CaOH}), && (1.12)\\
P(\mathrm{Ti}) &= p(\mathrm{Ti}) + p(\mathrm{Ti}^+) + p(\mathrm{TiO}), && (1.13)\\
P(\mathrm{V}) &= p(\mathrm{V}) + p(\mathrm{V}^+) + p(\mathrm{VO}), && (1.14)\\
P(\mathrm{Cr}) &= p(\mathrm{Cr}) + p(\mathrm{Cr}^+) + p(\mathrm{CrH}), && (1.15)\\
P(\mathrm{Fe}) &= p(\mathrm{Fe}) + p(\mathrm{Fe}^+) + p(\mathrm{FeH}) + p(\mathrm{FeO}). && (1.16)
\end{aligned}
$$

The 72 unique species on the right-side of the equations are the species that were included for all MOOG calculations described in this dissertation. They are also now the default species for chemical equilibrium calculations in the standard release of MOOG. The list is contained in an array in the "Bmolec" subroutine.

The fictitious pressures are related to the number densities (abundances) of an element, N, through the ideal gas law. The equation for an example element, X, is

$$P(\mathrm{X}) = N(\mathrm{X})kT, \tag{1.17}$$

where k is the Boltzmann constant and T is the temperature.

1.2 Molecular Data

Molecular dissociation energies, D_0, and chemical equilibrium constants, K_p, are needed to solve for individual atomic and molecular species partial pressures and calculate electron energy level populations in MOOG. The equilibrium constants are defined as

$$K_p(XY) \equiv \frac{p(\mathrm{X})p(\mathrm{Y})}{p(\mathrm{XY})}, \tag{1.18}$$

where XY is an example molecule composed of one atom each of elements X and Y. They may be calculated from partition functions, Q, using the molecular Saha equation

$$K_p(XY) = kT\left(\frac{2\pi kT}{h^2}\right)^{\frac{3}{2}}\left(\frac{M(\mathrm{X})M(\mathrm{Y})}{M(\mathrm{XY})}\right)^{\frac{3}{2}}\left(\frac{Q(\mathrm{X})Q(\mathrm{Y})}{Q(\mathrm{XY})}\right)e^{\frac{D_0(\mathrm{XY})}{kT}}, \tag{1.19}$$

where h is the Plank constant and M is the species mass. We adopted equilibrium constants from fitting the PHOENIX partial pressure data to maintain complete consistency with the model atmospheres, but also checked the derived values against those calculated directly from the partition functions. The adopted dissociation energies (from Sauval & Tatum 1984) and coefficients, c_n, for the polynomial fits are given in Table 1.1. The chemical equilibrium constants are calculated from this data with the formula

$$K_p = \sum_{n=0}^{4} c_n(log\ \theta)^n - D_0\theta. \tag{1.20}$$

This data is also included in the "Bmolec" subroutine of the standard release of MOOG.

Table 1.1. Molecular Data in MOOG

Species	D_0 (eV)	c0	c1	c2	c3	c4
H_2	4.4781	12.1174	-1.0476	1.6851	-5.5831	4.0060
CH	3.4650	11.5335	-0.5211	-0.7475	0.1494	-0.1967
NH	3.4700	11.4657	-0.7265	-0.6439	0.0004	0.1269
OH	4.3920	11.8018	-0.8525	-0.5525	0.1625	-0.1935
FH	5.8690	12.2897	-0.9174	-0.6416	0.1616	-0.1222
NaH	1.8800	10.7189	-0.8053	4.1674	-12.8321	10.8590
MgH	1.3400	10.2878	-0.3455	0.1677	-3.8628	4.7348
AlH	3.0600	11.4876	-0.4024	-0.4809	-1.6283	2.5415
SiH	3.0600	11.2586	-0.6758	-0.5870	0.0669	0.3139
PH	3.3000	11.3387	-0.2112	0.5964	0.2027	0.2323
SH	3.5500	11.4380	-0.7731	-0.4785	0.1716	-0.2326
ClH	4.4336	11.9042	-0.8250	-0.6309	0.1545	-0.1999
CaH	1.7000	10.1987	-0.9426	1.8085	-4.6629	3.4971
CrH	2.1700	10.4501	-3.4047	-2.5032	1.6933	-2.1073
MnH	1.3100	9.7219	-3.9379	-3.4116	0.6378	-3.0173
FeH	2.4100	12.1214	0.9531	2.3351	-0.2231	3.0718
NiH	2.7000	11.9592	-0.9476	-0.4685	0.8228	0.2487
CuH	2.8400	11.3419	-1.3372	-0.6389	1.5957	-0.4408
CH_2	7.9400	23.8688	-1.7944	4.4565	-10.8615	6.6375
NH_2	7.4400	23.7463	-1.7687	4.2349	-12.2375	8.6009
H_2O	9.6221	24.6063	-1.8370	3.9590	-10.9331	7.4896
PH_2	6.4895	23.0957	-2.0802	5.0222	-10.7703	5.8343
SH_2	7.5946	23.8619	-1.7009	4.4792	-11.4475	7.2724
BOH	12.7425	25.2365	-1.2673	5.1472	-12.0672	7.6325
HCN	13.2363	25.1400	-1.3548	5.4650	-12.6262	7.5607
COH	11.8560	24.6494	-1.6665	4.8174	-10.9079	6.7311
NOH	8.6140	24.4465	-1.3261	-0.5924	0.0156	-0.7950
NaOH	8.0150	23.3475	-1.4238	7.1752	-17.8186	13.4471
MgOH	8.0735	23.3316	-1.3691	6.1267	-15.3175	11.1568
AlOH	10.1252	25.2641	-1.4342	5.1091	-13.2682	9.2414
KOH	8.1892	23.3235	-1.9306	8.6260	-17.6081	10.5153
CaOH	8.7035	23.2006	-1.9644	8.3448	-17.4669	10.8898
BaOH	9.0621	23.3508	-2.9133	7.9864	-14.7824	10.4060
BO	8.2800	12.6247	-0.6958	-0.4147	0.2800	-0.4535
C_2	6.2100	12.4677	-0.4434	-0.0516	-0.1304	-0.0555
CN	7.7600	12.4439	-0.4823	-0.4724	-1.1721	1.3124
CO	11.0920	13.2412	-0.8502	-0.0724	-0.2098	-0.2096
SiC	4.6400	11.8943	-1.2037	2.5280	-5.4728	3.5183
CP	6.8950	13.0550	1.1581	2.9371	0.6616	1.9298
CS	7.3550	12.8508	-0.7689	-0.4254	1.9738	-2.7599
C_3	13.8610	26.3157	-1.9852	4.7933	-10.1191	6.4350
SiC_2	13.1966	25.7482	-0.8673	6.1588	-14.8609	10.8245
ClCN	12.2076	25.3546	-0.9498	6.1809	-13.9272	8.7748
CO_2	16.5382	26.9665	-1.5802	5.2319	-12.8507	7.2799
CS_2	11.9993	26.2469	-1.0515	6.3688	-12.9191	7.5525
N_2	9.7594	12.8868	-0.8861	0.2644	-1.4001	0.9645
NO	6.4968	11.9347	-0.7631	0.0848	-0.8149	0.4636

Table 1.1 (cont'd)

Species	D_0 (eV)	c_0	c_1	c_2	c_3	c_4
NF	2.8190	11.4441	-1.2536	-0.9028	-0.5407	-0.8453
SiN	4.5100	11.9190	-0.7171	-0.7889	-1.6147	1.2567
NP	7.1110	12.1020	-1.2837	0.4612	-1.4609	0.1464
NS	4.8000	11.9264	-1.0597	2.7095	-6.0355	3.6858
N_2O	11.4400	25.8228	-1.8022	5.4142	-13.7572	7.8651
NO_2	9.6210	25.4890	-2.1013	4.7855	-12.0992	6.7146
O_2	5.1156	12.8763	-0.4923	-0.5474	0.2097	-0.3337
NaO	3.0790	11.1443	0.1006	1.3407	-0.8726	1.1604
MgO	3.5300	10.7965	-0.4336	4.5543	-9.6555	6.8587
AlO	5.2700	12.2111	-0.5018	-0.0903	-1.3613	1.7974
SiO	8.2600	12.9276	-0.7698	-0.5315	2.1774	-2.8482
PO	6.0710	11.9149	-1.0730	0.4169	-0.8595	-0.0207
SO	5.3590	12.3424	-0.8964	2.5742	-6.2111	3.7515
ClO	2.7450	11.8129	-1.0573	2.2239	-5.7356	3.2844
CaO	4.5310	11.7806	1.6875	3.1813	-5.1106	4.8826
ScO	6.9600	12.5239	-1.2329	1.5239	-1.9903	0.4735
TiO	6.8700	12.3189	-1.8737	4.2408	-7.4936	3.3890
VO	6.4100	12.8103	-0.5642	-0.5910	-2.5261	3.9417
FeO	4.2000	12.5333	-1.0582	1.0158	-1.5253	0.7221
YO	7.2900	12.4455	-1.3319	1.0692	0.0949	-2.0131
ZrO	7.8500	12.4688	-1.0832	0.0935	-0.2133	0.5480
BaO	5.4410	11.5981	-2.2831	-1.3418	4.2093	-4.0635
LaO	8.2300	12.1926	0.1654	-0.8084	-1.0001	1.1994
SiO_2	13.0355	26.5705	-1.1245	6.0979	-12.6131	7.8414
SO_2	11.1405	25.9338	-1.3799	5.5465	-11.7480	7.0670
TiO_2	13.2915	25.9435	-2.1804	7.1450	-13.0296	7.9278
YO_2	15.2000	25.8616	-1.4066	-0.5348	2.4526	-1.0943
ZrO_2	14.4650	25.6438	-2.2794	6.4569	-11.9176	7.3456
LaO_2	21.1510	31.0796	10.7083	13.0309	9.1626	10.4251
Al_2O	10.9653	24.8867	-0.8364	6.6875	-15.6083	11.6178
F_2	1.5920	12.6197	-0.4363	-0.5840	0.4907	-0.6261
NaF	4.9530	11.4755	-0.4941	0.6264	-1.1793	0.5988
NaMg	3.2000	9.4953	-4.2045	-4.0612	-3.2308	-3.0520
AlF	6.8900	12.2405	-0.4662	-0.3499	-0.6568	1.0680
SiF	5.5700	12.0156	-0.5029	-0.1059	0.3137	0.0030
SF	3.3380	11.6730	-0.9068	-0.8140	-0.0380	-0.8173
ClF	2.6160	12.2059	0.4295	-3.9612	6.8690	-4.3459
Na_2	0.7300	10.2142	-0.5498	1.0576	-2.8013	1.4272
NaCl	4.2300	11.0824	-0.4354	1.4015	-6.7895	7.3949
MgS	2.4000	11.3114	-0.5242	0.5655	-3.1955	3.8100
MgCl	2.7010	10.2253	-1.7707	-1.1903	-1.3832	-0.9560
Al_2	1.5500	11.3645	-0.1608	0.1321	-3.2955	4.3483
AlS	3.8400	11.9118	-0.4891	-0.0108	-1.2859	1.7739
AlCl	5.1200	11.8263	-0.3140	-1.0244	0.8982	-0.1197
Si_2	3.2100	12.1806	-0.6731	-0.1732	0.0349	0.4326
SiS	6.4200	12.6372	-0.7285	-0.0244	0.8566	-1.1574
SiCl	4.0020	11.7232	-0.2951	0.1824	0.8534	-0.3405

Table 1.1 (cont'd)

Species	D_0 (eV)	c_0	c_1	c_2	c_3	c_4
P_2	5.0330	12.2546	-1.1717	1.4643	-1.9459	0.8396
PS	5.6370	12.5482	1.4333	3.0823	0.9032	2.0434
S_2	4.3693	12.3238	-0.9114	2.7995	-6.1180	3.5118
ClS	2.7490	11.8411	-0.0001	0.5709	0.7753	0.0580
TiS	4.7500	11.6639	-1.3994	1.3016	-1.2659	0.5035
Cl_2	2.4760	12.2664	-0.5351	-0.6211	0.7092	-0.7675
CaS	3.4600	10.8548	0.2371	3.1884	-8.1647	5.1342
FeS	3.1000	11.3327	-1.5519	0.5150	-1.5570	-0.0107

1.3 TiO Partition Function

The electron energy level populations for molecules are normally calculated from the constituent elements' partition functions in MOOG (Sneden 1973). We modified MOOG to calculate the electron energy level populations directly from the molecular partition function for TiO, which is the only molecular line opacity source we considered. We fit a polynomial as a function of temperature to the ^{48}Ti^{16}O partition function calculated by Kurucz (1999). The resulting function was

$$\begin{aligned} log\ Q(\mathrm{TiO}) &= 5.3145 - 2.4021(log\ \theta) + 1.0378(log\ \theta)^2 - \\ & \quad 0.8135(log\ \theta)^3 + 0.4036(log\ \theta)^4. \end{aligned} \tag{1.21}$$

This equation was used to calculate the TiO partition function for a given temperature in the MOOG subroutine "Nearly." The TiO electron energy level populations were then calculated using Boltzman's equation. This feature is not included in the standard MOOG release and is unique to the code used for this Dissertation.

Bibliography

Allard, F., Hauschildt, P. H., & Schwenke, D. 2004, ApJ, 540, 1005

Allen, C., Poveda, A., & Herrera, M. A. 2000, A&A, 356, 529

Allende Prieto, C., Barklem, P. S., Lambert, D. L., & Cunha, K. 2004, A&A, 420, 183

Anders, E., & Grevesse, N. 1989, Geochim. Cosmochim. Acta, 53, 197

Asplund, M., Grevesse, N., & Sauval, A. J. 2005, in ASP Conf. Ser. 336, Cosmic Abundances as Records of Stellar Evolution and Nucleosynthesis in honor of David L. Lambert, ed. A. G. Barnes III & F. N. Bash (San Francisco: ASP), 25

Asplund, M., Gustofsson, B., Kiselman, D., & Eriksson, K. 1997, A&A, 318, 521

Baraffe, I., Chabrier, G., Allard, F., & Hauschildt, P.H. 1998, A&A, 337, 403

Barklem, P. S., Piskunov, N., & O'Mara, B. J. 2000, A&AS, 142, 467

Bean, J. L., Benedict, G. F., & Endl, M. 2006b, ApJ, 653, L65

Bean, J. L., Sneden, C., Hauschildt, P. H., Johns-Krull, C. M., & Benedict, G. F. 2006a, ApJ, 652, 1604

Bean, J. L., McArthur, B. E., Benedict, G. F., Harrison, T. E., Bizaev, D., Nelan, E., & Smith, V. V. 2007, AJ, 134, 749

Beaulieu, J.-P., & et al. 2006, Nature, 439, 437

Beichman, C. A., & et al. 2005, ApJ, 622, 1170

Benedict, G. F., McArthur, B. E., Franz, O. G., Wasserman, L. H., Henry, T. J. 2000a, AJ, 120, 1106

Benedict, G. F., & et al. 2000b, AJ, 116, 429

–. 2001, AJ, 121, 1607

–. 2002a, ApJ, 581, 115

–. 2002b, AJ, 123, 473

–. 2006, AJ, 132, 2206

–. 2007, AJ, 133, 1810

Bennett, D. P., Anderson, J., Bond, I. A., Udalski, A. U., & Gould, A. 2006, ApJ, 647, L171

Berger, D. H., & et al. 2006, ApJ, 644, 475

Bertelli, G., Bressan, A., Chiosi, C., Fagotto, F., & Nasi, E. 1994, A&AS, 106, 275

Bertone,E., Buzzoni, A., Chvez, M., & Rodrguez-Merino, L. H. 2004, AJ, 128, 829

Black, D. C., & Scargle, J. D. 1982, ApJ, 263, 854

Bond, I. A., & et al. 2004, A&A, 606, 155

Bonfils, X., Delfosse, X., Udry, S., Santos, N. C., Forveille, T., Ségransan, D. 2005a, A&A, 442, 635

Bonfils, X., & et al. 2005b, A&A, 443, 15

–. 2007, A&A, in press

Boss, A. P. 2006, ApJ, 643, 501

Bouchy, F., & et al. 2005, A&A, 444, L15

Butler, R. P., Marcy, G. W., Williams, E., McCarthy, C., Dosanjh, P., & Vogt, S. S. 1996, PASP, 108, 550

Butler, R. P., Johnson, J. A., Marcy, G. W., Wright, J. T., Vogt, S. S., & Fischer, D. A. 2006b, PASP, 118. 1685

Butler, R. P., Vogt, S. S., Marcy, G. W., Fischer, D. A., Wright, J. T., Henry, G. W., Laughlin, G., & Lissauer, J. J. 2004, ApJ, 617, 580

Butler, R. P., & et al. 2006a, ApJ, 646, 505

Cayrel de Strobel, G., Soubiran, C., & Ralite, N. 2001, A&A, 373, 159

Chabrier, G., & Baraffe, I. 1997, å, 327, 1039

Charboneau, D., Brown, T., M., Latham, D. W., & Mayor, M. 2000, ApJ, 529, L45

Chase Jr., M. W., Davies, C. A., Downey Jr., J. R., Frurip, D. J., McDonald, R. A, & Syverud, A. N. 1985, JANF Thermochemical Tables, 3rd Ed., J. Phys. Chem. Ref. Data 14, Suppl. 1

Chen, Y. Q., & Zhao, G. 2006, AJ, 131, 1816

Cox, A. N. ed. 2000, Allen's Astrophysical Quantities (4th ed.; New York: AIP)

Creevey, O. L., & et al. 2005, ApJ, 625, L127

Cutri, R. M., & et al. 2003 The 2MASS All-Sky Catalog of Point Sources (Pasadena: IPAC/California Inst. Technology)

Dawson, P. C., & De Robertis, M. M. 2004, 127, 2909

Delfosse, X., Forveille, T., Mayor, M., Perrier, C., Naef, D., & Queloz, D. 1998, A&A, 338, 67

Delfosse, X., Forveille, T., Ségransan, D., Beuzit, J. -L., Udry, S., Perrier, C., & Mayor, M. 2000, A&A, 364, 217

Desidera, S., & et al. 2004, A&A, 420, 683

Dubois, L. H., & Gole, J. L. 1977, J. Chem. Phys. 66, 779

Ecuvillon, A., Israelian, G., Santos, N. C., Shchukina, N. G., Mayor, M., & Rebolo 2006, å, 445, 633

Endl, M., Cochran, W. D., Kürster, M., Paulson, D. B., Wittenmyer, R. A., MacQueen, P. J., & Tull, R. G. 2006, ApJ, 649, 436

ESA 1997, The Hipparcos and Tycho Catalogues, ESA SP-1200

Fischer, D. A., & Valenti, J. A. 2005, ApJ, 622, 1102

Forveille, T., & et al. 1999, å, 351, 619

Fuhrmann, K., Pfeiffer, M. J., & Bernkopf, J. 1997, A&A, 326, 1081

–. 1998, A&A, 336, 942

Gilliland, R. L., Morris, S. L., Weymann, R. J., & Ebbets, D. C. 1992, PASP, 104, 367

Gillon, M., & et al. 2007, A&A, in press

Gonzalez, G. 1997, MNRAS, 285, 403

–. 1998, A&A, 334, 221

–. 1999, MNRAS, 308, 447

–. 2006, PASP, 118, 1494

Gonzalez, G., Laws, C., Tyagi, S., & Reddy, B. E. 2001, AJ, 121, 432

Gould, A., & et al. 2006, ApJ, 644, 37

Gustafsson, B., Bell, R. A., Eriksson, K., & Nordlund, Å. 1975, A&A, 42, 407

Hauschildt, P. H., Allard, F., & Baron, E. 1999, ApJ, 512, 377

Henry, G. W., Marcy, G. W., Butler, R. P., & Vogt, S. S. 2000, ApJ, 529, L41

Henry, T. J. 1998, in ASP Conf. Ser. 134, Brown Dwarfs and Extrasolar Planets, ed. R. Rebolo, E. L. Martín, & M. R. Zapatero Osorio (San Francisco: ASP), 28

Henry, T. J., & McCarthy, D. W., Jr. 1993, AJ, 106, 773

Henry, T. J., & et al. 1999, ApJ, 512, 864

Hillenbrand, L. A., & White, R. J. 2004, ApJ, 604, 741

Holmberg, J., Flynn, C., & Portinari, L. 2006, MNRAS, 367, 449

Huber, K. P., & Herzberg, G. 1979, Molecular Spectra and Molecular Structure, Vol. 4, Constants of Diatomic Molecules (New York: Van Nostrand Rheinhold)

Ida, S., & Lin, D. N. C. 2005, ApJ, 626, 1045

Jefferys, W. H. 1990, Biometrika, 77, 597

Jefferys, W. H., Fitzpatrick, M. J., & McArthur, B. 1988, Celestial Mechanics 41, 39

Jørgensen, U. G. 1994, A&A, 284, 179

Käufl, H. U., & et al. 2004, Proc. SPIE, 5492, 1218

Kroupa, P., & Tout, C. A. 1997, MNRAS, 287, 402

Kupka, F., Pisknunov, N. E., Ryabchikova, T. A., Stempels, H. C., & Weiss, W. W. 1999, A&AS, 138, 119

Kurucz, R. L. 1993, ATLAS9 Stellar Atmosphere Programs and 2 km/sec grid, Kurucz CD-ROM No. 13

–. 1999, TiO linelist from Schwenke, Kurucz CD-ROM No. 24

Kurucz, R. L., Furenlid, I., Brault, J., & Testerman, L. 1984, National Solar Observatory Atlas (Sunspot, New Mexico: NSO)

Kučinskas, A., Hauschildt, P. H., Ludwig, H.-G., Brott, I., Vansevičius, V, Lindegren, L, Tanabé, T, & Allard, F. 2005, A&A, 442, 281.

Lane, B. F., Boden, A. F., & Kulkarni, S. R. 2001, ApJ, 551, L81

Laughlin, G., Bodenheimer, P., & Adams, F. C. 1997, ApJ, 482, 420

–. 2004, ApJ, 612, 73

Laws, C., Gonzalez, G., Walker, K. M., Tyagi, S., Dodsworth, J., Snider, K., & Suntzeff, N. B. 2003, AJ, 125, 2664

Leggett, S. K., Allard, F., Berriman, G., Dahn, C. C., & Hauschildt, P. H. 1996, ApJS, 104, 117

López-Morales, M., & Ribas, I. 2005, ApJ, 631, 1120

Maceroni, C., & Montalbán, J. 2004, A&A, 426, 577

Marcy, G. W., Butler, R. P., Fischer, D. A., Vogt, S. S., Lissauer, J. J., & Rivera, E. J. 2001, ApJ, 556, 296

Marcy, G. W., Butler, R. P., Fischer, D. A., Vogt, S. S., Wright, J. T., Tinney, C. G., & Jones, H. R. A. 2005 PThPS, 158, 24

Marcy, G. W., Butler, R. P., Vogt, S. S., Fischer, D. A., & Lissauer, J. J. 1998, ApJ, 505, 147

Marquardt, D. W. 1963, J. Soc. Ind. Appl. Math. 11, 431

Martin, C., Mignard, F., Hartkopf, W. I., McAllister, H. A. 1998, A&AS, 133, 149

Martinache, F., Lloyd, J. P., Ireland, M. J., Yamada, R. S., Tuthill, P. G. 2007, ApJ, 661, 496

Mason, B. D., & Hartkopf, W. I. 2006, JDSO, 2, 171

Mazeh, T., & et al. 2001, MNRAS, 325, 343

Maxted, P. F. L., & et al. 2004, MNRAS, 355, 1143

McArthur, B. E., Benedict, G. F. , Jeffreys, W. H., & Nelan, E. 2002, in The 2002 *HST* Calibration Workshop, Ed. S. Arribas, A. Koekemoer, & B. Whitmore (Baltimore: STScI)

McArthur, B. E., & et al. 2004, ApJ, 614, L81

Metcalfe, T. S., Mathieu, R. D., Latham, D. W., & Torres, G. 1996, ApJ, 456, 356

Mayor, M, & Queloz 1995, Nature, 378, 355

Nauenberg, M. 2002, ApJ, 568, 369

Naulin, C., Hedgecock, I. M.,& Costes, M. 1997, Chem. Phys. L., 266, 335

Nelan, E., & et al. 2003, Fine Guidane Sensor Handbook, Ver. 12.0 (Baltimore: STSCcI)

Perrier, C., Sivan, J.-P., Naef, D., Beuzit, J.-L., Mayor, M., Queloz, D., Udry, S. 2003, å, 410, 1039

Perryman, M. A. C. 2005, in ASP Conf. Ser. 338, Astrometry in the Age of the Next Generation of Large Telescopes, ed. Seidelmann, P. K., & Monet, A. K. B.(San Francisco: ASP), 3

Perryman, M. A. C. & et al. 1997, A&A, 323, 49

Pickles, A. J. 1998, PASP, 110, 863

Piskunov, N. E. 1992 in Stellar Magnetism, Proceedings of international meeting on the problem "Physics and evolution of stars", ed. Yu.V. Glagolevskij & I.I. Romanyuk (Saint Petersburg: NAUKA), 92

Piskunov, N. E., Kupka, F., Ryabchikova, T. A., Weiss, W. W., & Jeffery, C. S. 1995, A&AS, 112, 525

Piskunov, N. E., & Valenti, J. A. 2002, A&A, 385, 1095

Plez, B. 1998, A&A, 337, 495

Pollack, J. B., Hubickyi, O., Bodenheimer, P., Lissauer, J. J., Podolack, M., & Greenzweig, Y. 1996, Icarus, 124, 62

Pourbaix, D., & Jorissen, A. 2000, A&AS, 145, 161

Poveda, A., Herrera, M. A., Allen, C., Cordero, G., Lavalley, C. 1994, RMxAA, 28, 43

Press, W. H., Flannery, B. P., Teukolsky, S. A., & Vetterling W. T. 1986, Numerical Recipes (Cambridge: Cambridge University Press)

Press, W. H., Teukolsky, S. A., Vetterling, W. T., & Flannery, B. P. 1992, Numerical Recipes: The Art of Scientific Computing (2nd Edition; Cambridge: Cambridge University Press)

Ramirez, I., Allende Prieto, C., & Lambert, D. L. 2007, in preparation

Ramirez, I., & Meléndez, J. 2004, ApJ, 609, 417

–. 2005, ApJ, 626, 465

Reddy, B. E., Tomkin, J., Lambert, D. L., & Allende Prieto, C. 2003, MNRAS, 340, 304

Reffert, S., & Quirrenbach, A. 2006, A&A, 449, 699

Reid, I. N., & Hawley, S. L. 2005, New Light on Dark Stars: Red Dwarfs, Low-Mass Stars, Brown Dwarfs (2nd ed.; London: Springer)

Ribas, I. 2003, A&A, 398, 239

Rivera, E. J., & et al 2005, ApJ, 634, 625

Santos, N. C., Israelian, G., & Mayor, M. 2000, A&A, 363, 228

–. 2004, A&A, 415, 1153

Santos, N. C., Israelian, G., Mayor, M., Bento, J. P., Almeida, P. C., Sousa, S. G., & Ecuvillon, A 2005, A&A, 437, 1127

Santos, N. C., Israelian, G., Mayor, M., Rebolo, R., & Udry, S. 2003, A&A, 398, 363

Sato, B., & et al. 2005, ApJ, 633, 465

Sauval, A. J., & Tatum, J. B. 1984, ApJS, 56, 193

Schweitzer, A., Hauschildt, P., Allard, F., & Basri, G. 1996, MNRAS, 283, 821

Ségransan, D. 2001, Ph.D. Thesis, Laboratoire d'Astrophysique de Grenoble

Ségransan, D., Delfosse, X., Forveille, T., Beuzit, J.-L., Udry, S., Perrier, C., Mayor, M. 2000, A&A, 364, 665

Ségransan, D., Kervella, P., Forveille, T., & Queloz, D. 2003, A&A, 397, L5

Sekiguchi, M., & Fukugita, M. 2000, AJ, 120, 1072

Siess, L., Dufour, E., & Forestini, M. 2000, A&A, 358, 593

Sneden, C. 1973, Ph.D. Thesis, University of Texas

Takeda, G., Ford, E. B., Sills, A., Rasio, F. A., Fischer, D. A., & Valenti, J. A. 2007, ApJS, 168, 297

Torres, G., Boden, A. F., Latham, D. W., Pan, M., Stefanif, R. P. 2002, AJ, 124, 1716

Torres, G., Henry, T. J., Franz, O. G., & Wasserman, L. H. 1999, AJ, 117, 562

Torres, G., & Ribas, I. 2002, ApJ, 567, 1140

Tull, R. G. 1998, Proc. SPIE, 3355, 387

Tull, R. G., MacQueen, P. J., Sneden, C., & Lambert, D. L. 1995, PASP, 107, 251

Unsöld, A. 1955, Physik der Sternatmosphären. Springer-Verlag, Berlin

Udry, S., & et al. 2007, A&A, 469, L43

Valenti, J. A., Butler, R. P., & Marcy, G. W. 1995, PASP, 107, 966

Valenti, J. A., & Fischer, D. A. 2005, ApJS, 159, 141

Valenti, J., Piskunov, N., & Johns-Krull, C. M. 1998, ApJ, 498, 851, V98

Vogt, S. S., Butler, R. P., Marcy, G. W., Fischer, D. A., Pourbaix, D., Apps, K., & Laughlin, G. 2002, ApJ, 568, 352

Wittenmyer, R. A., Endl, M., Cochran, W. D., Hatzes, A. P., Walker, G. A. H., Yang, S. L. S., & Paulson, D. B. 2006, AJ, 132, 177

Wright, J. T. 2005, PASP, 117, 657

Woolf, V. M., & Wallerstein, G. 2006, PASP, 118, 218

Zacharias, N., & et al. 2004, AJ, 127, 3043

Vita

Jacob L. Bean was born 24 June 1980, the son of David and Gayle Bean. He attended Murray County public schools in Georgia for elementary, middle, and high school education. He also matriculated at Dalton College during his final year of high school for concurrent enrollment in Mathematics and Literature courses. After graduating from high school in 1998, he attended the Georgia Institute of Technology for undergraduate studies. He received a Bachelor of Science degree in Physics with highest honors in May of 2002. He began graduate school at the University of Texas in August of 2002. During graduate school he worked with his Advisors G. Fritz Benedict and Chris Sneden on the topics covered in this dissertation.

Permanent address: 626 Green Rd.
Chatsworth, GA 30705

This dissertation was typeset with LaTeX[†] by the author.

[†]LaTeX is a document preparation system developed by Leslie Lamport as a special version of Donald Knuth's TeX Program.